Making light jump

Photonic crystals on trampoline membranes for optomechanics experiments

Pinto Moura, Joâo

DOI
10.4233/uuid:f090d58f-558c-47ed-8c9c-3152dadbc4ae

Publication date
2019

Document Version
Final published version

Citation (APA)
Pinto Moura, J. (2019). *Making light jump: Photonic crystals on trampoline membranes for optomechanics experiments*. [Dissertation (TU Delft), Delft University of Technology]. https://doi.org/10.4233/uuid:f090d58f-558c-47ed-8c9c-3152dadbc4ae

MAKING LIGHT JUMP

PHOTONIC CRYSTALS ON TRAMPOLINE MEMBRANES FOR OPTOMECHANICS EXPERIMENTS

MAKING LIGHT JUMP

PHOTONIC CRYSTALS ON TRAMPOLINE MEMBRANES FOR OPTOMECHANICS EXPERIMENTS

Dissertation

for the purpose of obtaining the degree of doctor
at Delft University of Technology
by the authority of the Rector Magnificus prof. dr. ir. T.H.J.J. van der Hagen
chair of the Board for Doctorates
to be defended publicly on
Wednesday 3 April 2019 at 15:00 o'clock

by

João Pedro PINTO MOURA

Master of Science in Physical Engineering, University of Porto, Portugal
born in Porto, Portugal

This dissertation has been approved by the promotors.

Composition of the doctoral committee:

Rector Magnificus,	chairperson
Prof. dr. ir. H.S.J. van der Zant,	Delft University of Technology, promotor
Dr. S. Gröblacher,	Delft University of Technology, copromotor
Independent members:	
Prof. dr. L. Kuipers,	Delft University of Technology
Prof. dr. D. Vitali,	University of Camerino, Italy
Prof. dr. G.A. Steele,	Delft University of Technology
Prof. dr. S. Schmid,	Vienna University of Technology, Austria
Dr. W. Löffler,	Leiden University
Prof. dr. Y.M. Blanter,	Delft University of Technology, reserve member

Keywords: Optical cavities, mechanical resonators, silicon nitride, optomechanics, photonic crystal slabs, optomechanical arrays

Printed by: Gildeprint, Enschede

Cover: Schematic of a photonic crystal on a trampoline membrane.

ISBN 978-90-8593-390-8
Casimir PhD series 2019-06

An electronic version of this dissertation is available at
http://repository.tudelft.nl/.

To my family,
both given
and chosen.

CONTENTS

SUMMARY

CAVITY optomechanics studies the interaction between mechanical resonators and optical cavities through radiation pressure forces and aims to harness this interaction for applications in the areas of high precision metrology, tests of fundamental quantum mechanics, or quantum information processing. For the most ambitious of these applications it is necessary that the mechanical resonator has a sufficiently high mechanical quality factor such that it can undergo at least a few coherent oscillations before interacting with incoherent thermal phonons. Furthermore, the optomechanical coupling must be large enough to make the interaction between optics and mechanics probable and, ideally, deterministic.

This work pursues both goals using a thin membrane in the middle (MIM) of an optical cavity. This is a common configuration in cavity optomechanics but most experiments to date have low mechanical quality factors and optomechanical couplings.

Chapters 2 and 3 contain a brief overview of the basic theory and experimental concepts required to understand the following.

On chapter 4 we investigate the mechanical properties of SiN trampoline resonators: square membranes supported by four tethers connected to the substrate. We study the effect of all their geometrical parameters on the frequency–quality factor product and find that the most relevant ones are the thicknesses of both the membrane and the substrate. By fabricating trampoline membranes with a Si thickness of 1 mm and a 20 nm-thick SiN layer, we obtain fundamental frequencies close to 150 kHz and quality factors up to 10^8, resulting in a frequency–quality factor product of 1.37×10^{13} Hz. This is the first demonstration of a mechanical resonator with good enough properties to, for example, reach the mechanical ground state of a macroscopic object using optomechanical cooling starting from room temperature conditions.

Bare SiN membranes have low reflectivity due to their low refractive index and since they are typically much smaller than a quarter of a wavelength (the thickness for which the reflectivity of a thin film reaches its maximum). Since the optomechanical coupling in a MIM configuration scales with the square root of the membrane's reflectivity, bare membranes have low optomechanical couplings. To counter this, we pattern photonic crystals (PhC), composed of a periodic array of holes etched into the membranes, obtaining reflectivities higher than 99.3 %. For PhCs with a small area, the maximum reflectivity achievable drops with the film thickness. This work presents two solutions for this problem. On chapter 4 we leave thick pillars of SiN on the 20 nm-thin membranes, obtaining similar performance to thicker devices. On the other hand, on chapter 5 we increase the PhC area from $90 \times 90\ \mu m^2$ up to $10 \times 10\ mm^2$. This allows using laser beams with a larger waist and smaller wavevector spread, increasing the maximum achievable reflectivity of thin membranes.

Due to its square root dependency on the reflectivity, the gain in optomechanical

coupling by patterning a PhC on the trampoline membranes is limited to little more than 50 % of what can be achieved with a bare membrane. However, the high reflectivity of PhC membranes can be harnessed to increase the optomechanical coupling by orders of magnitude in comparison with that of a bare membrane. If more than one highly reflective membrane is placed in the middle of a cavity, the relative motion between the mechanical elements is expected to generate strong phase shifts which can result in strong optomechanical coupling rates. On chapter 6 we present one of the first experimental explorations of such optomechanical arrays. We fabricate two PhC trampoline membranes on both sides of the same chip, which constitute two high reflectivity mechanical resonators parallel to each other. We characterize them independently, measuring finesse values up to 220, as well as inside an optical cavity, confirming that their center-of-mass motion couples to the cavity in a fashion well described by the single-MIM model. This type of device is a large step towards the observation of enhanced coupling with optomechanical arrays.

The results presented here are not only significant for the field optomechanics but they also present promising applications elsewhere. Mechanical resonators with very high mechanical quality factor, such as those of chapter 4, can be used for displacement or force detectors with very high sensitivity. Large-area PhC membranes (chapter 5) open the door to mechanically tunable mirrors whose optical properties can be freely adapted to the wavelength or polarization response that the user wishes. And finally, devices such as the double-PhC-membranes of chapter 6 could be used as integrated cavities for filtering or simple optomechanics experiments.

SAMENVATTING

CAVITY optomechanica bestudeert de interactie tussen mechanische resonatoren en optische trilholtes (cavities) middels de stralingsdruk en beoogt deze interactie te gebruiken voor toepassingen zoals hoge precisie metrologie, het testen van fundamentele quantum mechanica of quantum informatieverwerking. Bij de meest ambitieuze van deze toepassingen is het noodzakelijk dat de mechanische resonator een voldoende hoge mechanische kwaliteitsfactor heeft zodat de resonator tenminste een paar coherente oscillaties heeft ondergaan vóór de interactie met incoherente thermische phononen. Daarnaast moet de optomechanische koppeling sterk genoeg zijn om de interactie tussen optiek en mechaniek waarschijnlijk en idealiter ook deterministisch te maken.

Beide doelen worden in dit werk nagestreefd met behulp van een dun membraan in het midden van een optische trilholte (MIM). Dit is een welbekende configuratie in cavity optomechanica maar in de meeste experimenten tot nu toe zijn de mechanische kwaliteitsfactoren en optomechanische koppelingen laag.

Hoofdstukken 2 en 3 geven een kort overzicht van de theorie en experimentele concepten die benodigd zijn om het volgende te begrijpen.

In hoofdstuk 4 onderzoeken we de mechanische eigenschappen van SiN trampoline resonatoren: vierkante membranen die via vier verbindingen vast zitten aan het substraat. We bestuderen het effect van al hun geometrische parameters op het frequentie–kwaliteitsfactor product en ontdekken dat daarin de diktes van het membraan en het substraat het meest relevant zijn. Door trampoline membranen te fabriceren met een Si dikte van 1 mm en een 20 nm dikke SiN laag verkrijgen we fundamentele resonantie frequenties nabij 150 kHz en kwaliteitsfactoren tot aan 10^8, wat resulteert in een frequentie–kwaliteitsfactor product van 1.37×10^{13} Hz. Dit is de eerste demonstratie van een mechanische resonator met eigenschappen die voldoende zijn om bijvoorbeeld de mechanische grondtoestand van een macroscopisch object te bereiken door vanaf kamer temperatuur optomechanisch te koelen.

Membranen van onbewerkt SiN hebben een lage reflectiviteit door hun lage brekingsindex en doordat ze typisch veel kleiner zijn dan een kwart van de golflengte (de dikte waarbij de reflectiviteit van een dunne film maximaal is). Aangezien de optomechanische koppeling in een MIM configuratie schaalt met de wortel van de reflectiviteit van het membraan, is de optomechanische koppeling van onbewerkte membranen laag. Om dit te bestrijden etsen we een periodiek patroon van gaatjes, een zogenaamd photonisch kristal (PhC), in de membranen, waardoor we reflectiviteiten boven de 99.3 % verkrijgen. Bij PhC's met een klein oppervlak zakt de maximaal bereikbare reflectiviteit met de filmdikte. In dit werk worden twee oplossingen voor dit probleem gepresenteerd. In hoofdstuk 4 laten we dikke pilaren van SiN op de 20 nm dunne membranen staan, waarbij we gedrag vergelijkbaar met dikkere apparaten verkrijgen. Aan de andere kant vergroten we het PhC oppervlak van $90 \times 90\,\mu m^2$ naar $10 \times 10\,mm^2$ in hoofdstuk 5.

Hierdoor kan men laser licht gebruiken met een grotere waist en een kleinere golfvector spreiding, waardoor de maximaal haalbare reflectiviteit van dunne membranen wordt verhoogd.

Door zijn wortel afhankelijkheid van de reflectiviteit is de versterking van de optomechanische koppeling, door het etsen van een PhC in een trampoline membraan, gelimiteerd aan ongeveer 50 % van wat gehaald kan worden met een onaangepast membraan. Echter, de hoge reflectiviteit van PhC membranen kan gebruikt worden om de optomechanische koppeling met een aantal orde groottes te vergroten ten opzichte van onaangepaste membranen. Als er meer dan één zeer reflectief membraan in het midden van een trilholte wordt geplaatst, wordt er verwacht dat de relatieve beweging tussen de mechanische elementen sterke fase verschuivingen genereert wat tot sterke optomechanische koppeling kan leiden. In hoofdstuk 6 presenteren we een van de eerste experimentele verkenningen van zulke optomechanische reeksen. We fabriceren twee PhC trampoline membranen aan beide zijdes van dezelfde chip, die zo twee zeer reflectieve parallele mechanische resonatoren vormen. Deze worden onafhankelijk gekarakteriseerd, waarbij finesse waardes tot 220 worden gemeten, en in een optische trilholte, waarbij wordt bevestigd dat de massamiddelpunts beweging aan de trilholte koppelt op een manier die goed beschreven kan worden door het enkel-MIM model. Dit type apparaat is een grote stap richting het observeren van versterkte koppeling met optomechanische reeksen.

De hier gepresenteerde resultaten zijn niet alleen significant met betrekking tot optomechanica maar kunnen elders ook tot veelbelovende toepassingen leiden. Mechanische resonatoren met zeer hoge mechanische kwaliteitsfactor, zoals die beschreven in hoofdstuk 4, kunnen gebruikt worden in verplaatsings- of krachtmeters met zeer hoge gevoeligheid. PhC membranen met groot oppervlak (hoofdstuk 5) openen de deur naar mechanisch afstembare spiegels waarvan de optische eigenschappen aangepast kunnen worden aan de gewenste golflengte of polarisatie respons. Tenslotte zouden apparaten zoals de dubbele PhC membranen uit hoofdstuk 6 gebruikt kunnen worden als geïntegreerde trilholtes voor optisch filteren of simpele optomechanische experimenten.

1

INTRODUCTION

CONTEXT

LENGTH is a fundamental dimension which plays a crucial role in society. It is therefore natural that scientists and engineers have placed extensive efforts in developing tools to measure it as accurately as possible.

Perhaps some of the most impressive length measurement tools developed recently are gravitational wave detectors [1–4]. The goal of these devices is to measure minute displacements caused by gravitational waves. An example of the extreme sensitivity of these devices is the recent measurement of the collision of two black holes of approximately 30 $M_\odot$ each which occurred 410 Mpc away from the Earth. The gravitational wave generated by this collision created a peak displacement on Earth of 4 am at approximately 100 Hz. This event was notably measured by the LIGO and Virgo collaborations in 2016 [5], which was awarded the Nobel Prize in Physics one year after [6].

The principle of operation of these remarkable experiments is surprisingly simple: it relies on measuring variations in the distance between two mirrors using light. The mirrors constitute an optical cavity. If the distance between them changes, so will the cavity's resonance frequency and, consequently, the phase of light that couples out of the cavity. By accurately measuring light's phase, one can retrieve the variations in cavity length caused by passing gravitational waves or other sources of displacement.

However simple, it was soon understood that achieving the required sensitivities would prove to be an incredibly complex scientific and engineering challenge. Crucially, it was necessary to identify and minimize all possible sources of cavity displacement oscillations not related to gravitational waves, which in this context act as sources of noise. Some effects are quite obvious. For example, the cavity mirrors need to be decoupled as much as possible from their environment, so that mechanical vibrations around the experiment do not make the mirrors move [7, 8]. Others are much subtler.

Of particular interest, when a photon reflects off one of the mirrors, it will transfer some momentum to the mirror and thus displace it. Although the momentum of a single photon is small, this effect can still be relevant, since one typically works with a

large number of photons and each photon bounces back and forth inside the cavity a large number of times. If the rate of photon momentum "kicks" (i.e. the radiation pressure) was stable, it would simply cause a fixed change of the cavity length. But due to the random nature of light [9], the radiation pressure fluctuates and acts as a source of displacement noise.

CAVITY OPTOMECHANICS

In the context of displacement measurements, the radiation pressure is typically seen as a source of noise which should be avoided in order to increase the measurements' sensitivity. Interestingly, one can look at it not only as a source of noise, but also as a tool to control the mirror's motion. For example, if the radiation pressure is modulated in phase with the motion, then the mirror can be accelerated; vice versa, if the force is out of phase, it is possible to decelerate it. This type of *feedback amplification and cooling* can be applied directly to a moving particle [10] but, together with an optical cavity, this effect can be harnessed to control objects with a high mass [11]. For example, using feedback cooling it is possible to dampen the motion of particular mechanical resonances of the gravitational wave interferometers and thus decrease their thermal displacement noise [12].

Cavity optomechanics is the field that more generally studies the interaction between an optical cavity and a mechanical oscillator [13]. These effects are observed in a multitude of systems with different optical and mechanical properties. The mechanical resonators span from massive, kilogram-scale mirrors oscillating at 100 Hz [12]; to thin, suspended nanogram membranes with frequencies around 1 MHz [14]; or even picogram nanobeams with GHz vibrational modes [15].

The most conventional cavity optomechanical picture is the case where the mechanical resonator is a mirror at the end of a Fabry-Perot cavity, such as in gravitational wave interferometers. Another typical situation is that in which the optical and mechanical oscillators are highly integrated in the same volume, such as in nanobeams, where a photonic crystal confines the mechanical and optical modes in the same region [15]. An issue with these configurations is that when either the cavity or the mechanical oscillator needs to be modified, they will in general also affect the other one. An alternative is to place a *membrane in the middle* of an optical cavity [14]. In this way, the cavity and the mechanical oscillator are completely independent, avoiding common trade-offs between their properties.

Over the past years, the goals of cavity optomechanics expanded further than high sensitivity displacement detection. Indeed, today's most interesting paths of research lie on the regime where both oscillators behave as quantum harmonic oscillators. In this case, the optomechanical coupling allows the preparation of quantum states of motion (optical and/or mechanical) [16]; studying quantum decoherence mechanisms in massive objects [17]; or transducing between different frequencies coherently through the mechanical oscillator [18].

CHALLENGES

A few requirements must be met to realize some of these *quantum optomechanics* experiments. Most prominently:

- The mechanical resonator must be able to undergo at least a few coherent oscillations before interacting with incoherent thermal phonons;
- The coupling between optics and mechanics must be large enough to make their interaction probable and, ideally, deterministic.

The rate of thermal phonons that couple to the mechanical resonator is given by the product of the thermal phonon occupancy n_{th}, which depends on the working frequency and environment temperature, and the coupling between the resonator and its thermal environment, also called the mechanical decay rate, Γ_{m}, which is an intrinsic property of the resonator [13]. The most straightforward way to increase the number of coherent oscillations that a mechanical resonator can perform before it is decohered by environmental phonons is to decrease n_{th} by cooling the bath temperature. This decreases the thermal occupation of phonons at the frequency of the mechanical oscillator, therefore decreasing the rate of thermal phonon coupling. This method is particularly interesting for GHz resonators, since, at temperatures commonly reached by dilution refrigerators, the thermal phonon occupancy is so low that the resonator can be considered to be in its ground state of motion [19]. Unfortunately, in systems with lower frequencies, such as the ones studied in this thesis, it is not technically feasible to decrease the temperature sufficiently. Instead, one must engineer the resonator itself to decrease Γ_{m}.

The *optomechanical coupling* g_0 is a measure of how strongly the optical and mechanical resonators interact [13]. It is defined by how much the cavity frequency changes for a given displacement of the mechanical oscillator. To facilitate comparison between different systems, one often looks at the ratio between g_0 and the cavity decay rate. If this ratio is larger than 1, an optomechanical system is said to be in the *single photon/phonon strong coupling* regime. This means that a single phonon shifts the cavity frequency by more than the decay rate. Having such a strong coupling between the optical and mechanical oscillators is a long-standing goal in the field. The most common approach to increase g_0 is to optimize the overlap between the optical and mechanical mode volumes, but the best results to date are still orders of magnitude below the strong coupling regime [20]. Many groups are therefore exploring alternative paths that can bring us closer to it.

THESIS GOALS AND OUTLINE

One of the most promising approaches towards the strong coupling regime explores the collective motion of multiple membranes inside an optical cavity [21]. This type of *optomechanical array* is a variation of the membrane-in-the-middle system. The concept relies on using two or more highly reflective membranes with a spacing between them such that they are optically resonant with the outer cavity. Small variations of the relative position between the individual membranes will change the phase of the outer cavity's field more strongly than what would happen with a single membrane. It is predicted that if the reflectivity of the membranes is high enough and if they are placed much closer to

each other than the length of the outer cavity, it could be possible to strongly couple the optical and mechanical oscillators.

This thesis paves the way towards the observation of enhanced coupling with optomechanical arrays of tethered silicon nitride membranes. Chapter 2 briefly introduces fundamental theory concepts of mechanical resonators, optical cavities, cavity optomechanics and optomechanical arrays. Chapter 3 explains how the devices are fabricated and the tools we use to study them. The following three chapters describe experiments realized during the course of the past four years. Chapter 4 explores the mechanical properties of individual tethered membranes and shows that their geometries can be optimized such that the mechanical decay rate decreases to values that could allow performing quantum optomechanical experiments at room temperature. These membranes are made reflective by patterning photonic crystals on them. Chapter 5 shows it is possible to make high-reflectivity photonic crystals on thin silicon nitride membranes with large areas, which is necessary for optomechanical arrays with low mechanical dissipation and high optomechanical coupling. Finally, chapter 6 presents the first platform that combines two tethered silicon nitride membranes with a high reflectivity and a study of their optomechanical center-of-mass coupling.

2

THEORY

THIS chapter introduces some theoretical concepts required to understand the experiments performed in the remainder of the thesis. This is a brief introduction and the reader is recommended to consult the cited references for more details and in-depth discussions.

2.1. MECHANICAL OSCILLATORS

The displacement of a mechanical oscillator can be described by a vector $\vec{u}(\vec{r},t)$ [13]. $\vec{r}$ represents a position on the device and t a particular time at which the displacement is described. Typically we are interested in studying the normal modes of the oscillator, described by the product of a time-independent amplitude $\vec{u}_n(\vec{r})$ and a scalar function $x_n(t)$ that contains the time evolution of each mode. n is a label of each specific mode. The dynamics of these modes are described by the linear equation of motion

$$m\ddot{x}(t) + m\Gamma_{\mathrm{m}}\dot{x}(t) + m\omega_{\mathrm{m}}^2 x(t) = F(t), \tag{2.1}$$

where m is the mass of the mechanical mode, $F(t)$ represents the total force applied to the resonator and where we have dropped the subscript n, since from now on we will always focus on a single resonance. Γ_{m} and ω_{m} are the decay rate and frequency of the mechanical mode. The decay rate will be discussed in more detail on chapter 4. The frequency can usually be either calculated, if the geometry of the mechanical oscillator is simple enough, or simulated.

By Fourier transforming equation 2.1 we can rewrite it in the form $x(\omega) = \chi_{\mathrm{m}}(\omega)F(\omega)$, where ω is the frequency and $\chi_{\mathrm{m}}(\omega)$ is the mechanical susceptibility which describes the resonator's displacement in response to applied forces:

$$\chi_{\mathrm{m}}(\omega) = \frac{1}{m}\frac{1}{\omega_{\mathrm{m}}^2 - \omega^2 - i\Gamma_{\mathrm{m}}\omega}. \tag{2.2}$$

As such, by measuring $x(t)$ with respect to a known force $F(t)$ and performing a Fourier

transform of both, one obtains the mass, frequency and decay rate of the particular resonator normal mode which is being studied.

Often, $x(t)$ is acquired by a spectrum analyzer. This tool measures the variance $\mathrm{Var}[x(t)]$, which is equal to $\langle x^2(t)\rangle$ if the mean is zero, and performs its Fourier transform, outputting $\langle x^2(\omega)\rangle$ [22, 23]. Using the Wiener-Kinchin theorem we learn that

$$\langle x^2(\omega)\rangle = S_{xx}(\omega),$$

where $S_{xx}(\omega)$ is the power spectral density of $x(t)$ [13].

Assuming once again that our system is linear, we can write

$$S_{xx}(\omega) = \left|\chi_{\mathrm{m}}(\omega)\right|^2 S_{FF}(\omega),$$

where $S_{FF}(\omega)$ is the power spectral density of the force applied to the resonator. If the device is in thermal equilibrium with an environment of temperature T,

$$S_{FF}(\omega) = 2\frac{k_{\mathrm{B}}T}{\omega}\,\mathrm{Im}\left[\chi_{\mathrm{m}}^{-1}(\omega)\right] = 2mk_{\mathrm{B}}T\Gamma_{\mathrm{m}}$$

where k_{B} is Boltzmann's constant. This leads to a thermally driven displacement power spectral density which follows a Cauchy (Lorentzian) distribution [22, 24]

$$S_{xx}(\omega) \approx \frac{2k_{\mathrm{B}}T}{m\omega_{\mathrm{m}}\Gamma_{\mathrm{m}}}\frac{1}{1+4(\omega_{\mathrm{m}}-\omega)^2/\Gamma_{\mathrm{m}}^2}. \tag{2.3}$$

The previous equations give us the tools to interpret the spectra of mechanical resonators measured with a spectrum analyzer. They were derived from a classical interpretation of the resonator's motion. However, this can also be analyzed from the perspective of a quantum harmonic oscillator. One of the key results of this picture is that even if the oscillator has a *phonon* occupancy $\bar{n} = 0$, its position still has a non-zero variance x_{zpf}^2, where

$$x_{\mathrm{zpf}} = \sqrt{\frac{\hbar}{2m\omega_{\mathrm{m}}}} \tag{2.4}$$

is the *zero-point fluctuation* of displacement and $\hbar$ is the reduced Planck constant.

If the resonator is in thermal equilibrium with its environment, it will have a *thermal phonon occupancy* $n_{\mathrm{th}} \approx k_{\mathrm{B}}T/\hbar\omega_{\mathrm{m}}$ [13]. The rate of thermal phonon coupling between the resonator and the environment is given by

$$n_{\mathrm{th}}\Gamma_{\mathrm{m}} = k_{\mathrm{B}}T/\hbar Q_{\mathrm{m}},$$

where $Q_{\mathrm{m}} = \omega_{\mathrm{m}}/\Gamma_{\mathrm{m}}$ is the mechanical quality factor. This interaction acts as a decoherence mechanism of the resonator. As mentioned on the introduction, in order to perform quantum optomechanics experiments it is necessary that the resonator can oscillate coherently at least a few times, i.e.

$$\frac{\omega_{\mathrm{m}}}{n_{\mathrm{th}}\Gamma_{\mathrm{m}}} > 1 \Leftrightarrow \omega_{\mathrm{m}} > \frac{k_{\mathrm{B}}T}{\hbar Q_{\mathrm{m}}} \Leftrightarrow Q_{\mathrm{m}}\omega_{\mathrm{m}} > \frac{k_{\mathrm{B}}T}{\hbar}.$$

In this context, it is typical to compare mechanical resonators based on $Q_{\mathrm{m}}f_{\mathrm{m}}$, where $\omega_{\mathrm{m}} = 2\pi f_{\mathrm{m}}$ and the previous inequality can be written as $Q_{\mathrm{m}}f_{\mathrm{m}} > k_{\mathrm{B}}T/h \approx 6.25\times10^{12}$ Hz.

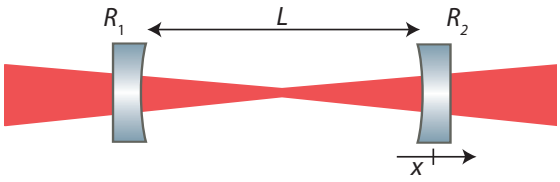

Figure 2.1: Schematic representation of a Fabry-Perot optical cavity, composed of two mirrors with reflectivities R_1 and R_2. The mirrors have a distance L between each other. The left mirror is fixed, whereas the second can suffer displacements of amplitude x around its resting position.

2.2. OPTICAL CAVITIES

Fabry-Perot interferometers are perhaps the most commonly known type of optical cavities. These consist of two mirrors with reflectivities R_1 and R_2 which are aligned to each other just as in figure 2.1. An incident optical beam that is transmitted through the input mirror undergoes multiple reflections inside the cavity before it couples out of it. The spectrum of a Fabry-Perot cavity results from the interference between all these partially reflected and transmitted beams. Assuming there are no losses, the reflection and transmission spectra are given by [25]

$$R_{\text{lossless}} = \frac{\left(\sqrt{R_1}-\sqrt{R_2}\right)^2 + 4\sqrt{R_1 R_2}\sin^2(\phi)}{\left(1-\sqrt{R_1 R_2}\right)^2 + 4\sqrt{R_1 R_2}\sin^2(\phi)} \tag{2.5}$$

$$T_{\text{lossless}} = \frac{(1-R_1)(1-R_2)}{\left(1-\sqrt{R_1 R_2}\right)^2 + 4\sqrt{R_1 R_2}\sin^2(\phi)} \tag{2.6}$$

where 2ϕ is the phase light acquires after a round-trip inside the cavity. This is usually the sum of the phase shift caused by the reflections at the mirrors and the propagation phase $4\pi nL\cos(\theta)/\lambda$. In this, n is the refractive index inside the cavity, L is the distance between the two mirrors, θ is the angle between light's propagation direction and the cavity axis, and λ is the wavelength of light. From here on we will assume $n = 1$ and $\theta = 0$, i.e. that the cavity is empty and that light propagates parallel to the cavity axis.

Figure 2.2 contains the reflection and transmission of a Fabry-Perot cavity with $R_1 = R_2 = 0.9$ as a function of phase ϕ. The reflection is minimized (and the transmission maximized) when $\phi = q\pi, q \in \mathbb{Z}$. These points are called the cavity *resonances*. Neglecting the phase shifts introduced by the mirrors, the resonance condition can be written as

$$\phi = \frac{2\pi L}{\lambda} = q\pi \Leftrightarrow \nu_q = q\frac{c}{2L} \tag{2.7}$$

where we have used $c = \lambda\nu$. This equation indicates the frequency of the cavity resonances. Notice that the mirror phase shifts would only add a constant offset to all resonance frequencies. The frequency difference between consecutive resonances is $c/2L$, a constant which we name *free spectral range* (FSR).

Another interesting observation from figure 2.2 is that as the mirror reflectivities increase, the resonances become narrower. For high reflectivities, the full width at half

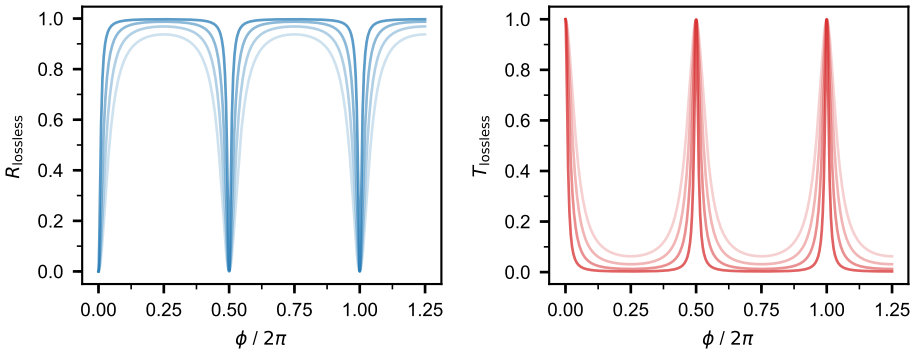

Figure 2.2: Reflection and transmission intensity coefficients of a lossless Fabry-Perot cavity as a function of phase ϕ, according to equations 2.5 and 2.6. The mirror reflectivities are equal ($R_1 = R_2$) and vary from 0.6 (lighter traces) to 0.9 (darker traces).

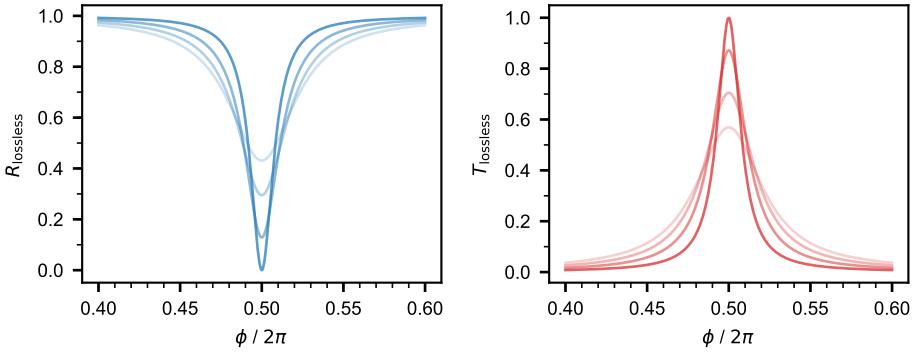

Figure 2.3: Reflection and transmission intensity coefficients of a lossless Fabry-Perot cavity as a function of phase ϕ, according to equations 2.5 and 2.6. The reflectivity of mirror 2 is kept constant at $R_2 = 0.9$, whereas R_1 varies from 0.6 (lighter traces) to 0.9 (darker traces).

maximum (FWHM) of these resonances, expressed in terms frequency, is given by [26]

$$\frac{\kappa}{2\pi} = \text{FSR}\frac{2\pi}{-\ln(R_1 R_2)}. \tag{2.8}$$

The ratio between a cavity's FSR and FWHM is called the *finesse*

$$F = \frac{2\pi\text{FSR}}{\kappa} = \frac{2\pi}{-\ln(R_1 R_2)} \approx \frac{2\pi}{(1-R_1)+(1-R_2)} \tag{2.9}$$

where the approximation assumes that the reflectivities are close to 1. The finesse can be interpreted as the average number of round-trips that a photon travels in the cavity before it is either transmitted through one of the mirrors or lost, for example through absorption or scattering.

When $R_1 = R_2$, $R_{\text{lossless}} = 0$ and $T_{\text{lossless}} = 1$ on resonance. The same does not happen if the mirror reflectivities are different from each other, like represented in figure 2.3. In

this case, the transmission (reflectivity) reaches a lower (higher) value. Analogously to transmission lines, it is common to say that a cavity's mirrors are *impedance matched* or *mismatched* if they are equal or different, respectively. This is typically quantified by the cavity *contrast*, which is defined by $1-R_{\text{lossless}}$ on resonance [27]. This is also colloquially called the reflectivity *dip depth*.

In case there are intensity losses, for example through scattering or absorption at the mirrors or somewhere inside the cavity, the reflected and transmitted powers do not add up to one and so the models must be altered. A simple change which can take losses into account is through adding to the previous equations a round-trip intensity loss $1-A$:

$$R_{\text{lossy}} = \frac{\left(\sqrt{R_1}-\sqrt{R_2}A\right)^2 + 4\sqrt{R_1R_2}A\sin^2(\phi)}{\left(1-\sqrt{R_1R_2}A\right)^2 + 4\sqrt{R_1R_2}A\sin^2(\phi)} \tag{2.10}$$

$$T_{\text{lossy}} = \frac{(1-R_1)(1-R_2)A}{\left(1-\sqrt{R_1R_2}A\right)^2 + 4\sqrt{R_1R_2}A\sin^2(\phi)}. \tag{2.11}$$

Absorption worsens the cavity finesse. Equation 2.9 can be generalized to include losses by defining the round-trip losses $\rho = (1-R_1)+(1-R_2)+A$ as $F = 2\pi/\rho$.

So far the discussion considered a cavity composed of two infinite plane mirrors parallel to each other, with an incident plane electromagnetic wave with wavevector perpendicular to the mirrors. In this case, we can simply describe the cavity modes as plane waves as well. However, in practice mirrors have a finite size and laser beams have a gaussian profile. As a gaussian beam propagates back and forth inside the cavity, its width (in the direction transverse to the cavity axis) increases. If the width is larger than the mirror size, part of the light is lost through *diffraction losses* [25, 26]. Due to this, it is hard to make high finesse cavities with a parallel-plane cavity geometry, since it imposes strict parallelism between the mirrors and also that they have a large area. Instead, one typically uses spherically curved mirrors. In certain conditions, cavities composed of spherical mirrors can have modes which are stable, in the sense that the beam width does not increase after one round-trip and, therefore has lower diffraction losses.

A cavity can sustain stable modes if the condition $0 \leq g_1 g_2 \leq 1$ is met, where $g_i = 1 - L/\text{ROC}_i$ is the stability parameter and ROC_i is the radius of curvature of mirror i [25, 26]. In a plane-parallel cavity $\text{ROC}_i = \infty$, and therefore the above product would be 1, right on the limit of the stability condition. Commonly, stable cavities sustain Hermite-Gaussian modes [25, 26], whose electric field distribution is described by

$$E_{l,m}(x,y,z) = E_0 \frac{w_0}{w(z)} H_l\left(\sqrt{2}\frac{x}{w(z)}\right) H_m\left(\sqrt{2}\frac{y}{w(z)}\right) e^{-\frac{x^2+y^2}{w(z)}} e^{-ikz+i(1+l+m)\eta} \tag{2.12}$$

where z is *longitudinal* direction of beam propagation, x, y are the *transversal* axes, E_0 is the field amplitude, w_0 is the beam waist radius or spot size, $w(z)$ is the radius of the beam at a distance z from the spot, H_j are Hermite polynomials of order j, k is the wavenumber, and $\eta = \arctan\left(\lambda z/\pi w_0^2\right)$. l and m indicate the order of the transversal mode. The cavity spot size w_0 is defined by the geometry of the optical resonator [26]

$$w_0 = \sqrt{\frac{L\lambda}{\pi}} \left[\frac{g_1 g_2 (1-g_1 g_2)}{(g_1+g_2-2g_1 g_2)^2}\right]^{1/4}. \tag{2.13}$$

The last term of equation 2.12 is the phase of the Hermite-Gaussian modes, which include a propagation term $-ikz$, and the Gouy phase $i(1+l+m)\eta$. The latter is an important term which can help us differentiate the behaviour of the multiple transversal cavity modes. By considering its effect on the cavity resonance condition we arrive at an improved description of the cavity spectrum [23, 25, 26]:

$$\nu_{q,l,m} = \frac{c}{2L}\left[q + \frac{1+l+m}{\pi}\arccos\left(\pm\sqrt{g_1 g_2}\right)\right]. \tag{2.14}$$

Each of these modes is an independent peak on the cavity spectrum. When a Gaussian beam is sent to an optical cavity, it is split into all the transversal cavity modes according to the projection of the incident beam to these modes. This projection tells us how much of the incident beam energy propagates in each transversal mode. It also affects the contrast of each resonance. One is usually interested in the situation when most of the incident beam is coupled to the *fundamental* transversal mode $l, m = 0$. For this to happen, the spot of both incident beam and fundamental mode must be located at the same position and must have the same radius w_0. The process of adjusting the incident beam to maximize its overlap with the fundamental cavity mode is called *mode matching*.

2.3. CAVITY OPTOMECHANICS

2.3.1. LINEAR COUPLING HAMILTONIAN

The electromagnetic field can be quantized, giving rise to a description of light as quantum harmonic oscillators with a distribution of single photon energies $\hbar\omega$ [9]. Inside an optical cavity, the energy spectrum is restricted to the cavity modes $\hbar\omega_{q,l,m}$, where $\omega_{q,l,m} = 2\pi\nu_{q,l,m}$ is given by equation 2.14, for the case of a Fabry-Perot cavity. Since we will always be concerned with the same optical mode, the mode indices will be from now on dropped and the cavity mode frequency will be labeled as ω_c. The total energy in a mode is given by the product of the single photon energy with the total number of photons in the mode $\hat{n}_c$. In mathematical form, the Hamiltonian is given by

$$\hat{H} = \hbar\omega_c\left(\hat{n}_c + \frac{1}{2}\right).$$

Recall that even if a quantum harmonic oscillator is not occupied (i.e. if $\hat{n}_c = 0$), it still has a *zero-point energy* of $\hbar\omega_c/2$, as can be read from the previous equation.

In a similar fashion, the motion of a mechanical oscillator can also be quantized. Considering a particular mechanical mode with frequency ω_m and *phonon* number $\hat{n}_m$, the Hamiltonian of a system containing two independent optical and mechanical modes is

$$\hat{H} = \hbar\omega_c\hat{n}_c + \hbar\omega_m\hat{n}_m$$

where the zero point energy $\hbar(\omega_c+\omega_m)/2$ has been dropped.

Consider now the situation in which the optical and mechanical oscillators are somehow coupled. For example, one of the cavity mirrors might be allowed to move, modulating the cavity length and, therefore, the cavity mode spectrum. In such a *dispersive*

cavity optomechanics system, the cavity frequency becomes a function of the mechanical resonator's position x:

$$\hat{H} = \hbar\omega_c(x)\hat{n}_c + \hbar\omega_m\hat{n}_m.$$

We are typically concerned with small mechanical displacements. As such, the previous equation can be approximated by expanding $\omega_c(x)$ into a sum of Taylor polynomials and discarding terms with an order larger than 1, thus arriving at the linear coupling Hamiltonian

$$\hat{H} \approx \hbar\left(\omega_c(0) + \frac{\partial\omega_c(x)}{\partial x}\hat{x}\right)\hat{n}_c + \hbar\omega_m\hat{n}_m = \hbar\omega_c(0)\hat{n}_c + \hbar\omega_m\hat{n}_m + \hbar\frac{\partial\omega_c(x)}{\partial x}\hat{x}\hat{n}_c.$$

$G \equiv \partial\omega_c(x)/\partial x$ is called the *optomechanical coupling strength* and it represents the cavity frequency shift per unit of displacement [28].

Recall that $\hat{n}_c = \hat{a}^\dagger\hat{a}$, where $\hat{a}^\dagger$ and $\hat{a}$ are the creation and destruction ladder operators or the specific light mode we are studying. Similarly, $\hat{n}_m = \hat{b}^\dagger\hat{b}$, where $\hat{b}^\dagger$ and $\hat{b}$ are the ladder operators of the mechanical oscillator. The ladder operators can be used as well to describe the mechanical displacement as $\hat{x} = x_{zpf}(\hat{b}^\dagger + \hat{b})$, where x_{zpf} is the zero-point displacement amplitude, as defined in equation 2.4. The Hamiltonian of the last equation can now be rewritten using the ladder operators as

$$\hat{H} \approx \hbar\omega_c(0)\hat{a}^\dagger\hat{a} + \hbar\omega_m\hat{b}^\dagger\hat{b} + \hbar G x_{zpf}\left(\hat{b}^\dagger + \hat{b}\right)\hat{a}^\dagger\hat{a}.$$

where the first two terms are the uncoupled resonator energies and the last term is the dispersive optomechanical interaction. The product $g_0 \equiv G x_{zpf}$ is called the *vacuum* or *single photon/phonon coupling rate* and it quantifies the cavity frequency shifts due to the mechanical vacuum fluctuations. In other words, it is a measure of the interaction strength between single photons and phonons. g_0 is a particularly useful value which allows comparing optomechanical systems with distinct properties.

It is often relevant to compare g_0 to the cavity linewidth κ. The ratio g_0/κ determines how much the cavity frequency shifts in relation to the cavity linewidth when the mechanical resonator has a displacement of x_{zpf}. If $g_0/\kappa > 1$, the system is said to be *strongly coupled* at the level of single quanta. In this case, a single phonon excitation is able to shift the cavity resonance by more than the cavity linewidth, making the optomechanical interaction non-linear and the system energy spectrum anharmonic [28, 29]. This regime is crucial for quantum optomechanics experiments such as photon blockade or efficient production of non-classical optical and mechanical states [28]. However, apart from atomic clouds [30], all optomechanical systems have so far $g_0/\kappa < 1$. The most common approach to reach single-photon/phonon strong coupling is to maximize the overlap between the optical and mechanical modes, such as with nanobeams or zipper-cavities. Indeed, the best results reported to date are with slotted photonic crystal cavities with $g_0/\kappa = 2\times10^{-3}$ [20, 31]. This is still far from strong coupling and there is an intense research effort in the field to reach this regime.

The following subsections discuss the situations in which one or more mechanical resonators are placed in the middle of an optical cavity, with a focus on calculating the optomechanical coupling strength of both systems. Interestingly, the relative motion

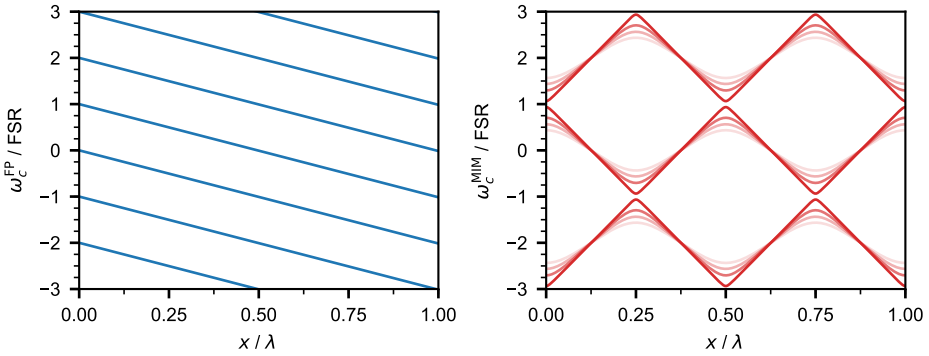

Figure 2.4: Frequency of several consecutive longitudinal modes of a Fabry-Perot (left) and MIM (right) as a function of mirror and membrane displacement, respectively. The displacement is normalized by the laser wavelength. Both cavities have the same length. The frequencies are subtracted by the laser frequency and normalized by the FSR. The membrane reflectivity $|r_m|^2$ takes the values 0.4 (lighter traces), 0.6, 0.8 and 0.99 (darker traces).

between multiple mechanical resonators has a coupling strength that scales very favorably with the reflectivity of the individual elements, offering a promising path towards reaching the strong coupling regime.

2.3.2. FABRY-PEROT

The previous subsection did not specify an equation for the optomechanical coupling strength G since this is dependent on the details of the particular system one is interested in. One of the simplest cases is that of a Fabry-Perot cavity in which one of the mirrors can move, such as represented in figure 2.1. In that situation, the frequency of a particular cavity mode is $\omega_c^{FP}(x) = 2\pi qc/2(L+x)$ (eq. 2.14) where q is the index of the longitudinal mode which is being studied (assuming that this is the fundamental transversal mode and ignoring additional frequency offsets) and x is the displacement of the mirror from the average cavity length L. With this we have direct access to the coupling strength of a Fabry-Perot:

$$G_{FP} = \frac{\partial \omega_c^{FP}(x)}{\partial x} = 2\pi \frac{\partial}{\partial x} \frac{qc}{2(L+x)} = -\frac{\omega_c^{FP}(x)}{L+x} = -4\pi \frac{FSR}{\lambda} \tag{2.15}$$

where $c = \lambda \omega_c^{FP}/2\pi$. The left plot of figure 2.4 shows the cavity frequency for a few consecutive longitudinal FP cavity modes as a function of displacement of one of the mirrors. Since the displacement is typically very small in comparison to the cavity length, the cavity frequencies appear to decrease linearly with displacement with a constant rate G_{FP}.

2.3.3. MEMBRANE-IN-THE-MIDDLE

One extension of the simple Fabry-Perot cavity is the case when the mirrors are fixed rigidly but a mechanical resonator is placed in the middle of it. The first experiments of this type used a *membrane in the middle* (MIM) of an optical cavity [14, 32], but the

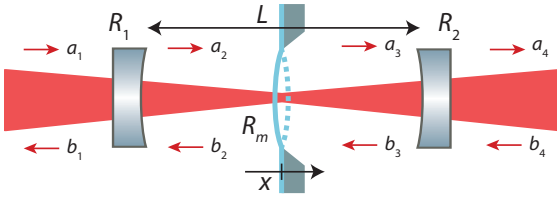

Figure 2.5: Schematic representation of a membrane with reflectivity $R_m = |r_m|^2$ in the middle of a Fabry-Perot optical cavity, composed of two mirrors with reflectivities R_1 and R_2. The mirrors are fixed at a distance L between each other. The membrane can undergo displacements of amplitude x around its resting position.

mechanical element can also be a nanosphere, a cantilever, or any other type of mechanically compliant scatterer [33]. This is schematically represented in figure 2.5. As the membrane moves along the cavity axis, it changes the boundary conditions of the electric field and, consequently, the optical spectrum. One advantage of a MIM system is that the mechanical and optical properties can be decoupled from each other. This means that in principle one can study a mechanical element with arbitrary characteristics and change the cavity finesse independently, whereas in other systems these two are often coupled together and suffer from technical trade-offs.

To obtain an expression for a MIM's cavity frequency as a function of the membrane's position $\omega_c^{\mathrm{MIM}}(x)$ and, consequently, the optomechanical coupling strength G_{MIM}, we analyze the system in one dimension (along the cavity axis) and separate the electromagnetic field into forward and backward propagating planewaves in different regions, labelled by the index i. The waves share the same propagation constant $|k| = \omega_c/c$ but have different amplitudes a_i and b_i, as indicated in figure 2.5. In the paraxial beam approximation, this type of problem can be solved using the transfer matrix method [25, 34–36]. For this the system is separated into individual building blocks, such as free-space propagation and scattering. Each of these can be described by a 4×4 matrix M which, when applied to the field amplitudes on one side i of the block, outputs the field on the opposite side $i-1$:

$$\begin{bmatrix} a_{i-1} \\ b_{i-1} \end{bmatrix} = M \begin{bmatrix} a_i \\ b_i \end{bmatrix}.$$

The free-space propagation over a distance d can be represented by the matrix

$$M_{\mathrm{p}}(d) \equiv \begin{bmatrix} e^{ikd} & 0 \\ 0 & e^{-ikd} \end{bmatrix}$$

and the scattering at an infinitesimally thin element with amplitude reflection and transmission coefficients r and t by

$$M_{\mathrm{s}}(r,t) \equiv \frac{1}{t}\begin{bmatrix} t^2-r^2 & r \\ -r & 1 \end{bmatrix}.$$

We can now transform the MIM into a product of these two matrices:

$$\begin{bmatrix} a_{\mathrm{in}} \\ b_{\mathrm{r}} \end{bmatrix} = M_{\mathrm{s}}(r_{\mathrm{M}},t_{\mathrm{M}})M_{\mathrm{p}}(\frac{L}{2}+x)M_{\mathrm{s}}(r_{\mathrm{m}},t_{\mathrm{m}})M_{\mathrm{p}}(\frac{L}{2}-x)M_{\mathrm{s}}(r_{\mathrm{M}},t_{\mathrm{M}})\begin{bmatrix} a_{\mathrm{t}} \\ 0 \end{bmatrix} = M_{\mathrm{MIM}}\begin{bmatrix} a_{\mathrm{t}} \\ 0 \end{bmatrix}$$

where r_M and t_M are the amplitude reflection and transmission coefficients of the mirrors and r_m and t_m those of the membrane. x is the displacement of the membrane from the center of the cavity. We assume that the mirrors have the same amplitude reflection and transmission coefficients, and that they are lossless (i.e. $|r_M|^2 + |t_M|^2 = 1$). The membrane transmission and reflection coefficients are given by [37, 38]

$$t_m = \frac{2n}{2in\cos(knl) + (n^2+1)\sin(knl)}, \quad r_m = \frac{(n^2-1)\sin(knl)}{2in\cos(knl) + (n^2+1)\sin(knl)}$$

where n is the refractive index and l the thickness of the membrane.

Having defined the matrix M_{MIM}, the overall amplitude transmission t_{MIM} and reflection r_{MIM} of the system can be calculated by taking the matrix elements $M^{\alpha,\beta}_{MIM}$ as follows [34]:

$$t_{MIM} = \frac{1}{M^{2,2}_{MIM}}, \quad r_{MIM} = \frac{M^{1,2}_{MIM}}{M^{2,2}_{MIM}}. \tag{2.16}$$

Thus using this method one can obtain a full description of the MIM system. It should be pointed out that it is not necessary to assume that the mirrors are lossless nor that they have the same transmission and reflection coefficients. However, these assumptions strongly simplify the analysis and they do not impact the cavity resonance frequencies, which is what we are interested in finding. These frequencies can be found by maximizing $|t_{MIM}|^2$, which gives [37, 39]:

$$\omega_c^{MIM}(x) = 2\pi \mathrm{FSR}\left[q + \frac{(-1)^q}{2} - \frac{(-1)^q}{\pi}\arccos\left(|r_m|\cos\left(\frac{4\pi x}{\lambda}\right)\right)\right] \tag{2.17}$$

where q is the index of the mode. This expression assumes that the membrane is lossless, i.e. that $|r_m|^2 + |t_m|^2 = 1$. The right plot of figure 2.4 represents $\omega_c^{MIM}(x)$ for different membrane reflectivities $R_m = |r_m|^2$. Just as expected, equation 2.17 reduces to the frequency of an empty Fabry-Perot (eq. 2.7) when $r_m = 0$, with equally spaced longitudinal modes and no dependency in the displacement of the fully transparent membrane. However, if the membrane is reflective, the behavior of a MIM is markedly different. There are two regimes which are particularly interesting.

The first is the regime for which the cavity frequency depends linearly on the displacement. This occurs for small displacements close to $x = \lambda/8 + n\lambda/4, n \in \mathbb{Z}$. Around these positions, the first derivative of the cavity frequency, which was defined in subsection 2.3.1 as the linear coupling strength, is given by

$$G_{MIM} = \max\left(\left|\frac{\partial \omega_c^{MIM}(x)}{\partial x}\right|\right) = 8\pi\frac{\mathrm{FSR}}{\lambda}|r_m| = 2G_{FP}|r_m|. \tag{2.18}$$

From the last equality we learn that the coupling strength of a MIM system can be twice as high as that of a Fabry-Perot with the same cavity length, if the reflectivity of the membrane is large enough.

The second regime of interest occurs around $x = \lambda/4 + n\lambda/4, n \in \mathbb{Z}$. For small displacements around these positions, the first derivative of $\omega_c^{MIM}(x)$ vanishes and the frequency depends *quadratically* on the displacement. Just as for the linear coupling, we

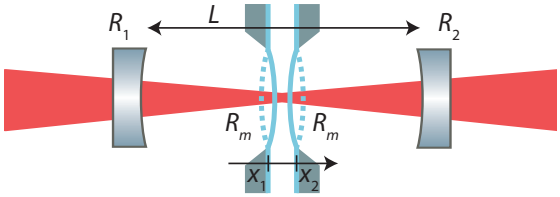

Figure 2.6: Schematic representation of a membrane with reflectivity $R_m = |r_m|^2$ in the middle of a Fabry-Perot optical cavity, composed of two mirrors with reflectivities R_1 and R_2. The mirrors are fixed at a distance L between each other. The membrane can undergo displacements of amplitude x around its resting position.

can define a quadratic coupling strength [28, 32]

$$G^{(2)}_{\mathrm{MIM}} = \max\left(\left|\frac{\partial^2 \omega_c^{\mathrm{MIM}}(x)}{\partial x^2}\right|\right) = 32\pi^2 \frac{\mathrm{FSR}}{\lambda^2} \frac{|r_m|}{\sqrt{1-|r_m|^2}}$$

and a quadratic vacuum coupling rate $g_0^{(2)} = G^{(2)}_{\mathrm{MIM}} x^2_{\mathrm{zpf}}$.

It is interesting to note that by displacing the membrane by $\lambda/8$, the system's main coupling mechanism can be easily tuned from linear to quadratic. This is another advantage of the MIM platform, which is not easily achievable in other systems. The quadratic coupling regime offers different physics which do not have as much attention in the optomechanics community. Also in this thesis we will focus our attention on the properties of the linear MIM coupling.

2.3.4. OPTOMECHANICAL ARRAYS

From the previous subsection we learned that G_{MIM} increases with the membrane amplitude reflectivity coefficient. This can also be seen in figure 2.4. However, this scaling is linear, which means that only modest gains can be made even with highly reflective membranes. In fact, the best reported g_0/κ MIM ratios are of the order of 10^{-4} which is still quite far from the strong coupling regime [14, 40].

Curiously, some theoretical proposals predict that variations of the MIM configuration can result in strongly enhanced linear optomechanical coupling strengths and, consequently, may provide a path towards strong coupling [21]. These consist in placing more than one scattering element with similar mechanical and optical properties in the middle of a cavity. If the scatterers are somehow coupled together, for example through the electromagnetic field that travels between them, their motion can be described by a set of collective motional modes. We will discuss the coupling of two particular collective modes of motion to the optical cavity: the *center-of-mass* (COM) mode, in which the membranes move synchronously with each other, and the *relative* or *breathing* mode, in which the COM remains constant but the distance between membranes oscillates.

Figure 2.6 represents such an *optomechanical array* for the particular case of two membranes in the middle of a cavity. We assume that the membranes have the same amplitude reflectivity r_m and mechanical properties. The membranes have an initial spacing between them of l and can undergo displacements of x_1 and x_2 in relation to their resting positions. Defining the position of mirror 1 as the origin of the x axis, the

COM can be found from $L/2 + x_1 + x_2$, whereas the relative distance between the membranes is given by $l + x_2 - x_1$. Similarly to the previous subsection, this problem can be solved using the transfer matrix method. The matrix which defines the whole system is

$$M_s(r_M, t_M)M_p(\frac{L-l+x_1}{2})M_s(r_m, t_m)M_p(l+x_2-x_1)M_s(r_m, t_m)M_p(\frac{L-l-x_2}{2})M_s(r_M, t_M)$$

and the cavity frequency can be calculated once again from the maxima of the transmission function (c.f. equation 2.16). Several papers discuss this and alternative methods of obtaining the cavity frequency of an optomechanical array [21, 38, 39, 41, 42], but in this thesis we will only reproduce the results more relevant to us, pertaining to the optomechanical coupling strength of the COM and relative modes of motion.

The two-membrane array can be seen as a shorter Fabry-Perot etalon. As such, the spacing between the membranes will define the reflectivity r_T of the stack. If the membranes move synchonously, the spacing between them and, consequently, the reflectivity, remains constant. As such, the COM motional mode couples to the cavity in a similar fashion to a MIM. The COM coupling strength takes a similar form to equation 2.18 but the reflectivity is now that of the stack of membranes [21]

$$G_{CM} = 8\pi \frac{\mathrm{FSR}}{\lambda} |r_T| = 2G_{FP}|r_T|. \tag{2.19}$$

When using low reflectivity membranes, G_{CM} is can be larger than G_{MIM} since, in that case, $|r_T|$ can be higher than $|r_m|$. However, by adding a membrane, the system's total mass doubles. Therefore, the optomechanical coupling rate becomes

$$g_0^{CM} = 2G_{FP}|r_T| \frac{x_{zpf}}{\sqrt{2}}$$

where x_{zpf} is that of a single membrane. If $|r_m|$ is close to 1, g_0^{CM} is actually lower than g_0^{MIM} by a factor of $\sqrt{2}$. In a more general way, although G_{CM} does not depend directly on the number of membranes used (but indirectly through the total reflectivity) the coupling rate of a stack with N similar membranes scales as

$$g_0^{CM} = 2G_{FP}|r_T| \frac{x_{zpf}}{\sqrt{N}}$$

where x_{zpf} is that of a single membrane.

For the COM mode, the membranes move synchonously and the distance between them is fixed. Therefore, the reflectivity of the membrane stack remains constant. In contrast, for the relative motional mode, the COM is fixed but the distance between the membranes oscillates. As a consequence, the reflectivity of the stack varies more strongly, introducing larger optical phase shifts and, thus cavity frequency oscillations. This effect is most pronounced for small displacements around a certain spacing l for which the membrane array is optically transmissive. In this case, the coupling strength is [39]

$$G_{rel} = 2G_{FP}\frac{|r_m|}{1-|r_m|}. \tag{2.20}$$

The previous equation is valid only for reflectivity values not too close to 1. We can see that the coupling strength scales very favourably with the single membrane reflectivity. As the reflectivity approaches 1, the coupling strength is capped at [38]

$$G_{\mathrm{rel}}^{\mathrm{max}} \approx G_{\mathrm{FP}} \frac{L}{l} = G_{\mathrm{MIM}} \frac{L}{2l}. \tag{2.21}$$

This means that the coupling of the relative motion between two membranes is enhanced by a factor of $L/2l$ in comparison to the coupling of a single MIM, when the membrane reflectivity is close to 1. This enhancement factor is geometrically defined and if the membranes are placed close together in the middle of a long cavity, one could aim at achieving coupling rates close to the strong coupling regime. As opposed to the COM coupling, this effect scales favourably with the number of membranes in the array, with a factor of $N^{3/2}$ [21].

In conclusion, we have seen that the optomechanical coupling between the relative motion of an array of membranes in the middle of an optical cavity can be very large, provided that the membranes are close together and that their reflectivity is very high. The challenge lies in successfully creating such structures while maintaining good mechanical properties. This thesis contains a series of experiments that culminates in an optomechanical array of two highly reflective membranes which paves the way towards the observation of coupling enhancement in the context of optomechanical arrays.

3

METHODS

THE goal of this thesis is to develop and study mechanical resonators for optomechanical experiments in membrane- or array-in-the-middle configurations. This chapter contains a description of the devices that were used, in particular in what concerns their design and fabrication. It also discusses the most important methods and techniques used to perform the studies presented in the following chapters: two setups used to test and characterize devices in terms of their mechanical and optical properties, followed by a cavity setup, whose goal is to perform optomechanical experiments.

3.1. DEVICE DESIGN AND FABRICATION

3.1.1. DESIGN

The first membrane-in-the-middle (MIM) experiments were performed using square membranes made of suspended silicon nitride (SiN) films [14, 37]. These films are typically created using low pressure chemical vapor deposition (LPCVD) on top of a crystalline silicon (Si) substrate. With this technique it is possible to obtain SiN films with large intrinsic stress (~ 1 GPa), high purity and smooth surfaces. Due to these properties, SiN square membranes can have large mechanical quality factors of 1×10^6 at 1 MHz and low optical losses (imaginary part of the refractive index of $\sim 1 \times 10^{-6}$ at 1550 nm). This makes them very interesting objects of study for MIM optomechanics experiments.

Recently many groups started exploring if and how the mechanical dissipation of such devices could be improved even further. One possible approach is to design a structure around the membrane which impedes the leaking of phonons around the mechanical resonance frequency which one is interested in interacting with. These *phononic shields* effectively try to create a bandgap to avoid mechanical excitations from propagating.

A different approach is to change the geometry of the membrane and its connections to the substrate in order to lower the mechanical dissipation through *stress engineering*. This is the approach followed in this thesis. We suspend square membranes with a side length of 100 ~ 300 µm using four ~ 10 µm-wide tethers connected to the

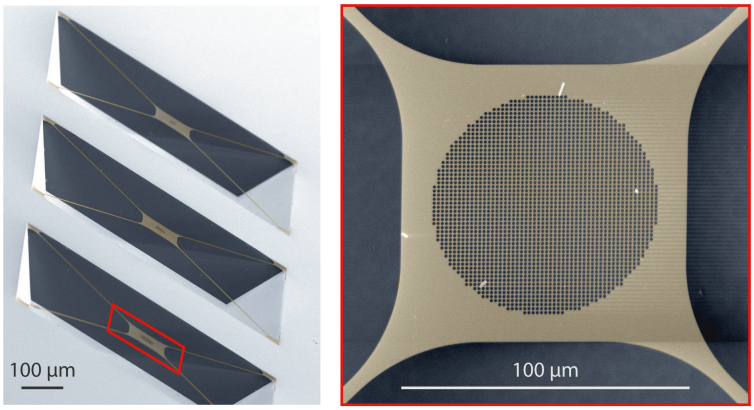

Figure 3.1: False-colored scanning electron microscope picture of three trampoline membranes fabricated on the same Si substrate. The membranes patterned onto LPCVD SiN and suspended by four tethers. The right figure is a zoom-in of one of the membranes, where the PhC pattern can be seen.

substrate. Figure 3.1 shows examples of this type of *tethered* or *trampoline membranes*. Chapter 4 explores in more detail the loss mechanisms of this type of structure and how their mechanical decay can be optimized to be at least two orders of magnitude better than simple square membranes at the same fundamental resonance frequency.

In addition to manipulating the mechanical properties of SiN membranes, we study and tailor their optical spectrum using *photonic crystals*. The following subsections explain their principle of operation, as well as how the devices are fabricated.

3.1.2. PHOTONIC CRYSTAL SLABS

As mentioned on the introduction, the mechanical resonators studied in this thesis are thin silicon nitride membranes and we interact with them using perpendicularly incident optical beams. The reflectivity spectrum of such a thin film is well modelled by a low finesse Fabry-Perot etalon (see section 2.2) in which the refractive index inside the etalon is that of silicon nitride ($n \approx 2$ at $\lambda = 1550\,\text{nm}$ [43]) and the reflectivity of the interfaces $R = 0.11$ can be calculated through Fresnel's equations [44]. For a wavelength of 1550 nm, the reflectivity is a function of film thickness t, with a period $\lambda/2n = 387.5\,\text{nm}$, and reaches its first maximum of 0.6 at $\lambda/4n = 193.75\,\text{nm}$. Two problems arise. First, one is often interested in using films thinner than 193.75 nm, for reasons which will become clear on chapter 4. Second, for some applications it is crucial to have membrane reflectivities much higher than 99 %.

To get around these issues, we pattern a square array of holes on the thin film in order to create a photonic crystal (PhC) slab [45, 46]. The left side of figure 3.2 represents a unit cell of such a device. The cylindrical holes have a radius r and are patterned with a period a (also called the *lattice parameter*) onto a membrane with thickness t. Figure 3.2 (right) contains a cross-section view of a PhC slab. Suppose the device interacts with a plane-wave with an incident wavevector $\vec{k}_i$. If the slab was not patterned with the PhC, its reflection $\vec{k}_r$ and transmission $\vec{k}_t$ would be well modeled from the Fabry-Perot etalon

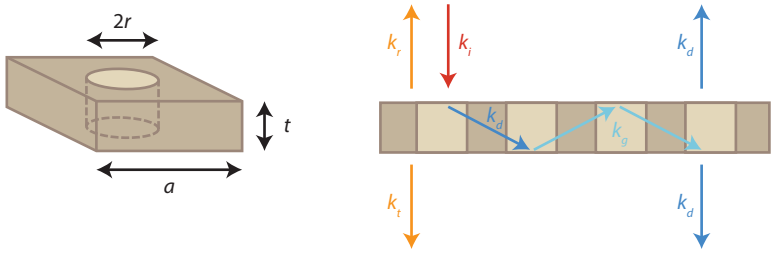

Figure 3.2: Left: unit cell of a photonic crystal slab. The crystal consists on a series of cylinders with radii r etched with a periodicity a onto a film with thickness t. Right: cross-section of a PhC slab and representation of the wavevectors involved in the resonant response of the device.

model (eqs. 2.10 and 2.11). In addition, the slab supports in-plane guided modes, represented by $\vec{k}_g$. The photonic crystal functions as a grating which diffracts the incident beam and the guided modes. The diffracted wavevectors $\vec{k}_d$ depend on the geometry of the PhC. By careful design, it is possible to modematch the incident and guided modes, resulting in an efficient coupling between $\vec{k}_i$ and $\vec{k}_g$, as well as between $\vec{k}_g$ and $\vec{k}_{r,t}$ [47]. The interference between the highly resonant light which leaks out of the guided modes with broadband direct reflection and transmission of the thin film results in spectral features which resemble Fano resonances [48].

The plot in figure 3.3 is an example of the reflection spectrum of such a PhC slab. Due to the symmetry of the unit cell, this type of structure is polarization independent for normal incidence. The resonance wavelength λ_{PhC} is defined by the geometrical parameters of the slab. To find geometries for which λ_{PhC} is close to our operating wavelength of 1550 nm, we use simulation softwares which are able to estimate the spectrum of PhC slabs. For this we have used Lumerical [49], a commercial simulator based on the finite-difference time-domain (FDTD) method, as well as a S^4 [50], an open-source rigorous coupled-wave analysis (RCWA) solver. These programs calculate the optical response of a PhC slab when a plane wave of a given wavelength is incident on it.

With FDTD, the space is discretized and Maxwell's equations are solved by approximating the derivatives as central-differences. This process is repeated such that the time and space propagation of an electromagnetic wave incident on a PhC can be obtained. With this method one can simulate the response of a short pulse incident on a PhC. By Fourier transforming the time response we obtain the frequency spectrum. This makes it a simple method to calculate the spectrum over a large range of wavelengths with a single simulation. In addition, it is possible to simulate a whole structure composed of many unit cells, as well as to define multiple types of incident beams, such as plane-waves or Gaussian beams. Since the whole space and time must be discretized, this comes at the cost of long simulation durations and large memory consumption.

By contrast, the RCWA method simulates the response of plane-waves incident on the unit cell of a longitudinally periodic structure. The software divides the unit cell into multiple layers (such as vacuum or silicon nitride) which can have arbitrary geometries in the longitudinal directions. It then calculates the modes of the electromagnetic field in each of the layers and solves the boundary conditions at the interfaces between lay-

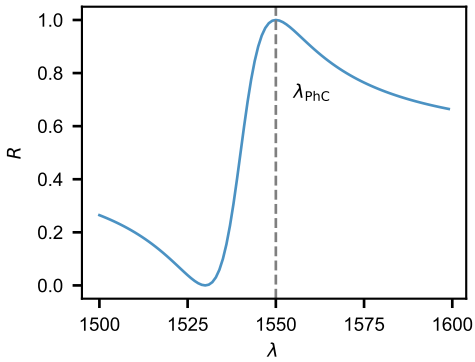

Figure 3.3: Example of the reflection spectrum of a PhC slab, resembling a Fano resonance, with resonance wavelength λ_{PhC}.

ers, assuming uniformity in the z direction and periodicity at the edges of the unit cell. The reflected and transmitted waves are calculated as the sum of the electromagnetic modes. The user must choose how many modes to use from the infinite basis of the electromagnetic field. For simple structures, such as the PhCs used in this work, only a small number of modes are necessary to accurately simulate the spectrum. Because of this, and since it does not require a fine discretization along the z direction, RCWA can be more efficient than FDTD. Each simulation calculates the electromagnetic field for a specific wavelength. This can be repeated over the desired wavelength range.

When designing a PhC membrane, we start with a known device thickness and desired resonance wavelength. We then run an algorithm which optimizes the lattice constant a and hole radius r for which the spectral response of a plane wave perpendicularly incident on a unit cell of a PhC with those dimensions has a resonance wavelength close to the desired one. Given the simplicity of our structure and simulation, FDTD and RCWA require similar computational times and therefore we have used both methods for this application.

In some cases, we would like to study how a Gaussian beam, and not a simple plane wave, interacts with the sample. If performed with FDTD, this would be computationally expensive, since it would have to simulate a space with a volume considerably larger than the actual Gaussian beam waist. Furthermore, each simulation would be specific to a given beam waist. We know, however, that a Gaussian beam (and other types of beams) can be composed from an infinite sum of plane waves with a continuous (Gaussian) distribution of wavevector angles. As such, one can simulate the spectrum of many plane waves incident on the PhC unit cell at different angles and later recreate the response of Gaussian beams with arbitrary waist radii. Each plane wave simulation is computationally cheap and can be reused later for the recreation of any type of beam. This method is explained in more detail on chapter 5.

3.1.3. FABRICATION

This section describes the fabrication process in general terms. A more detailed discussion can be found in [51]. The essential steps to fabricate a tethered SiN membrane are:

1. SiN deposition

   The fabrication process starts with the preparation of the substrate. We use double-side polished silicon (Si) substrates, with the crystal orientation ⟨100⟩ and a thickness ranging from 100 µm to 1 mm. The substrates are cleaned with RCA-1 and -2 processes, which remove organic and ionic contaminants, as well as stripping the oxidized surface layer. Using low pressure chemical vapor deposition (LPCVD), a thin silicon nitride (SiN) layer is uniformly deposited on top of the Si substrates at a temperature of 800 °C (fig. 3.4a). After deposition, the substrate is slowly cooled down. Due to their difference in thermal expansion coefficients, as the chip cools down, SiN contracts more than Si, resulting in a net tensile stress of the thin film at room temperature. Depending on the exact recipe, the stoichiometry of the film can be controlled, as well as its final intrinsic stress. Using this technique we can deposit films with a thickness between 25 and 300 nm and about 1 GPa of intrinsic stress.

2. Lithography

   The SiN layer is patterned using electron beam lithography. For this, a 500 nm-thick layer of positive electron beam resist (AR-P 6200) is spun on the chip (see fig. 3.4b). The trampoline and PhC patterns are exposed on the resist layer using a Raith EBPG 5200 lithography system. We typically write an array of 3×3 devices on a single chip. With this we can either sweep some parameter of the device geometry, or make 9 similar ones to test consistency of properties. The areas of the resist exposed to the electron beam are developed using pentyl acetate (fig. 3.4c).

3. SiN etching

   The resist pattern is transferred on to the SiN layer using reactive ion etching (see fig. 3.4d). In particular we create a plasma of C_4F_8/SF_6 or CHF_3 using an inductively coupled reactive ion etcher, which etches the SiN both physically and chemically. Once the pattern is transferred, the electron beam resist is stripped with an O_2 plasma and a piranha (H_2SO_4/H_2O_2) solution (fig. 3.4e). Often it is also necessary to pattern the SiN layer of the opposite side. In that case, we repeat the lithography and SiN etching steps, taking care to protect the already patterned layer with resist to minimize harm or contamination.

4. Si etching

   The Si between the two thin film SiN layers is removed using a KOH wet etching step (fig. 3.4f). We typically perform this process with a KOH concentration of 30 % in weight and at 70 °C, which results in a Si etching rate of 44.5 µm/h along the ⟨100⟩ direction. The residuals from KOH etching are cleaned using a solution of HCl. Furthermore, organic residues from any of the previous steps can be cleaned using a piranha solution. During this step, the SiN patterns are suspended and

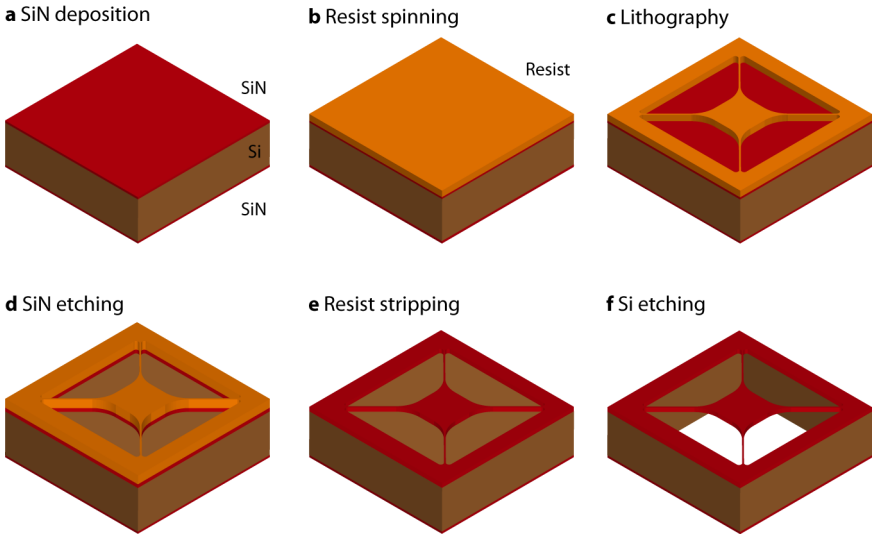

Figure 3.4: Schematic representation of the essential steps for the fabrication of tethered SiN membranes. Adapted from [51].

therefore the chip must be handled with great care. Some of the structures which we fabricate are very sensitive to shocks and surface tension forces between liquids. Particular attention must be given to the way the samples are dried. For this we use critical point drying, which greatly decreases the exposure of the sample to large surface tension forces and to the commonly used N_2 blow drying.

Since we typically alter the geometry of the trampolines and the photonic crystal patterns in almost every sample iteration, it is more useful to work with small chips rather than a whole wafer. Therefore, we perform the SiN deposition on a $4''$ wafer, since this step is common to every chip with the same thickness, which we afterwards dice into $10 \times 10\,\mathrm{mm}^2$ chips. Before dicing, we cover the wafer with photoresist on both sides to protect the surfaces from scratches and contamination during dicing and handling. The protective photoresist coating is stripped using acetone immediately before each chip is used in a lithography step. If after stripping the chip still looks to have contaminated spots, it is cleaned using a piranha solution.

If only one side of the chip were to be patterned with a trampoline, after the Si etching the unpatterned side would have a suspended square SiN membrane. To obtain a trampoline with clear optical access on both sides, we must also perform a lithography and SiN etching step on the side opposite to the trampoline. For single-trampoline devices, we simply pattern a square on the side opposite to the device. This way, during the Si etching, both sides of the chip are etched simultaneously, making this step take half as long as if only one side were to be patterned.

In fact, it is crucial to minimize the Si etching time. Even though KOH etches Si anisotropically, it is not perfectly selective to a single crystal orientation. In particular, the etch rate ratio between the $\langle 100 \rangle$ and the $\langle 111 \rangle$ directions, which correspond to the

perpendicular and parallel directions to the chip surface, is about 74:1. This results in a small *overhang* around the trampolines which has a strong impact in the mechanical properties of the devices. One method to decrease the overhang substantially is to use a special chip holder which isolates the trampoline side and only exposes the opposite one to the etchant [52]. With this, the process can be stopped as soon as the KOH etches the Si underneath the trampoline, minimizing that side's exposure to KOH and therefore the overhang. However, this method is often cumbersome and time-consuming.

As it was briefly mentioned, the devices must be handled with care once suspended. Whereas 200 to 50 nm devices are notoriously robust, mishandling thinner ones results in unwanted consequences. The worst case is when the trampoline rips or shatters. Often, however, the device remains intact but with poor mechanical properties. As such, we take great care to avoid shock collisions of the chip holder, strive to move the chip as slowly as possible when immersed in liquids, and use critical point drying.

Finally, one must highlight the importance of cleanliness during the whole fabrication process. Any impurity that lays on the trampoline membranes, in particular on its tethers, will strongly cripple its mechanical properties. Our recipes therefore include many cleaning and optical analysis steps to ensure that the chips are clean. The challenge lies in guaranteeing that this is true over the majority of the chip, since our devices span much larger areas than what is typical in other photonics applications. One detail which is often overlooked is the drying step. If not done properly, whenever drying a chip which was immersed on some liquid there is a chance of leaving residues on the surface which might be hard to later remove. Water is particularly hard to dry properly. As such, we try to always transfer the chip to a beaker with isopropyl alcohol, which has a much lower surface tension and is therefore easier to dry.

3.2. MECHANICS CHARACTERIZATION SETUP

In order to characterize the mechanical resonators studied in this thesis, we have built a dedicated setup based on the optical readout of the devices' displacement. When a laser beam is reflected off a sample, its phase $\phi(t)$ depends on the device's position $x(t)$ as $\phi(t) = 2\pi x(t)/\lambda$, where λ is the laser wavelength. In other words, the device's movement changes the optical path of the reflected beam and, consequently, its phase in relation to a fixed reference. The Fourier transform of the phase oscillations give us access to information about the mechanical resonances of the device.

Photodetectors are sensitive to light's intensity but not its phase. Typically, in order to measure the phase of an optical beam, one interferes it with a reference beam which does not interact with the sample. The two beams interfere, which translates phase differences between them into intensity variations, which can be measured with a photodetector. If all other sources of phase oscillations are small or if they affect both beams equally, then the phase difference between the two will primarily include signatures of the sample. Perhaps the best known interferometry techniques are the Michelson and Mach-Zehnder interferometers. Here we use a different technique, named Balanced Homodyne Detection, which is described in the following subsection.

The setup is schematically represented in figure 3.5. For probing the mechanical displacement we use a fiber coupled laser tunable from 1520 to 1570 nm (New Focus Vidia-Discrete 6427). Only 10 % of this laser's power is used to probe the sample, whereas 90 %

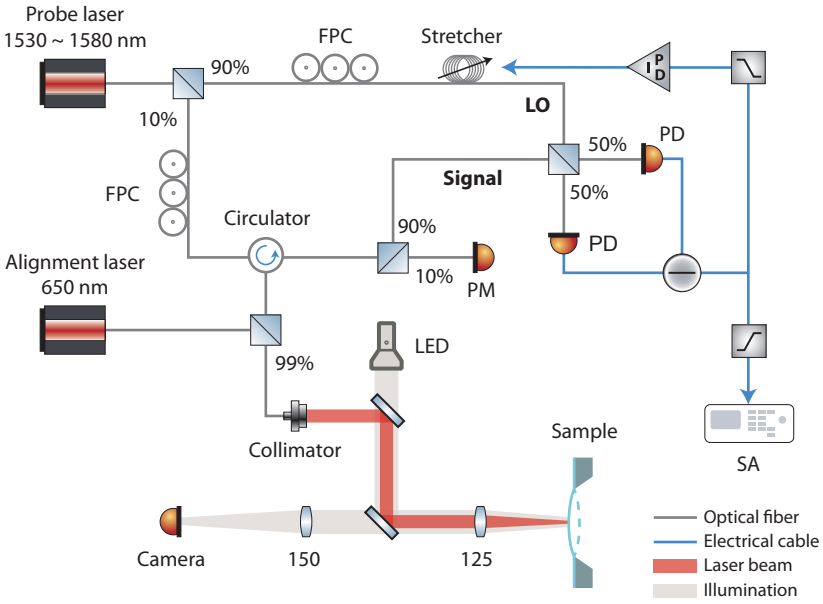

Figure 3.5: Schematic of the mechanics characterization setup. FPC: fiber polarization controller; PID: proportional, integral, differential controller; SA: spectrum analyzer; PM: powermeter; PD: photodiode.

is used as an interference reference (local oscillator). The probe goes through a fiber polarization controller (FPC) and a circulator. After, it is combined with a 650 nm laser. Although the optical components are designed for 1550 nm, they still allow the propagation of this red laser, which coarsely follows the path of the probe and, therefore, is used as an alignment aid, since 1550 nm is not visible by naked eye nor by Si cameras. The laser beams are coupled to free-space using a Thorlabs TC12APC-1550 triplet collimator, with an output waist radius of 1.14 mm, and aligned to the sample with the help of two steering mirrors. We focus the beam with a $f = 125$ mm lens, resulting in a spot of 55 µm at the sample. The beam is aligned to be perpendicular to the sample's surface, such that the light reflected from it couples efficiently back into the fiber collimator. The beam goes once again through the circulator and 90 % of it is used as a signal, while 10 % is measured by a powermeter (PM), which is useful during alignment.

In order to see the sample which is being measured, we set up a simple imaging system. A white LED is coupled to the beam path through one of the steering mirrors, whose back surface is unpolished, working as a light diffusing element. Light reflected from the sample is focused on a Si camera. Together with the alignment laser, this allows us to identify the positions of the probe beam and the sample.

The sample sits on two stick-slip piezoelectric translation stages from Physik Instrumente (Q-521). These stages have a travel range of 32 mm in both directions of the plane perpendicular to the laser beam, making it possible to study four different $10 \times 10\,\text{mm}^2$ chips with multiple devices on each. We add a gold sputtered chip to the stage, which provides a large, highly reflective surface with no topographical features, which greatly

aids in the alignment of the laser beam to the translation stage plane. We also clamp a small piezoelectric to the chip stage, which can be used to mechanically drive the samples.

The sample and stages are placed inside a vacuum chamber, which, with the aid of a turbomolecular and a Roots pump, is able to achieve pressures as low as 1×10^{-8} hPa. This is a particularly crucial component of the setup since, otherwise, the main damping mechanism of samples with low intrinsic mechanical losses would be viscous drag from collisions with surrounding gas molecules. The chamber can be pumped down close to base pressure in approximately 2 h. Together with the large stage which allows us to move between multiple chips in a single pump-down, this constitutes a practical setup to quickly test devices with high mechanical quality factors. This was an important factor for the experiment in chapter 4.

3.2.1. BALANCED HOMODYNE DETECTION

Balanced homodyne detection (BHD) is an interferometry technique which allows measuring the field quadratures of a weak *signal* beam in relation to a stronger one, the *local oscillator* (LO). The measured quadrature is defined by the phase difference between both beams at low frequencies which can be arbitrarily chosen. In fact, this technique is commonly applied in quantum optics to tomographically measure the quadratures of signals with quantum properties, such as vacuum or squeezed states, which gives access to their probability density distributions [53].

In a BHD we assume the signal ($\alpha_s(t)$) and LO ($\alpha_{LO}(t)$) field amplitudes to be described by

$$\alpha_s(t) = \overline{\alpha}_s + \delta X_s(t) + \delta Y_s(t)$$
$$\alpha_{LO}(t) = \left[\overline{\alpha}_{LO} + \delta X_{LO}(t) + \delta Y_{LO}(t)\right] e^{i\phi}$$

where $\overline{\alpha}_i$ represents the average vector of field $i \in \{s, LO\}$, $\delta X_i(t)$ and $\delta Y_i(t)$ are small fluctuations of the field quadratures around the respective average, and ϕ is the phase difference between both fields. We assume that $\overline{\alpha}_s$ is parallel with $\delta X_s(t)$, which means that $\delta X_s(t)$ can be interpreted as *amplitude* and $\delta Y_s(t)$ as *phase* fluctuations of the signal field. In the experiments described in this work, we are generally interested in measuring the phase oscillations of the signal, i.e. $\delta Y_s(t)$, which contains information about the motion of our mechanical oscillators.

As indicated in figure 3.5, the beams are combined in a beam splitter and measured by two photodiodes, whose currents are subsequently subtracted. If the condition that $|\alpha_s| << |\alpha_{LO}|$ is met, the difference between the photodiode currents $i_-(t)$ is given by

$$i_-(t) \approx 2|\alpha_s||\alpha_{LO}|\cos(\phi) + \sqrt{2}|\alpha_{LO}|\left[\delta X_s(t)\cos(\phi) + \delta Y_s(t)\sin(\phi)\right]. \tag{3.1}$$

The first term of this equation is an offset to the current which does not vary with time. Looking at the second term we find that by varying ϕ accordingly it is possible to measure any quadrature of the signal. In particular, setting $\phi = \pi/2$, the equation reduces to $i_-(t) = \sqrt{2}|\alpha_{LO}|\delta Y_s(t)$, i.e. to a signal oscillating around zero and proportional to the signal phase quadrature. Furthermore, this measurement does not depend on the signal's, but on the LO's amplitude. Thus it is often said that the LO acts as a gain factor to

the signal quadrature oscillations. More detailed discussions of the BHD can be found in multiple sources [23, 54, 55].

In practical terms, ϕ can have strong oscillations due to temperature drifts or mechanical vibrations of the setup which affect the signal and LO arms differently. This results in strong variations of the bias term of the BHD output with typical frequencies up to ~ 10 kHz. To counteract this effect, one typically places a tool on the LO arm to actively control its phase and counteract the unwanted oscillations which shift the average ϕ away from $\pi/2$. For this, one first acquires the low frequency component of the BHD output current $i_-^{\text{error}}(t) = 2|\alpha_s||\alpha_{LO}|\cos(\phi)$. Note that close to $\phi = \pi/2$, $i_-^{\text{error}}(t)$ can be approximated by a linear function, symmetric around the origin. This can thus be used as an error signal in a feedback circuit. This error signal is processed by a commercial Proportional-Integral-Differential analog circuit board (Toptica PID110) and connected to a fiber stretcher, a tool to control the phase of a signal propagating in an optical fiber, explained in detail in the next subsection, on the LO arm. With this, we are able to actively keep $\phi = \pi/2$ and, therefore, lock the BHD at the point of highest sensitivity to phase oscillations. The locking circuit compensates oscillations with frequencies up to a few kHz, whereas the mechanical modes of our devices are at hundreds of kHz. Therefore, the feedback loop should not affect the higher frequency measurements.

3.2.2. FIBER STRETCHER

A low-cost and straightforward way to shift the phase of a beam propagating through an optical fiber is to change the optical path length, for example by stretching the fiber. This can be done, for example, by tightly winding an optical fiber around a cylindrical piezoelectric tube which expands when a voltage is applied between the inner and outer sides. The stretchers we have built can be seen in figure 3.6a. The piezoelectric actuator, model SMC4037T50111 from Steminc, has a diameter of 50 mm, a capacitance of 37.5 nF, a piezoelectric constant $d_{33} = 320 \times 10^{-12}$ m/V and an unloaded resonance frequency of 32 kHz. This means that theoretically we can use this device to compensate for phase oscillations up to this frequency. The holder for the actuator and the case to enclose it were designed and 3D-printed inhouse. The 3D models are free to use and can be found online [56].

Considering the situation in which a fiber is tightly wound around the cylinder and that its length changes by exactly the same amount as the piezoelectric actuator perimeter δP, the phase change $\delta\phi$ can be calculated from $\delta\phi = N\frac{2\pi}{\lambda} n\delta P$, where λ is the wavelength, n is the refractive index of the optical fiber and N is the number of fiber loops around the cylinder. Using the fact that the piezoelectric constant $d_{33} = \delta r/V$ tells us how the radius r of the cylinder changes when a voltage V is applied, we arrive at an equation for the phase change as a function of voltage and number of loops

$$\delta\phi = N\frac{4\pi^2}{\lambda} n d_{33} V.$$

This equation can be rearranged to provide the voltage to obtain a phase change of π:

$$V_\pi = \frac{\lambda}{4\pi n d_{33} N}.$$

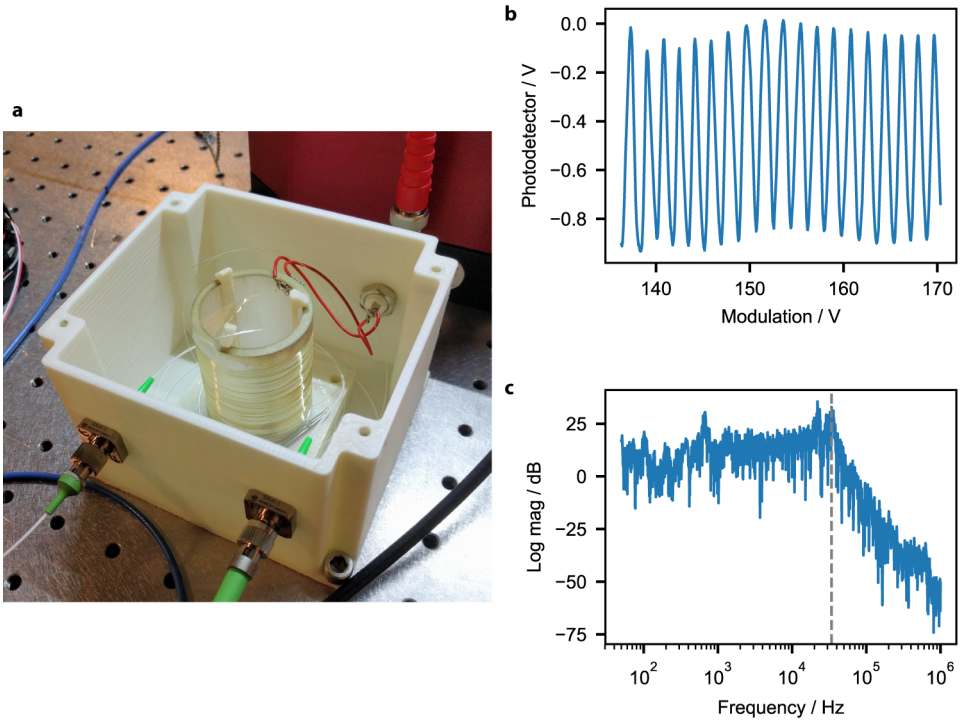

Figure 3.6: **a** Picture of a homemade fiber stretcher. **b** Output of a homodyne detector as a function of the modulation applied to a fiber stretcher in one of the interferometer arms. **c** Typical magnitude response of a fiber stretcher, together with a voltage amplifier and the low frequency output of a homodyne detector. The dashed line indicates the frequency of the first piezoelectric actuator resonance.

We usually wind the fiber between 70 and 100 times, resulting in expected V_π between 2.7 and 3.8 V. To measure the actual V_π, we place the fiber stretcher in the local oscillator arm of an unlocked homodyne detection scheme and measure the low frequency output of the BHD as a function of voltage applied to the stretcher. This is shown on figure 3.6b. Equation 3.1 tells us that the low frequency oscillations of the BHD follow the cosine of the phase difference between the two arms, which is verified in the figure. V_π is then half of the periodicity of this curve, which is 0.95 V.

The measurement shown in 3.6b was obtained by applying a ramp function to the fiber stretcher at 500 Hz. The ramp was created by a signal generator and amplified using a Falco WMA-200 low noise voltage amplifier. We also measured the magnitude of the response of the same setup as a function of frequency using a vector network analyzer, shown in 3.6c. In this setup it was not possible to optimize the SNR, which is why the measurement is so noisy. Even so, it is possible to observe the piezoelectric actuator resonance at about 34 kHz.

3.2.3. RINGDOWN SPECTROSCOPY

As mentioned before, if the BHD is locked at $\phi = \pi/2$, its output current is proportional to $Y_s(t)$, which includes information about the sample's displacement $x(t)$. Using a *spectrum analyzer*, one directly obtains the power spectral density of the current $S_{ii}(\omega)$ which is proportional to the mechanical power spectral density $S_{xx}(\omega)$ (see eq. 2.3). Therefore, from the BHD current we gain access to the frequency and linewidth of the mechanical resonances of the device under study. In this work we are concerned with features of relatively low frequency (hundreds of kHz) and linewidth (down to a few mHz). However, our spectrum analyzer (R&S FSV30) has a minimum resolution bandwidth of RBW = 1 Hz. In order to properly resolve such fine features one would have to average the signal for a long time or to acquire a long time trace and extract the mechanical properties from its Fourier transform. But these methods expose the measurement to artificial broadening mechanisms, limiting the minimum linewidth that we can measure to a value close to the spectrum analyzer's RBW.

An alternative is to measure the dynamics of the specific mode of interest, which is achieved by integrating the spectrum within a certain bandwidth around the resonance. Recall that the linewidth can be interpreted as the rate at which energy of a mode leaks to the environment. As such, the mechanical linewidth Γ_m can be obtained by resonantly driving the resonance until it reaches an excited steady-stade and measuring the time it takes for its energy to decrease by a factor of e^{-1} after the driving force is stopped. This technique is called *ringdown spectroscopy* and it is commonly applied to systems with narrow linewidths, as is the case of high finesse optical cavities.

In a ringdown measurement one typically assumes the time evolution of the system's energy follows

$$W(t) = W(t_0)e^{-\Gamma_m(t-t_0)},$$

where t_0 is the moment when the resonant driving force is stopped [22]. Notice that the energy is related to the displacement by

$$W(t) = \frac{1}{2}mx^2(t).$$

Therefore the previous equation can be rewritten as

$$x^2(t) = x^2(t_0)e^{-\Gamma_m(t-t_0)}.$$

The area under the noise spectrum of a mechanical resonance ω_m is equal to the average of $x^2(t)$ over some integration time and bandwidth BW [13, 28]

$$\langle x^2 \rangle = \int_{\omega_m - BW/2}^{\omega_m + BW/2} S_{xx}(\omega)\frac{d\omega}{2\pi}.$$

BW must be larger than the expected linewidth but small enough so that the signal-to-noise ratio is significant. If the integration time is much slower than Γ_m, the time evolution of $\langle x^2 \rangle$ can be used to obtain Γ_m.

Experimentally, we use the spectrum analyzer to measure $S_{xx}(\omega)$ and integrate it over some frequency range around the mechanical resonance of interest. Calculating the total power in a certain bandwidth is a common procedure and in some spectrum

analyzers this is called *zero-span mode*. We chose the BW to be close to 100 Hz and the measurement is repeated at a rate much faster than the mechanical decay time. The sample is driven with sinusoidal signal at the resonance frequency applied to a piezoelectric actuator which is clamped to the sample stage. During this driving phase $\langle x^2 \rangle$ increases from its thermal fluctuations level and soon reaches a steady state. Finally, the driving is turned off, the decay of $\langle x^2 \rangle$ is acquired and Γ_m is obtained from fitting this decay to an exponential function.

3.3. OPTICS CHARACTERIZATION SETUP

In order to characterize the optical properties of our samples, in particular to study the photonic crystal mirrors, we use the setup outlined in figure 3.7. With this setup we measure light transmitted and reflected from a sample. By properly calibrating the setup we gain access to the transmission and reflection spectra.

A fiber coupled Santec TSL510 wavelength-tunable laser is used as a light source. Its polarization is adjusted with a fiber polarization controller (FPC) and the beam is brought into free-space using a triplet collimator (Thorlabs TC12APC-1550). The first polarizing beam splitter (PBS) is used as a polarizer to mitigate the effect of polarization drifts in the fiber part of the setup. The second PBS splits light into the beam that is going to interact with the sample (incident beam) and a reference beam that is detected by PD_{ref}. We use the reference beam to remove the effect of power oscillations from the measured spectra that are not related to the sample. Between the two PBSs we place a half-waveplate ($\lambda/2$) to control the power ratio between the incident and reference beams. After the second PBS, the incident beam is focused onto the sample using a lens set (between 1 and 3 lenses) which are adjusted to change the waist from 8 to 420 µm. Light reflected by the sample is sent back into the second PBS. We place a quarter-waveplate ($\lambda/4$) in the incident beam path such that the reflected beam is separated from the incident beam by the PBS and then detected by PD_R. Light transmitted by the sample is recorded by PD_T. The photodetectors are home-built surface-mount-device circuits equipped with a JDSU ETX500 photodiode. By means of electronic design and spectral characterization, a linear response to the optical input power is guaranteed. An oscilloscope (Rhode & Schwarz RTB2004) records the output of all photodetectors simultaneously as the laser wavelength is scanned, allowing the acquisition of the sample's reflection and transmission spectra.

For alignment purposes, the $\lambda/4$ waveplate is adjusted to allow reflected light to propagate back to the collimator. If the incident beam is perpendicular to the sample surface, which is the alignment that is usually desired, then the reflected beam couples most efficiently back into the collimator. The back-coupled power is sent to a powermeter (PM) using a fiber circulator and the sample's tip, tilt, x, y and z positions are adjusted to maximize this power. Care is taken to ensure good tip and tilt alignment with respect to the incident beam, since the response of the PhC is very sensitive to the incidence angle.

Using flip mirrors we are also able to send the transmitted or reflected beam into an infrared CCD (Duma Optronics BeamOn-IR 1550). The camera helps during the tip and tilt alignment of the sample, or acts as a reference during the alignment of the lens system. It is also useful to assess if the sample affects the beam profile in any way.

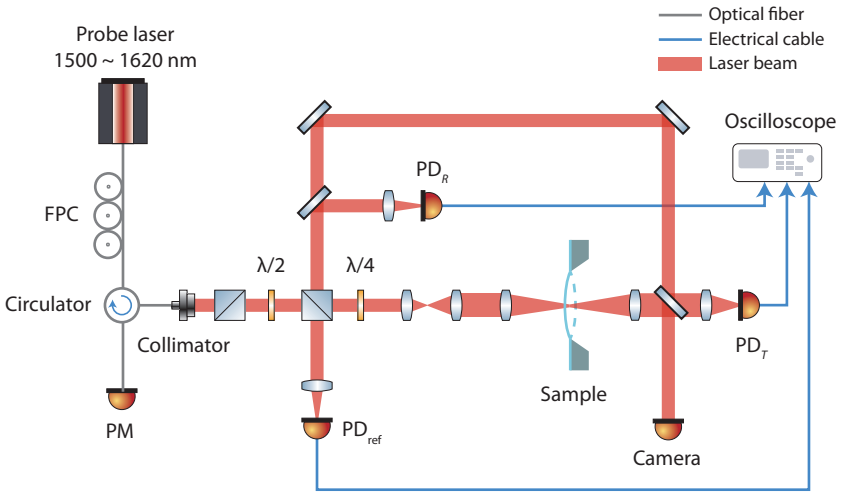

Figure 3.7: Schematic of the optics characterization setup. All beam splitters are polarizing. FPC: fiber polarization controller; PM: powermeter; PD: photodiode.

To obtain the reflection and transmission spectra, the voltages measured by the photodetectors have to be calibrated. Depending on the experiment, this calibration can be based on some assumptions that make it more or less laborious. For example, if the sample can be assumed lossless, then the calibration procedure is greatly simplified. When studying individual photonic crystal membranes, the losses are usually lower than 10^{-5} [57, 58], which cannot be resolved by this setup due to its uncertainty being on the order of 10^{-3}, as we will see below. As losses become of the same order of the measurement uncertainty, as in the case of double PhC membranes, it is important to calibrate the setup in a way that allows us to directly measure such losses. Finally, in some situations we do not have access to the transmitted light, which requires calibrating the reflected power in relation to a mirror with known reflectivity. These calibration methods are described in the following subsections.

3.3.1. CALIBRATION WITH KNOWN MIRROR

If there is no access to the transmitted beam, one can still estimate the reflection spectrum by comparing the power that the sample reflects to that which is reflected from a mirror with well known properties. This requires two measurement sets: in the first we place a mirror with known reflectivity R_{cal} in place of the sample and acquire the voltages of the reflection $V_{\text{R}}^{\text{cal}}$ and reference $V_{\text{ref}}^{\text{cal}}$ photodetectors as a function of wavelength; in the second, we replace the mirror by a sample and obtain $V_{\text{R}}^{\text{PhC}}$ and $V_{\text{ref}}^{\text{PhC}}$. The sample's reflection spectrum is then calculated as

$$R = \frac{V_{\text{R}}^{\text{PhC}} / V_{\text{ref}}^{\text{PhC}}}{V_{\text{R}}^{\text{cal}} / V_{\text{ref}}^{\text{cal}}} \times R_{\text{cal}}.$$

The reflectivity of the calibration mirror is specified to be 99.8(3) %. Considering all measurement uncertainties to be independent from each other, one can estimate the uncertainty in reflectivity ΔR via the method of uncertainty propagation

$$\Delta R = \sqrt{\sum_x (\frac{\partial R(x)}{\partial x}\Delta x)^2} \approx 0.006,$$

where $x = \{V_{\mathrm{R}}^{\mathrm{PhC}}, V_{\mathrm{ref}}^{\mathrm{PhC}}, V_{\mathrm{R}}^{\mathrm{cal}}, V_{\mathrm{ref}}^{\mathrm{cal}}, R_{\mathrm{cal}}\}$.

In the experiment described in chapter 5, to estimate the uncertainty of the beam waist, the same propagation method was applied. As uncertainty parameters, the position of each lens and its focal length was taken into account. The beam was propagated through the lens system by means of the complex beam parameter and ABCD matrices [26].

3.3.2. CALIBRATION ASSUMING NO LOSSES

If both the reflected and transmitted beam are accessible, a different calibration process can be followed. Assuming that all loss sources are negligible, then the input power $P_{\mathrm{in}} = P_{\mathrm{R}} + P_{\mathrm{T}}$, where P_{R} and P_{T} are the reflected and transmitted powers, respectively. By definition, the reflection coefficient is given by $R = \frac{P_{\mathrm{R}}}{P_{\mathrm{in}}} = \frac{P_{\mathrm{R}}}{P_{\mathrm{R}}+P_{\mathrm{T}}}$. The powers are proportional to the voltages that the photodetectors output. Assuming the photodetector responses are similar, then $R = \frac{V_{\mathrm{R}}}{V_{\mathrm{R}}+V_{\mathrm{T}}}$. Similarly, the transmission coefficient is given by $T = \frac{V_{\mathrm{T}}}{V_{\mathrm{R}}+V_{\mathrm{T}}}$.

The convenience of this method makes it a good choice when one is interested in quickly characterizing the spectrum of many samples, for example during the resonance wavelength optimization phase of the fabrication process, by sacrificing accuracy in R and T. This method was thus not used in the results which are shown in the remainder of this thesis.

3.3.3. CALIBRATION OF PHOTODETECTORS

More realistically, some of P_{in} is lost either in the optical components or by the sample itself through scattering or absorption. As such, $P_{\mathrm{in}} \neq P_{\mathrm{R}} + P_{\mathrm{T}}$. In this case we can obtain the sample's spectrum by properly calibrating all photodetectors in order to more accurately estimate P_{in}, P_{R} and P_{T}.

If no sample is present, then $P_{\mathrm{in}} = P_{\mathrm{T}}$, assuming the losses at the last two lenses to be negligible. By measuring $\epsilon = P_{\mathrm{T}}/P_{\mathrm{ref}}$ without a sample, we can later retrieve $P_{\mathrm{in}} = \epsilon P_{\mathrm{ref}}$, even if a sample is in the incident beam path. With this it is straightforward to obtain the transmission coefficient as $T = P_{\mathrm{T}}/\epsilon P_{\mathrm{ref}}$.

The reflected beam suffers some losses when it goes through the $\lambda/4$ waveplate and the PBS. These losses are not negligible and they are wavelength dependent. Therefore, to obtain a more accurate reading from $\mathrm{PD_R}$, we once again place a mirror with known reflectivity R_{cal} instead of the sample in order to measure $\gamma = P_{\mathrm{R}}/P_{\mathrm{in}}R_{\mathrm{m}} = P_{\mathrm{R}}/\epsilon P_{\mathrm{ref}}R_{\mathrm{m}}$. After, the reflection spectrum of a sample is given by $R = \frac{P_{\mathrm{R}}/\gamma}{P_{\mathrm{in}}} = \frac{P_{\mathrm{R}}}{\gamma\epsilon P_{\mathrm{ref}}}$.

Contrary to the previous subsection where we assumed that all photodetectors respond similarly, in this case we measure the responsivity κ of each device, arriving at the

following equations for the reflection and transmission spectra:

$$T = \frac{\kappa_T V_T}{\epsilon \kappa_{ref} V_{ref}}$$
$$R = \frac{\kappa_R V_R}{\gamma \epsilon \kappa_{ref} V_{ref}}.$$

An in depth explanation of this calibration procedure is given in [59].

3.4. CAVITY SETUP

As discussed in the previous chapters, our goal is to perform optomechanics experiments by placing mechanical resonators in a membrane-in-the-middle (MIM) configuration. For this we have built a setup with an optical cavity inside a vacuum chamber, which is outlined in figure 3.8. In this setup, two beams, named *probe* and *pump*, are derived from the same laser. Depending on the measurement one wishes to perform, this laser can either be a stable, fixed frequency laser (NKT Koheras Adjustik), or a highly tunable one (New Focus TLB-6730 or Santec TSL510). The probe and the cavity are kept resonant with each other using a Pound-Drever-Hall scheme (section 3.4.2), in which the feedback signal can either tune the laser frequency or change the cavity length using a piezoelectric ring. The frequency of the pump can be shifted using a single-sideband suppressed-carrier (SSB-SC, Thorlabs LN86S-FC) modulation scheme [60–62]. The cavity transmission is measured with a photodiode (PD_T), and the phase oscillations of reflected light are measured with a balanced homodyne detector (section 3.2.1).

Most of the laser is initially split into a local oscillator (LO) for the BHD. As before, the phase of this beam can be controlled with a fiber stretcher. After, it is brought into free-space using a fiber collimator and its polarization is adjusted so it is fully transmitted through a polarizing beam-splitter (PBS) which later combines the LO with the signal beam. The two beams are then split equally into two photodiodes, whose difference current provides the BHD signal that is used for spectral measurements and for locking the phase of the signal and LO paths.

The remaining laser light is split into the probe and pump beams. The probe is phase modulated with an electro-optical modulator (EOM, Ixblue Photline MPX-LN-0.1) to generate sidebands for PDH locking. It is brought into free space and focused through a Faraday isolator which will later send light reflected from the cavity into a detector for PDH (PD_{PDH}) and BHD (PD_{BHD}). After, it goes through a PBS that combines the probe and pump into the same propagation path. The profile of the beam is matched to one of the fundamental transversal modes of the optical cavity using three lenses placed in between the cavity and two steering mirrors which are used to align the beam with the cavity axis. These beams are then aligned to the optical cavity by repeatedly scanning the laser frequency over a span large enough to include a few cavity free spectral ranges and optimizing the ratio between light coupled to the fundamental transversal modes and higher order ones. With proper alignment and mode-matching, we are able to reach ratios as high as 96 %. The pump beam follows a path with similar optical components and propagation length to that of the probe, which makes it possible to have similar coupling efficiencies to the fundamental cavity mode for both probe and pump.

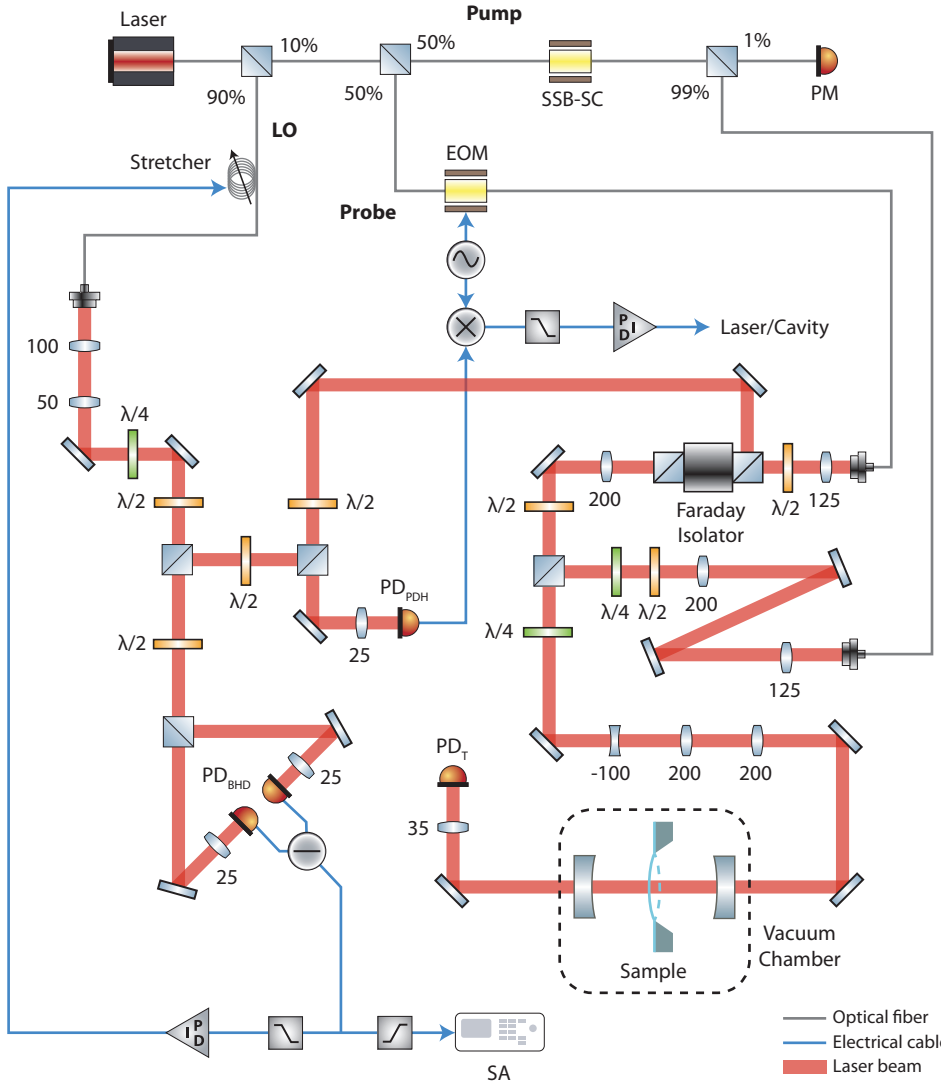

Figure 3.8: Schematic of the cavity setup. All beam splitters are polarizing. LO: local oscillator; PM: power-meter; PD: photodiode; PDH: Pound-Drever-Hall; EOM: electro-optic modulator; SSB-SC: single sideband, suppressed carrier modulator; SA: spectrum analyzer; PID: proportional, integral, derivative controller.

Similarly to the mechanics setup, the cavity and the membrane sit inside a vacuum chamber to minimize viscous damping. The chamber is pre-pumped with a turbomolecular and Roots pump set down to 5×10^{-7} hPa. Below this pressure, the vacuum is kept with an ion pump, which after a few days of pumping can bring the pressure down to 1×10^{-8} hPa.

The following subsections describe in more detail the cavity design and properties. The Pound-Drever-Hall modulation technique is also introduced. Even though it was implemented in the setup, it is not required to understand the experiments described in the following chapters.

3.4.1. CAVITY DESIGN

In designing an optical cavity one must specify the spatial mode profiles as well as the cavity finesse [26, 63]. The mode profiles are set by the spacing between the end mirrors as well as their radii of curvature. The finesse is given by the total cavity losses, which for an empty cavity are the transmission from and scattering at the mirrors.

To study the membrane in the middle of the cavity, we chose to use mirrors with the same radii of curvature. In order to obtain small waists between 25 and 50 µm, which are fractions of the membrane widths that we are able to fabricate (100 to 300 µm), the cavity assumes a nearly concentric, or spherical, geometry, in which both radii of curvature are approximately equal to half the cavity length. Short cavities result in high optomechanical coupling rates. However, they also increase the cavity linewidth and, as such, the sideband resolution ratio ω_m/κ. We chose a cavity length L of approximately 50 mm, which gives enough room to build the membrane translation system around it; results in a free spectral range FSR = 3 GHz, which is easily accessible with the frequency fine tuning controls of our lasers and with the modulators and electronics at our disposal; and gives us the chance of reaching sideband resolution with commercially available mirrors. This length sets the radii of curvature to 25 mm. Notice that in this concentric geometry, the stability parameter of both mirrors is -1, which is on the edge of the stability criterion (see section 2.2). Therefore, we slightly decrease the cavity length to 47.9 mm (FSR = 3.13 GHz), corresponding to a beam waist of 49 µm (eq. 2.13). Having defined the fundamental cavity mode profile, we use a beam propagation software to calculate the focal length and position of the three lenses that match the shapes of the beam right after the PBS which combines probe and pump, and that of the cavity.

The cavity finesse F, in combination with its FSR, defines the optical linewidth $\kappa = \mathrm{FSR}/F$. A small linewidth is usually desirable, since it makes reaching the sideband resolved regime easier. However, it also makes the cavity more sensitive to length fluctuations, which can complicate the laser locking procedure. We therefore opted to use reflectivities for the front and back mirrors of, respectively, 99.9 % and 99.995 %. This results in a theoretical finesse and linewidth of 6000 and 240 kHz.

Figure 3.9a shows the cavity spectrum in transmission where the resonances are indicated with a red dot on top. The high transmission features correspond to longitudinal modes with similar transversal mode indices. In this case, we have aligned the cavity such that these modes correspond to the fundamental transversal modes. The smaller peaks are higher order modes to which a small part of the incident beam couples to. Panel b of the same figure shows a zoom-in of the fundamental cavity mode. For this

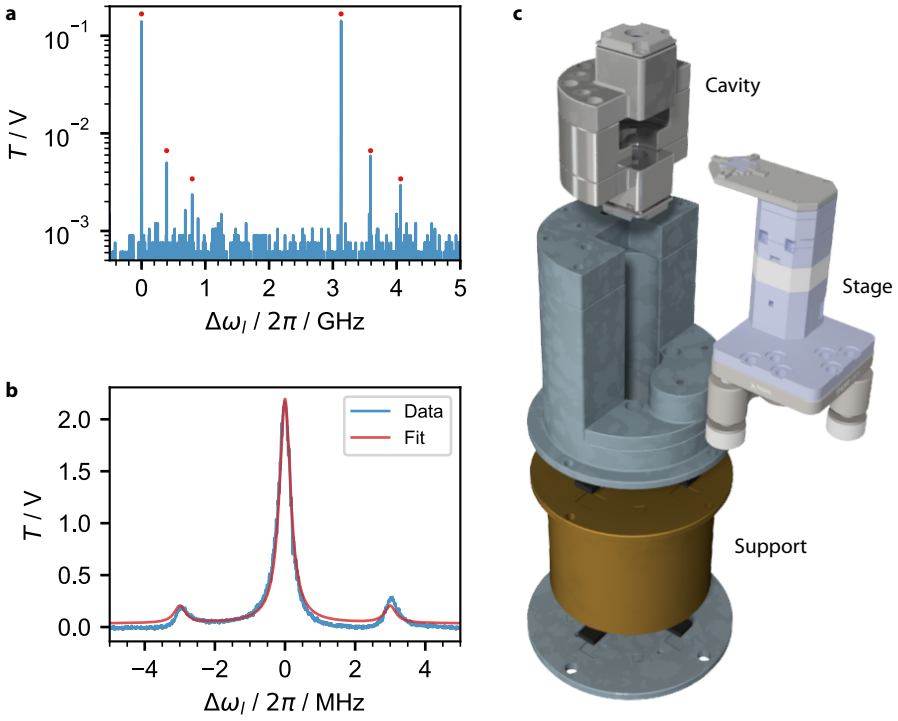

Figure 3.9: **a** Spectrum of the cavity transmission. The cavity modes are indicated by the red dots. The two highest peaks correspond to consecutive longitudinal modes with similar (fundamental) transversal mode indices, spaced by the cavity FSR = 3.13 GHz. The smaller peaks are higher order transversal modes. **b** Fine scan over one of the fundamental modes. The two sidebands are generated by an EOM modulated with a 3 MHz sinusoidal voltage. A fit of the data gives a finesse of 8000 and a linewidth of 192 kHz. **c** Exploded view of the cavity and the membrane stage assembly.

scan, the probe was weakly modulated using the EOM with a 3 MHz sinusoidal voltage. The modulation creates sidebands at higher and lower frequencies of the carrier and since the modulation is weak, we only need to consider the first order sidebands. These will couple to the optical cavity and they are seen in the spectrum as the two peaks at the left and right of the main resonance. The distance of the sidebands from the carrier is well defined by the sinusoidal voltage modulation and can therefore be used to accurately calibrate the timescale of the oscilloscope into a frequency scale, allowing us to directly measure the cavity linewidth. In this particular case we have obtained a finesse and linewidth of 8000 and 192 kHz, slightly better than predicted theoretically. However, shortly after the cavity mirrors may have gotten dirty, increasing their scattering, changing these values to 2900 and 526 kHz.

The cavity assembly, as well as the membrane stage and the support structure that connects both to the vacuum chamber is shown in an exploded view on figure 3.9c. The cavity is composed of the grey structure on the figure top. The mirrors are mounted inside the cubic structures, with a steel spacer in between. The bottom mirror holder

includes a ring piezo which we can use to fine tune the cavity length by approximately 2.5 µm. On the figure bottom one can see a plate that connects to the vacuum chamber. In between the support plate and the cavity there are two elevation stages which are separated by rubber pads made of viton. These are included as a means to reduce the coupling of mechanical vibrations from outside the chamber to the cavity. Finally, the chip translation stage is shown on the right. It consists of a stack of stick-slip piezoelectric stages (Attocube ANPx/z101) with a cantilever on top, where the chip is mounted. The stick-slip assembly can move the membrane in x, y and z by 5 mm. This gives us great flexibility to align and study multiple devices in a single pump down. In addition, the z element can be fine tuned over a range of 5 µm. For tip and tilt control, the stages are mounted on top of a kinematic plate (Thorlabs POLARIS-K1M4/M).

Although this setup was useful to perform the static measurements presented in chapter 6, it could not be used for other typical cavity optomechanics measurements due to difficulties in locking the frequencies of the laser and the cavity. Even though it was possible to lock the cavity and the laser when the cavity was empty, the same was not true with a membrane in its middle. After many tests and modifications of the detection and feedback electronics, we concluded that the problem lies in low frequency mechanical vibrations from the device positioning stage which couple dispersively to the cavity frequency through the optomechanical interaction and which are amplified by the feedback loop, making the system unstable. In particular, the cantilever-shaped membrane holder has its first mechanical resonance frequency oscillating along the cavity axis at approximately 700 Hz. Interestingly, it was possible to lock the system if the optomechanical coupling was quadratic. In this regime, the cavity frequency depends on the total energy of the mechanical resonances and not on the displacement itself. Since the total energy changes much slower than the displacement, the effect of these low frequency resonances became less pronounced, making it easier to lock the cavity and the laser. Presently we are finishing building a revised cavity assembly in which several key changes were made with the goal of increasing the system's stability:

- The tip and tilt stage was modified to one which is more compact and can be coupled to the rest of the setup in a more rigid and symmetric way;
- The x and y stages are now based on stiffer, more compact and ball-bearing based manual translation stages; the z stage was removed, to make the system more compact;
- The device holder was thickened, elongated and it is now partially clamped on the opposite side of the cavity (still allowing freedom for x and y translation), pushing its first relevant resonance frequency to above 7000 Hz.

More details about the new cavity design can be found in [64].

3.4.2. POUND-DREVER-HALL MODULATION

In experiments involving optical cavities one is often interested in having the laser frequency ω_l to be the same or at a known offset from the cavity resonance frequency ω_c. However, both the laser and the cavity suffer from frequency noise (e.g. due to length oscillations, thermo-optical drifts of the laser gain medium, etc.) which can have a large

amplitude, making it impossible to passively make the two resonant. To counteract these effects, one typically generates an error signal that carries information about the difference in frequency between the laser and the cavity, and actively tunes either the laser or the cavity frequency to compensate for those differences.

The error signal must indicate in which direction the frequency of one of the elements needs to be changed in order to achieve resonance. Simply measuring the reflection or transmission of a probe incident to the cavity cannot generate a valuable error signal, if the frequency oscillations are of the order or larger than the cavity linewidth, since the intensity spectrum of the cavity is symmetric around the resonance and, therefore, does not provide information about the direction in which the frequency needs to be corrected. However, the phase spectrum of a beam reflected from the cavity is asymmetric around the resonance and can therefore indicate the direction of the frequency correction.

As mentioned in section 3.2, one usually must interfere a beam with a known reference in order to measure an optical phase. In our experiment we use the Pound-Drever-Hall technique to lock the cavity to the lasers [65, 66]. In this technique, the probe is weakly modulated with an EOM with a frequency ω_{PDH}, generating two sidebands at frequencies $\omega_l + \omega_{\mathrm{PDH}}$ and $\omega_l - \omega_{\mathrm{PDH}}$. ω_{PDH} is chosen to be $2\pi \times 17.3\,\mathrm{MHz}$, much larger than the cavity linewidth κ, such that the sidebands do not couple into the cavity when the probe is close to resonance. If the probe is approximately resonant with the cavity, the phase of the upper and lower sidebands will be constantly shifted by $\pm\pi/2$, respectively, and they can therefore be used as phase references. On the other hand, the probe phase shift will strongly depend on how far it is from the cavity resonance. The interference between the probe and the sidebands therefore generates an error signal which indicates the magnitude and direction of the frequency difference between the cavity and the laser.

As shown in figure 3.8, we use signal generator to modulate the probe EOM. The signal reflected from the cavity is measured by PD PDH and mixed with the same frequency that modulates the EOM. The low frequency mixing component has the phase information we desire for the error signal. The signal is therefore lowpass-filtered, fed to a proportional, integral, derivative (PID) controller and sent to the piezo that controls the cavity length, after being amplified. The feedback can alternatively be applied to the laser frequency fine tuning modulator.

This type of locking technique is well described in the literature. For more details, the reader can, for example, look into the very instructive article from Eric Black [66].

4

HIGH-Q_m SiN MECHANICAL RESONATORS

All quantum optomechanics experiments to date operate at cryogenic temperatures, imposing severe technical challenges and fundamental constraints. Here we present a novel design of on-chip mechanical resonators which exhibit fundamental modes with frequencies f_m and mechanical quality factors Q_m sufficient to enter the optomechanical quantum regime at room temperature. We overcome previous limitations by designing ultrathin, high-stress silicon nitride membranes, with tensile stress in the resonators' clamps close to the ultimate yield strength of the material. By patterning a photonic crystal on the SiN membranes, we observe reflectivities greater than 99 %. These on-chip resonators have remarkably low mechanical dissipation, with $Q_m \sim 10^8$, while at the same time exhibiting large reflectivities. This makes them a unique platform for experiments towards the observation of massive quantum behavior at room temperature.

This chapter has been published together with R. A. Norte and S. Gröblacher in Physical Review Letters **116** (14), 147202 (2016) [67]

4.1. INTRODUCTION

OPTOMECHANICAL systems, where light is coupled to mechanical motion via the radiation pressure force, have generated enormous interest over the past years as they are promising candidates for testing macroscopic quantum physics, have great potential as quantum transducers between distinct quantum systems, as well as for their capabilities in sensor applications [13]. State-of-the-art systems have recently demonstrated ground-state cooling [19, 68], mechanical quantum state preparation [16, 69], entanglement [70] and squeezing of both the optical [71, 72], as well as the mechanical mode [73–75]. Experiments involving such optomechanical systems in the quantum regime are technically very challenging and so far have exclusively operated at cryogenic temperatures. This poses serious restrictions on the type of experiments that are feasible. Without the need for cryogenic pre-cooling, one could envision their use as hybrid quantum systems with for example atomic gases [76] or single atoms [77]. It would also open up practical avenues for real world applications of such quantum optomechanical systems.

One of the most successful implementation of mechanical oscillators for such (quantum) optomechanics experiments are devices made of high-stress silicon nitride (Si_3N_4), which have been utilized in quantum-limited accelerometers [78], coupling of their motion to ultra-cold atoms [33, 79], optomechanics in 3D microwave cavities [80], quadratic coupling in cavity optomechanics [14] and conversion between microwave and optical signals [81].

However, even these low mechanical dissipation oscillators have to date not operated in a regime where realistic quantum experiments at room temperature are feasible. The benchmark for this elusive regime is the $f_m \times Q_m$ product of the resonator which requires the mechanical quality factor Q_m to be larger than the number of thermal phonons at room temperature ($f_m \times Q_m > k_B T_{room}/h$), with h being the Planck and k_B the Boltzmann constant [82]. This regime will allow for ground-state cooling using the radiation pressure force and hence allow for experiments operating in the quantum domain. In general, the quality factor-frequency product also determines the number of coherent oscillations the resonator can undergo before one thermal phonon enters the system, i.e. $N_{osc} = Q_m f_m \cdot h/2\pi \cdot k_B T$. Experimental realizations of on-chip mechanical resonators that exceed this requirement have all been demonstrated in higher-order mechanical modes [83, 84]. Such mechanical systems are however in practice not useful for cooling experiments as higher order modes are enveloped by numerous neighboring modes, which increase the displacement background noise as one cools the mode of interest. To avoid this limit, it is important to couple to the fundamental mode of the membrane. An additional challenge is to operate at mechanical frequencies beyond 10^5 Hz, where commercial lasers exhibit a minimal amount of classical noise and can relatively easily be quantum limited to shot-noise in order to avoid heating or decoherence through noise [85]. Another difficulty for realistic quantum optomechanics experiments at room temperature is that often good mechanical quality is mutually exclusive with good optical reflectivity [86–88]. This limits the achievable coupling rates and increases the necessary optical power to a level where absorption becomes a practical limitation for cooling and quantum experiments.

In this letter, we demonstrate the first optomechanical platform that overcomes all

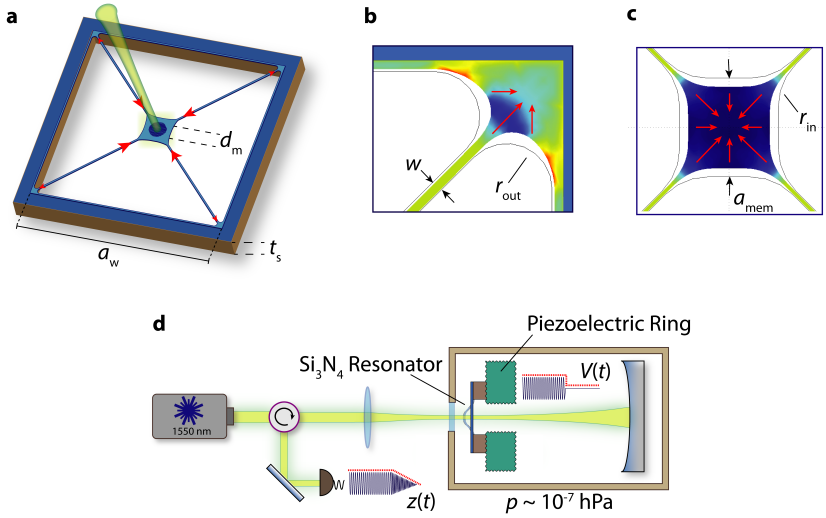

Figure 4.1: **a** Schematic of our tethered membrane which consists of a central membrane connected to the silicon substrate through a series of thin tethers. The central photonic crystal reflector can be used for increased reflectivities. Shown are our design parameters which are individually swept keeping all other parameters constant to observe their effect on the $f_m \times Q_m$ product. Finite element simulations map out the strain throughout the resonator and calculate deformation due to the relaxation of the material at the **b** tether clamps and **c** central membrane, which together significantly enhance the tensile stress in the tethers. **d** Schematic of ringdown measurement setup. The membrane is resonantly driven by a piezoelectric transducer inside an optical interferometer. We determine the mechanical dissipation by observing the ringdown of the mechanical resonance (see text for details).

these limitations, paving the way for room temperature experiments in the quantum regime. We fabricate on-chip optomechanical mirrors which exhibit $f_m \times Q_m$ products of their fundamental mechanical modes above the requirement for ground state cooling without cryogenics (figure 4.1). With a center-of-mass frequency of ~ 150 kHz and mechanical quality factor $Q_m \sim 10^8$, this new-generation of Si_3N_4 tethered membranes is on par with the state-of-the-art in optically levitated nanospheres, known for their extreme mechanical isolation and ultra-low dissipation, which are only limited by gas-molecule collisions in high vacuum and photon recoil-heating [89, 90].

In order to achieve such remarkably low dissipation rates of $\Gamma_m/2\pi = 1.4$ mHz with a tethered system, we design ultra-thin high-stress Si_3N_4 membranes which enhance the intrinsic stress in crucial tether regions – significantly reducing clamping and bending losses [91]. A key observation is that high-stress membranes have mechanical frequencies which are stress-dominated, meaning that one can minimize the thickness of the resonator in order to reduce bending losses without significantly reducing the mechanical mode frequencies. We fabricate tethered membranes with ultra-low dissipation rates by engineering up to 6 GPa of stress within films as thin as 15 nm and intrinsic stress of 1.3 GPa. Using finite element simulations to calculate the stress throughout the resonators, we push the tensile stress in the resonator's clamps to values near the ultimate yield strength of low-pressure chemical vapor deposition (LPCVD) Si_3N_4. In addition, we

are able to show that we can increase the intrinsic optical reflectivity R of these membranes to up to 99.3 % by patterning a two-dimensional photonic crystal onto the structure. These structures enable coupling rates that allow ground-state cooling from room temperature with realistic parameters in a membrane-in-the-middle design [37, 92–94] and can also be used as an end-mirror of a Fabry-Perot cavity [87, 95–97].

4.2. DEVICE DESIGN

The central mirror on the tethered membranes is a 2-D photonic crystal device (see figure 4.2a), that is designed using finite difference time domain (FDTD) simulations. They are similar to previous designs of grating reflectors [57] and photonic crystals [98, 99], which usually consist of an array of either lines or holes etched into the dielectric, respectively. Such a periodic change in the refractive index allows for a bandgap to be tailored for a specific wavelength, resulting in (simulated) reflectivities > 99.9 %. Experiments to date employing such photonic crystal mirrors for optomechanical resonators have however suffered from a trade-off between high reflectivity and high-mechanical quality, due to the requirement of thick dielectrics in order to achieve large R [99]. We confirm this by measuring PhC mirrors consisting of a square lattice of holes as a function of silicon nitride thickness (see section 4.6.3). In order to circumvent this design issue we follow two slightly different approaches: we either leave a thick cylindrical slab of SiN around the PhC (see figure 4.2b) or instead of using holes we use pillars, resulting in an inverse photonic crystal (see figure 4.2c). While the latter design still suffers from fabrication imperfections resulting in reflectivities of ~ 95 %, the other new design allows us to reach $R > 99$ % (figure 4.2d). We show that both methods decouple the mechanical from the optical properties and allow for optomechanical devices with simultaneous high-Q_m and high-R.

We also study the tethered membranes' mechanical parameters, several of which suffer from the conventional trade-off between either good mechanical quality factor or high frequency (see figure 4.5 and table 4.4, Supplementary Information). For example, extending the length of the tethers by increasing the size of the window a_w in order to reduce clamping and bending losses not only results in higher mechanical quality factors but also lower frequencies [100]. Achieving ultra-high Q_m with this parameter will result in very low fundamental modes, where low-frequency classical noise in lasers becomes a compelling limitation on radiation-pressure sideband cooling (for more detail and discussion on design parameters see the Supplementary Information).

4.3. LOSS MECHANISMS

It is known that for fundamental modes of long, thin nanostrings (width $w \approx 3 \sim 5\ \mu$m), mechanical dissipation starts to be dominated by bending losses [101]. By accounting for the dominating effect of flexural bending near the clamps of tensile strings one can express the quality factor for the fundamental mode of doubly clamped strings as [102, 103]

$$Q_{str} = \left[\frac{\pi^2}{12} \frac{E}{\sigma} \left(\frac{t_f}{L} \right)^2 + \sqrt{\frac{E}{3\sigma}} \left(\frac{t_f}{L} \right) \right]^{-1} Q_{bending} \tag{4.1}$$

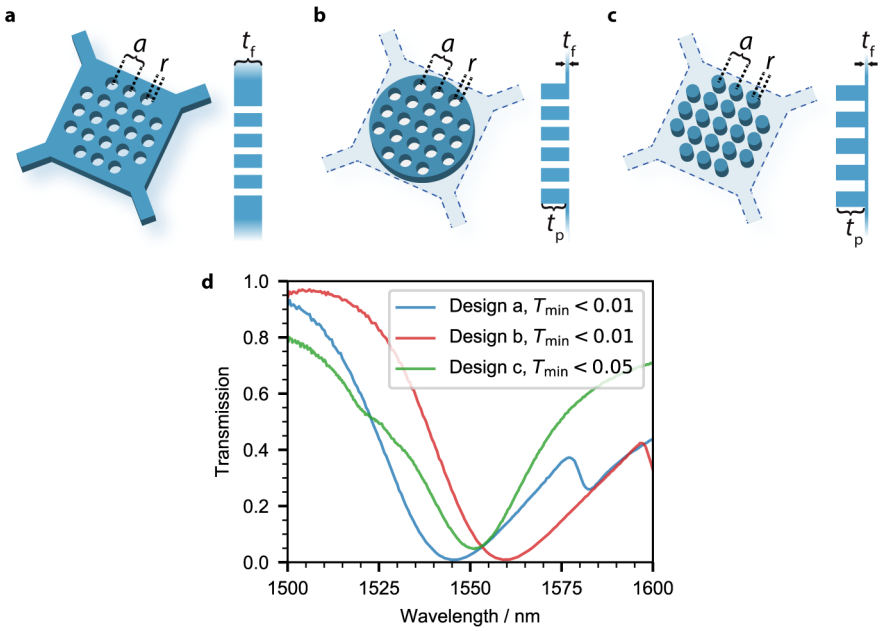

Figure 4.2: **a** Conventional design of a PhC membrane. The maximum reflectivity ($1 - T_{\mathrm{min}}$) strongly depends on the thickness of the silicon nitride (see SI). For **a** this is in competition with the requirement of thin films (i.e. small t_{f}) for good mechanical quality (cf. figure 4.4). We overcome this limitation by either leaving a thick cylindrical slab in the center of the membrane **b** or by using an inverse photonic crystal design **c**. These designs decouple the mechanical and optical properties of the membrane and show similar optical performances to **a**. **d** Transmittance T of three different designs of tethered mechanical membranes. We experimentally confirm the minimum transmission measurements by using a PhC membrane as one end-mirror of a Fabry-Perot cavity in combination with a second mirror with known reflectivity and measuring the finesse. The thickness of the photonic crystal t_{PhC} was chosen to be 200 nm for all designs.

where E is the Si_3N_4 Young's modulus, σ is the stress in the string, t_{f} is the film thickness, L is the length of the nanostring, and Q_{bending} is the quality factor due to bending losses in a relaxed string, which is mostly dependent on intrinsic material damping. From eq. 4.1, one finds that the quality factor of a string can be enhanced by using thinner strings with decreasing t_{f}. A crucial observation from thin plate theory is that membranes under large tensile forces have stress-dominated mechanical frequencies (i.e. $f_{11} = 1/(\sqrt{2}L)\sqrt{\sigma/\rho}$, where ρ is the material's density) which are independent of membrane thickness. Since our devices' dissipation is dominated by bending losses through the tethers and their mechanical modes are weakly dependent on thickness, we can engineer thinner membranes with increased mechanical quality factors and negligible impact on the frequency. This design scheme overcomes the trade-off between Q_{m} and f_{m} in order to realize optomechanical resonators with unprecedented enhancement of the fundamental mode $f_{\mathrm{m}} \times Q_{\mathrm{m}}$ product.

In addition, substrate thickness also plays an important role in anchoring losses for out-of-plane fundamental modes, where larger vibrational displacements of thin-

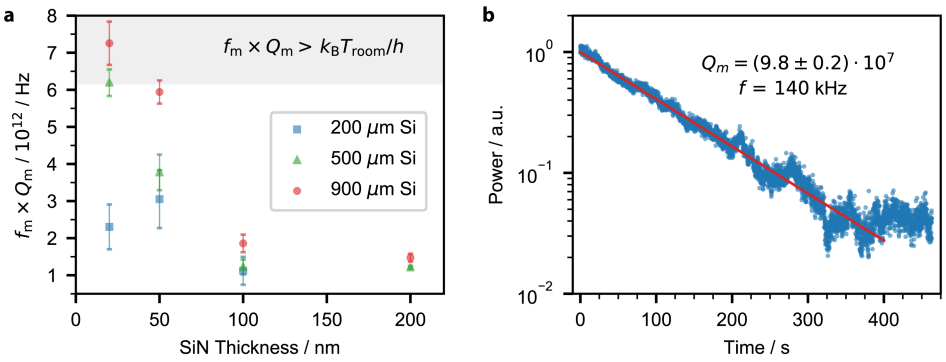

Figure 4.3: **a** Shown is the $f_m \times Q_m$ product for the nominal design (see text) of our tethered membrane for various silicon substrate ({200, 500, 900} μm) and Si_3N_4 film ({20, 50, 100, 200} nm) thicknesses. Each point is the average of measurements on resonators with identical geometry. In addition we verified that the results are independent of the particular PhC design. For thin silicon substrates (t_s = 200 μm), the anchoring losses completely dominate and result in minimal enhancement of the mechanical quality factor even at t_f = 20 nm. However, these ultra-thin films exhibit $f_m \times Q_m$ products above the ground state cooling limit (shaded region) when fabricated on thicker substrates, where anchoring losses are less pronounced. **b** Ringdown measurement for the best observed value for a single device with $Q_m = 9.8(2) \times 10^7$ at f_m = 140 kHz for a 20 nm thick film, with otherwise nominal parameters.

ner substrates near the clamping points of a fundamental mode significantly increase mechanical dissipation [104]. Previous studies found some enhancement in 30 ~ 50 nm-thick square membranes when moving from 200 µm substrates to 500 µm with a negligible effect in thicker Si_3N_4 films ($t_f \geq 100$) [22]. Silicon substrate thickness and silicon nitride film thickness are the parameters we focus on to achieve significant enhancements in $f_m \times Q_m$. We investigate these effects by fabricating our resonators from ultra-thin films ≤ 15 nm and on substrates as thick as 900 µm.

4.4. RESULTS

We determine the mechanical quality factors of our membranes by performing ringdown measurements using a piezoelectric stack in an optical interferometer (see figure 4.1d). Due to viscous damping, which becomes increasingly dominant with thinner membranes, our measurements are conducted inside an ultra-high vacuum chamber at ~ 10^{-7} hPa. Positioning stages are used to align the chip with the membranes to a 20 μm spot of a 1550 nm laser. The chip is placed onto the piezoelectric stack under its own weight since any type of clamping or gluing of the chip to the experimental setup can reduce the mechanical quality factor by several orders of magnitude [22]. Each of our chips has 9-16 resonators which allow us to collect several data points for each parameter sweep. We start with a nominal resonator design (see Supplementary Information for details) and adjust each parameter keeping others fixed.

In figure 4.3a we plot the effects on $f_m \times Q_m$ by varying the thickness of the silicon nitride films and silicon substrates for the nominal membrane design. We find that losses in thicker Si_3N_4 resonators ($t_f \geq 100$ nm) are dominated by bending losses. From the

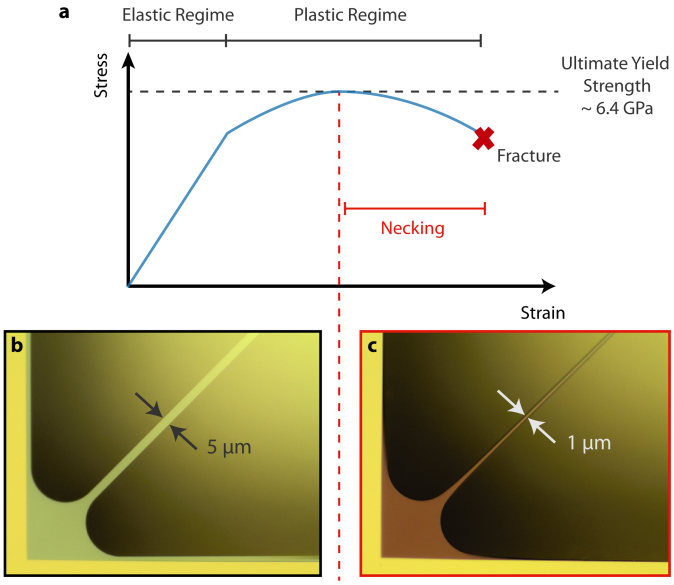

Figure 4.4: **a** Sketch of the stress-strain curve for silicon nitride. We design our structures such that for the thinnest films we operate in the regime close to the ultimate yield strength of the material. **b** Microscope image showing a nominal clamp with outer fillet $r_{out} = 20\,\mu m$ and tether width $w = 5\,\mu m$ when properly fabricated with turbulence reducing holders. **c** Typical necking deformation in very thin films ($\leq 20\,nm$). This occurs at the tether clamps where the stress is the largest and when the resonators are being exposed to small viscous forces or temperature gradients during fabrication. The tether is deformed to a width of $\sim 1\,\mu m$.

data we also see that low dissipation in ultra-thin resonators can be completely dominated by anchoring losses in thin substrates ($\sim 200\,\mu m$). A clear enhancement in the $f_m \times Q_m$ product is observed, exceeding the above requirement for ground state cooling at room temperatures as one fabricates thinner tethered membranes on increasingly thicker substrates, where their anchoring losses are no longer a limiting factor on Q_m.

In order to push the devices to their material limits, we engineer the stress at the clamps (the dominant source of flexural bending loss) to just short of the Si_3N_4 ultimate yield strength ($\approx 6.4\,GPa$ [105]). At thicknesses $\leq 15\,nm$, the silicon nitride membranes become increasingly susceptible to plastic deformation when subjected to small viscous forces due to handling or large temperature variations during wet chemical processing. Figure 4.4c shows the necking that occurs when the resonator is subjected to these small forces which result in large frequency drops from $\sim 170\,kHz$ to $\sim 60\,kHz$ and reduction in Q_m to $\sim 10^5$. Necking is a form of irreversible plastic deformation that occurs when excessively large strains localize in small cross-sections. In order to minimize such effects, we use polytetrafluoroethylene (PTFE) turbulence shielding holders [106, 107] which gently dilute the resonators from one liquid to the next during fabrication. This significantly reduces the resonators' exposure to viscous forces and surface-tension in the wet chemistry processes required to release, clean and rinse the sample thoroughly [107]. At thicknesses below 20 nm we observe consistently reduced $Q_m \sim 10^7$. Ultra-thin films be-

low 20 nm produce delicate structures which make it difficult to attribute the lower quality factors to intrinsic limits of the sensitive handling during fabrication or whether other surface-dominant loss mechanisms such as Akhiezer damping become more dominant loss channels. Figure 4.3b shows a ringdown for our best device at 20 nm silicon nitride thickness, 900 µm wafer thickness and mechanical quality factor $Q_m = 9.8(2) \times 10^7$ at a fundamental mode frequency of 140 kHz ($f_m \times Q_m = 1.37 \times 10^{13}$ Hz).

With the demonstrated combination of large reflectivities and low mechanical dissipation, we will be able to access the optomechanical quantum regime from room temperature. A first demonstration of such quantum behavior could be achieved by cooling the mechanical mode into its quantum ground state, which is already realistic with these device parameters (see Supplementary Information for detailed calculations).

4.5. CONCLUSION

To conclude, we studied the dissipation mechanism in a new regime of ultra-thin, highly-stressed optomechanical resonators and their effects on mechanical quality factor and fundamental mode frequency. By moving to these thin devices on thick silicon substrates and by engineering the stress in their tethers to near the ultimate yield strength of Si_3N_4 we are able to overcome a well-known trade-off between frequency and mechanical quality factor to achieve fundamental mode $f_m \times Q_m$ which are more than twice the requirement for quantum ground state cooling from room temperature. Our on-chip device performances are on par with the best values measured for optically levitated nanospheres without the need for high power trapping lasers or complex experimental setups. We also demonstrate the possibility to combine our resonators with different photonic crystal mirror designs which result in reflectivities between 95 % and 99 %, while simultaneously achieving ultra-high Q_m. These results allow to finally realize experiments to laser-cool a mechanical oscillator from room temperature to its quantum ground state (see SI). Such reflective tethered membranes are also ideal for optical trapping configurations that enhance the frequency and the mechanical quality factor even further, while avoiding thermal bistabilities which become a severe limitation at high laser powers [108, 109]. With a $Q_m \sim 10^8$, our dissipation rates are only matched in other silicon nitride membranes with the use of cryogenic cooling near 14 mK, with an improvement of two orders of magnitude in mechanical quality factor from room temperature [110]. This allows one to speculate that coupling our new generation of resonators to such low temperature baths could allow for $Q_m \sim 10^9$.

Our devices have the potential to allow for fundamental tests of quantum physics by generating massive, non-classical states of a mechanical oscillator, for example in space, where complicated cryogenic setups are not feasible [111]. In addition, thanks to the ultra-low mechanical dissipation, it is possible to push boundaries of applications in ultra-sensitive (e.g. force) detection, as has recently been demonstrated [112]. For the devices used here, we calculate a force sensitivity of about 10 aN/Hz$^{1/2}$, which, together with reference [112] and to our best knowledge, is the highest to date at room temperature. Achieving this level of dissipation in an on-chip design heralds a realistic building block towards optically-linked silicon-based quantum networks [113] operating at room temperature.

ACKNOWLEDGMENTS

We would like to thank M. Aspelmeyer, L. Bavdaz, A. G. Krause, I. Marinković, and G. A. Steele for fruitful discussions and help with early measurements. We also acknowledge valuable support from the Kavli Nanolab Delft, in particular from C. de Boer and M. Zuiddam.

4.6. SUPPLEMENTARY INFORMATION

4.6.1. COOLING TO LOW PHONON OCCUPANCIES

Cooling to the motional ground state of a mechanical oscillator with frequency ω_m and linewidth Γ_m (FWHM) using an optical cavity with frequency ω_c and amplitude decay rate κ in practice means reducing the average thermal occupation to $\bar{n}_f < 1$. In order to resolve the mechanical noise spectrum this also means that the effective mechanical quality factor $Q_{eff} > 1$. Q_{eff} is the optomechanically broadened quality factor and is different from the intrinsic quality factor $Q_m = \omega_m/\Gamma_m$. To experimentally achieve such cooling performances, we significantly increase the optomechanical coupling from bare Si_3N_4 resonators by adding photonic crystals, which allow us to reach reflectivities between 95 % and 99 % (see main text). In the following analysis, we calculate the phonon occupancies and the corresponding effective quality factors that are achievable by optomechanically cooling the mechanical resonators presented in this letter.

4

EFFECTIVE MECHANICAL FREQUENCY AND DAMPING RATES

The optomechanical coupling changes the mechanical properties of the resonator, giving rise to an effective frequency $\omega_{eff}^2(\omega) = \omega_m^2 + 2\omega\omega_{OM}(\omega)$ and damping rate $\Gamma_{eff}(\omega) = \Gamma_m + \Gamma_{OM}(\omega)$. $\omega_{OM}(\omega)$ and $\Gamma_{OM}(\omega)$ are the shifted frequency and damping rate due to the optomechanical interaction, derived from the modified mechanical susceptibility in frequency space ω, which are given by [13]

$$\omega_{OM}(\omega) = g^2 \frac{\omega_m}{\omega}\left(\frac{\Delta+\omega}{(\Delta+\omega)^2+\kappa^2} + \frac{\Delta-\omega}{(\Delta-\omega)^2+\kappa^2}\right),$$

$$\Gamma_{OM}(\omega) = g^2 \frac{\omega_m}{\omega}\left(\frac{\kappa}{(\Delta+\omega)^2+\kappa^2} - \frac{\kappa}{(\Delta-\omega)^2+\kappa^2}\right),$$

where ω_l is the laser frequency, $\Delta = \omega_l - \omega_c$ the detuning with respect to the cavity, $g = g_0\sqrt{\bar{n}_c}$ the linearized optomechanical coupling strength, $\bar{n}_c = \frac{2P}{\hbar\omega_l}\frac{\kappa_1}{\kappa^2+\Delta^2}$ the average cavity photon number, P the laser power, κ_1 the amplitude decay rate of the input mirror, $\hbar$ the reduced Planck constant, $g_0 = -\frac{\partial\omega_c}{\partial x}x_{zpf}$ the single-photon optomechanical coupling, $x_{zpf} = \sqrt{\frac{\hbar}{2m_{eff}\omega_m}}$ the zero-point fluctuation of the mechanical mode, and m_{eff} the effective mass of the mechanical mode. Note that these effects are most pronounced for $\omega = \omega_m$.

FINAL AVERAGE PHONON OCCUPANCY

Using the previous equations one can calculate the effective mechanical quality factor $Q_{eff} = \frac{\omega_{eff}}{\Gamma_{eff}}$ and the oscillator's final average phonon occupancy, which in general is given by

$$\bar{n}_f = \frac{\Gamma_{OM}\bar{n}_{min} + \Gamma_m\bar{n}_{th}}{\Gamma_{OM}+\Gamma_m}$$

where $\bar{n}_{th} = (e^{\frac{\hbar\omega_m}{k_B T}} - 1)^{-1}$ is the average phonon occupancy of a thermal bath at temperature T, k_B is Boltzmann's constants, and $\bar{n}_{min} = \left(\frac{\kappa^2+(\Delta-\omega_m)^2}{\kappa^2+(\Delta+\omega_m)^2} - 1\right)^{-1}$ is the minimum phonon occupancy.

λ_c, λ_l	L	$\omega_m/2\pi$	$\Gamma_m/2\pi$	m_{eff}	Δ
1550 nm	100 mm	140 kHz	1.4 mHz	1 ng	$-\omega_m$

Table 4.1: Nominal parameters for cooling estimates.

R_{phc}	$2\kappa/\omega_m$	C_0	$\bar{n}_f$	Q_{eff}
95%	85	0.1	180 000	410 000
99.3%	12	0.8	90	188
99.9%	1.8	5.1	0.7	1.4

Table 4.2: Estimated cooling performance for a 2MC, assuming $R_2 = 99.999\,\%$ and $P = 100\,\mu W$.

Note that $g_0 = -\frac{\partial\omega_c}{\partial x} x_{zpf}$ depends on the configuration of the cavity through $\omega_c(x)$. We estimate $\bar{n}_f$ and Q_{eff} starting from room temperature for two different configurations of particular interest, namely the 2 Mirror (2MC) and the 3 Mirror (3MC) Configurations, described below. For both configurations we use the parameters indicated in table 4.1.

TWO MIRROR CONFIGURATION (2MC)

In a 2MC, the cavity is composed of two mirrors, in which one of them is the mechanical resonator. In this case,

$$\omega_c^{2MC}(x) = n\frac{c}{2x},$$

where n is the index of the cavity resonance of interest. If we let one of the mirrors be a distance x away from a predefined cavity length L, $\omega_c(x) = n\frac{c}{2(L+x)}$. For small x we get $-\frac{\partial\omega_c}{\partial x} = -n\frac{c}{2L^2} = \frac{\omega_c(L)}{L}$. Simplifying the notation $\omega_c(L)$ by ω_c we get

$$g_0^{2MC} = \frac{\omega_c}{L}\sqrt{\frac{\hbar}{2m_{eff}\omega_m}}.$$

We now calculate the achievable average phonon occupancies and mechanical quality factors from cooling membranes such as the ones presented in this letter, in a configuration where the membranes are used as input mirrors R_{phc} in a 2MC in combination with a second mirror with reflectivity R_2. Taking $R_2 = 99.999\,\%$ and $P = 100\,\mu W$, we show the estimated $\bar{n}_f$ and Q_{eff} for several values of R_{phc} in table 4.2. Here $C_0 = 4g_0^2/\kappa\Gamma_m$ is the single-photon cooperativity and $2\kappa/\omega_m$ is the sideband resolution parameter. While in such a configuration it is not possible to enter the ground state regime with our currently best reflectivities of 99.3 %, future minor improvements in fabrication and design will allow us the reach the required reflectivities of around 99.9 %. In addition, as is shown in the next section, a membrane in the middle approach (3MC) allows us to realistically cool to the quantum mechanical ground state with our current devices.

THREE MIRROR CONFIGURATION (3MC)

In a 3MC, the membrane is placed at an arbitrary position x between two high highly reflective mirrors which are separated by a fixed distance L. In this case [37],

$$\omega_c^{3MC}(x) = \omega_c\left[2\phi_r + 2\cos^{-1}\left(|r_m|\cos\left(\frac{4\pi}{\lambda_c}x\right)\right)\right]$$

F	$2\kappa/\omega_m$	C_0	$\bar{n}_f$	Q_{eff}
3400	3.2	11	0.95	1.3
4100	2.6	13	0.67	1.0
18000	0.6	58	0.10	0.3

Table 4.3: Estimated cooling performance for a 3MC assuming a PhC reflectivity of 95 %, the lowest reflectivity achieved by our devices, and $P = 10\,\mu W$.

where r_m is the amplitude reflectance coefficient of the membrane, $\phi_r = \arg(r_m)$, and λ_c is the cavity wavelength. Note that $-\frac{\partial\omega_c(x)}{\partial x}$ is optimal for $\frac{4\pi}{\lambda}x = \frac{\pi}{2} + n\pi$. Assuming the membrane is positioned at such an optima and that it is allowed to move a small distance ϵ away from the optimum, i.e. $\frac{4\pi}{\lambda}x = \frac{\pi}{2} + \epsilon$, it is possible to approximate $\omega_c(\epsilon) \approx \omega_c\left[2\phi_r - 2|r_m|\epsilon\right]$. As such, $-\frac{\partial\omega_c(x)}{\partial x} = -\frac{4\pi}{\lambda}\frac{\partial\omega_c(\epsilon)}{\partial\epsilon} = 2|r_m|\frac{\omega_c}{L}$ and we get,

$$g_0^{3MC} = 2|r_m|\frac{\omega_c}{L}\sqrt{\frac{\hbar}{2m_{eff}\omega_m}}.$$

The advantage of this configuration is that the optomechanical mirror with reflectivity $|r_m|^2 = R_{phc}$ can be positioned inside a cavity where the finesse F is only determined by the fixed mirrors and not by the membrane reflectivity itself. In such an approach the influence of the membrane's optical properties on the achievable cooling performance is significantly smaller compared to the case for 2MC. Even when using our design with the lowest reflectivity $R_{PhC} = 95\,\%$, $P = 10\,\mu W$, we see that occupancies below 1 phonon are easily accessible with a modest finesse cavity. In table 4.3 the estimated $\bar{n}_f$ and Q_{eff} for varying cavity finesse are shown. In particular, for $F = 4100$ we estimate $\bar{n}_f = 0.67$ and $Q_{eff} = 1.0$. These calculations show that our novel designs place the quantum ground state of an optomechanical device at room temperature well within experimental reach.

4.6.2. RESONATOR DESIGN

Our devices are designed and optimized by performing a systematic analysis of several parameters of the tethered membranes (see figure 4.1, main text) in order to enhance the $f_m \times Q_m$ product. Parameters we studied are the size of the central membrane (a_{mem}), width of the tethers (w), total size of the window (a_w), fillet radius connecting the tethers to the central membrane (r_{in}), fillet radius connecting the tethers to the substrate (r_{out}), diameter of the photonic crystal mirror (PhC) (d_{phc}), Si_3N_4 film thickness (t_f) and silicon substrate thickness (t_s) to measure their effects on the $f_m \times Q_m$ product of the center-of-mass mode.

In order to measure the effects of the different design parameters on the mechanical quality factor and frequency we start with a set of nominal parameters and sweep each one while keeping all other parameters fixed. Our nominal parameters are: $w = 5\ \mu m$, $a_w = 700\ \mu m$, $a_{mem} = 100\ \mu m$, $r_{in} = 60\ \mu m$, $r_{out} = 20\ \mu m$. The following plots include a blue-dashed line representing the nominal value of the swept parameter. By changing the size of the inside and outside fillets we effectively change the length of the tethers. In order to decouple these parameters we change the size of the window, a_w, as a way to change the length of the tethers. While the relationship of these parameters

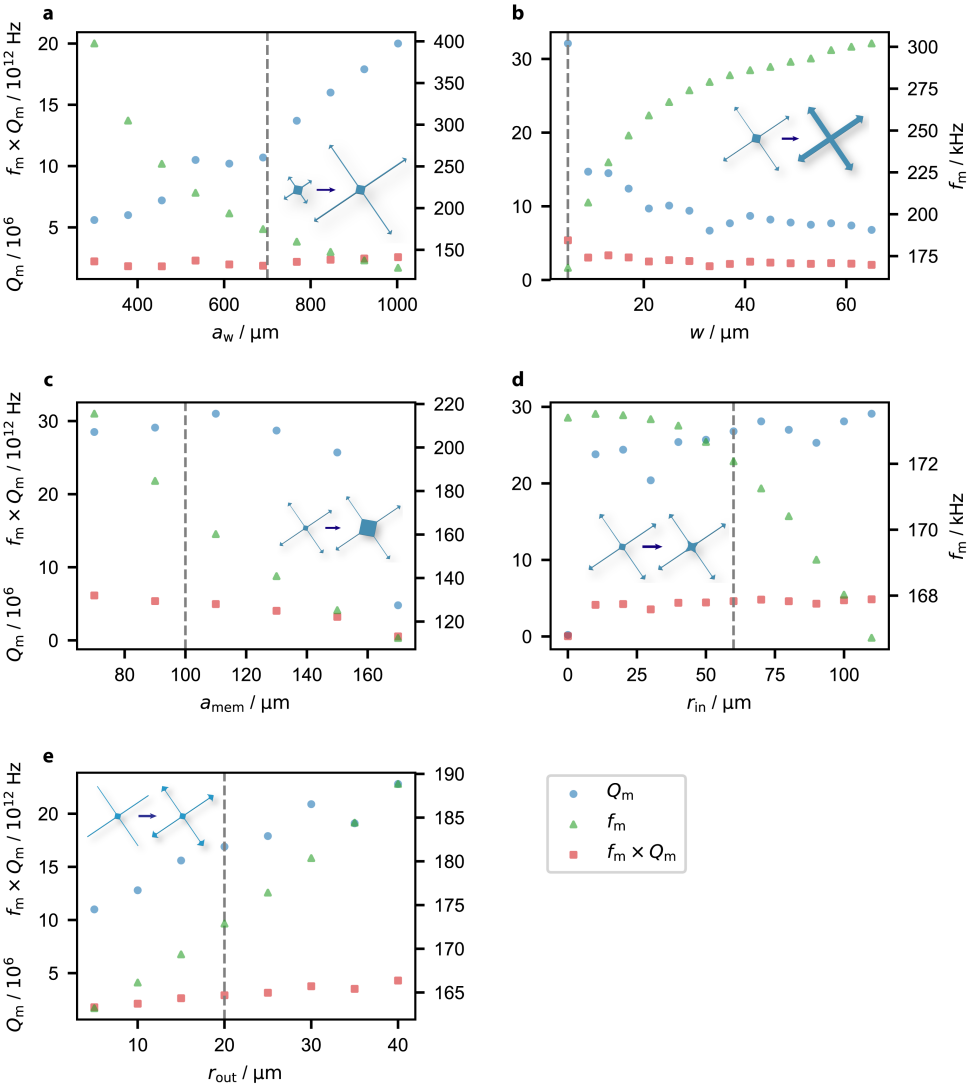

Figure 4.5: Frequency f_m, quality factor Q_m and $f_m \times Q_m$ of several devices with different geometry. In each subplot, a single geometrical parameter is varied: **a** tether length a_w; **b** tether width w; **c** membrane size a_{mem}; **d** inner fillet radius r_{out}; **e** outer fillet radius r_{out}.

with frequencies is experimentally robust, one of the main challenges is observing these parameters' effects on the mechanical quality factors which are susceptible to unavoidable fabrication imperfections due to small changes in handling and contaminants from sample to sample. To mitigate this effect, all resonators for these sweeps are fabricated with $t_f = 50$ nm and $t_s = 500$ μm, where we know that our quality factors are consistently

	f	Q_m	$f_m \times Q_m$
tether width w, ↑	↑	↓	=
window size a_w, ↑	↓	↑	=
membrane size a_{mem}, ↑	↓	↑	↓
inner fillet r_{in}, ↑	↓	↑	=
outer fillet r_{out}, ↑	↑	↑	↑
PhC diameter d_{phc}, ↑	=	=	=

Table 4.4: Using 50 nm thick Si_3N_4 films on 500 µm silicon substrates as a standard platform, we sweep all design parameters to determine their effect on f_m and Q_m. Here ↑ means an increase, while ↓ a decrease of the associated value. Most parameters suffer from a trade-off between f_m and Q_m, resulting in negligible enhancement (=).

high. The first parameter we investigate is the length of the tethers which we effectively vary by changing the size of the square window (a_w). As shown in figure 4.5a, increasing the length of the tethers increases Q_m and decreases f_m, as expected, with almost no change in the $f_m \times Q_m$ product.

We next sweep the width of the tethers from the nominal value of 5 μm to 64 μm, which is the maximum width before the tethers begin to overlap (figure 4.5b). We measure the mechanical frequency increase and quality factor decrease towards a plateau near 7×10^6, which is also the quality factor for a 50 nm thick square membrane of 700 μm. Intuitively in the limit of increasing tether width the tethered membranes begin to resemble square membranes where the tether width can no longer be properly defined and only the size of the window, a_w, defines the lateral geometry of the membrane. We see a large enhancement in Q_m from 15×10^6 to 32×10^6 when we decrease the tether width from 9 μm to 5 μm as the membranes losses begin to be dominated by clamping losses associated with strings ($Q_{clamp} \propto a_w / w$).

From finite element simulations we know that the contraction of relaxing material in the central membrane plays a key role in the enhancement of stress in the tethers. We sweep the size of the central membrane, a_{mem}, in order to see how it enhances the stress in the tethers and ideally increases $f_m \times Q_m$. As we increase a_{mem}, we simultaneously also increase a_w to keep the length of the tethers constant. We find that the mechanical quality factors remain at nominal values while the frequency drops dramatically as the resonator mass increases quadratically (figure 4.5c). In this case, $f_m \times Q_m$ improves with decreasing membrane size. From a practical standpoint, the optimal size of the membrane is set by the minimum cavity beam waist which can still achieve large reflectivities from the photonic crystal on the central membrane. By using a small beam waist the size of the central membrane can be minimized in order to increase $f_m \times Q_m$, with the limit of good mode overlap with the photonic crystal to achieve high reflectivities. A beam waist of 20 μm gives us maximal reflectivity and requires a minimum photonic crystal mirror with $d_{phc} \sim 80$ μm in order to overlap the tails of the Gaussian beam.

In addition, as the inner fillet radius r_{in} between tethers and central membrane is increased, there is a slight increase in quality factor with a large decrease in frequency as the mass of the central membrane increases (figure 4.5d)

We also vary the size of the outer fillet radius between the tether and the edge of

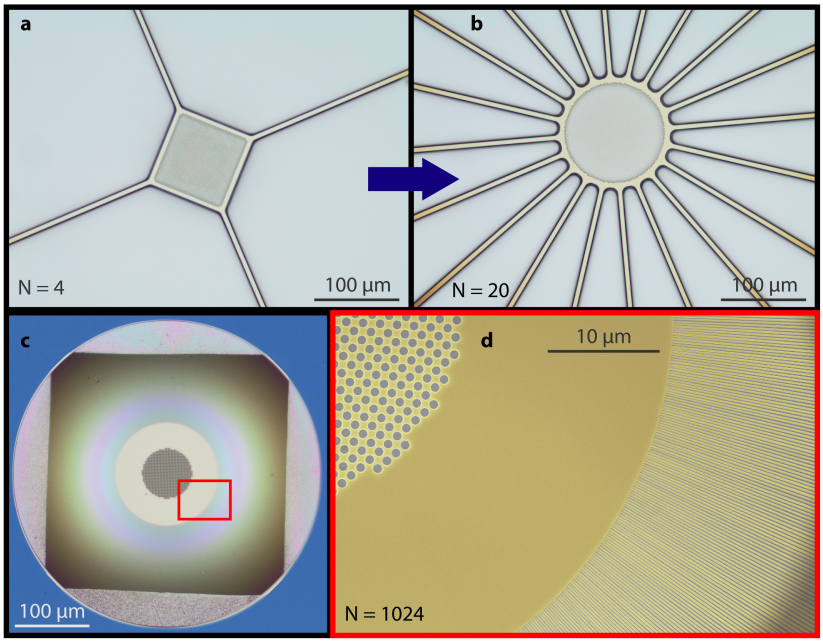

Figure 4.6: Sweep of the number of tethers N. **a** $N = 4$. **b** $N = 20$. **c** $N = 1024$. **d** Zoom-in of the region in **c** marked in red.

the window. As we increase r_{out} we see the mechanical quality factors and frequencies increase as the length of the tethers are effectively shortened. It is however difficult to directly compare resonators with different outer-fillet shapes since larger outer-fillets require longer KOH release times. The increased etching times also widens the overhang around the perimeter of the window, which we find to lower the mechanical quality factors for nominal dimensions (figure 4.5e).

Table 4.4 contains a summary of the results of these geometry sweeps, where we indicate how they influence f_m, Q_m and $f_m \times Q_m$.

Last but not least, we also vary the number of tethers connecting the central membrane to the substrate, N. We sweep it from $N = 4$ to $N = 20$ as shown in figure 4.6(a,b) while keeping all other parameters nominal. The observed shift in frequency in these "pinwheel" flexural resonators is from 170 kHz ($N = 4$) to almost 350 kHz ($N = 20$). In order to keep the lengths of the tethers equal, a rotationally symmetric design is required. In figure 4.6(c,d), we show a resonator with $N = 1024$ tethers, each 500 nm wide, and a square hole through the substrate for optical access. This large-N design exhibits frequencies around 1 MHz, with $Q_m \sim 10^6$, which could be an interesting approach to further mitigate classical laser noise. An important fabrication challenge for such devices is to keep the overhang at the perimeter of the resonator to a minimum in order to reduce radiative losses into the substrate. The smallest overhang we were able to attain was ≈ 8 μm wide, which incurred significant losses resulting in $Q_m \sim 1\text{-}3 \cdot 10^6$. The nominal

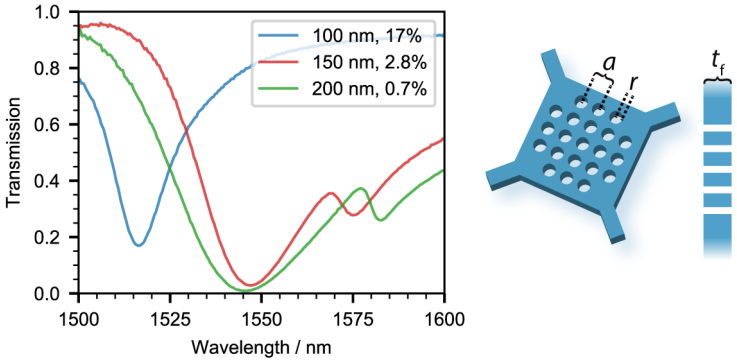

Figure 4.7: The measured transmittance of the tethered mechanical membranes as a function of silicon nitride thickness for a standard photonic crystal design of an array of holes (Fig 4.2a). The legend indicates the film thickness and the minimum of the transmission.

design ($N = 4$) keeps the overhang to a minimum due to the nature of rectangular crystal lattice etching of ⟨100⟩ silicon.

4.6.3. PHOTONIC CRYSTAL THICKNESS

Using FDTD simulations we are able to optimize for the most reflective design at different photonic crystal thicknesses ($t_{PhC} = 100, 150, 200$ nm) for 1550 nm light. In our simulations we sweep the lattice constant a and r/a, where r is the radius of the holes. Using these parameters, we are able to experimentally verify the FDTD results which show increased maximum reflectivity with increasing thickness of the photonic crystal t_{PhC} (see figure 4.7). While we only plot transmittance measurements for clarity, we also experimentally confirm that the reflectivity $R = 1 - T$ to within our measurement error by using the membranes as part of a Fabry-Perot cavity in conjunction with another mirror with known reflectivity.

5

LARGE-AREA, SUSPENDED PHC MIRRORS

Demand for lightweight, highly reflective and mechanically compliant mirrors for optics experiments has seen a significant surge. In this aspect, photonic crystal (PhC) membranes are ideal alternatives to conventional mirrors, as they provide high reflectivity with only a single suspended layer of patterned dielectric material. However, due to limitations in nanofabrication, these devices are usually not wider than 300 µm. *Here we experimentally demonstrate suspended PhC mirrors spanning areas up to* $10 \times 10\,\mathrm{mm}^2$. *We overcome limitations imposed by the size of the PhC and measure reflectivities greater than* 90 % *on* 56 nm*-thick mirrors at a wavelength of* 1550 nm*–an unrivaled performance compared to PhC mirrors with micro-scale diameters. These structures bridge the gap between nano-scale technologies and macroscopic optical elements.*

This chapter has been published together with R.A. Norte, J. Guo, C. Schäfermeier and S. Gröblacher in Optics Express **26** (2), 1895–1909 (2018) [114]

5.1. INTRODUCTION

PHOTONIC crystal (PhC) membranes are suspended dielectric sheets patterned with sub-wavelength, low-index two-dimensional periodic structures [48]. These patterns give rise to resonances that couple out-of-plane radiation to in-plane leaky modes, and can be engineered to transform a flat membrane into a mirror [45], a lens [115], or even a curved mirror [115–117]. Here we study a PhC consisting of a periodic lattice of holes in a membrane, whose hole radius and lattice constant can be tuned to reflect light at a wavelength of choice. When fabricated from materials with low optical absorption such as low-pressure chemically vapor-deposited silicon nitride (LPCVD SiN), one can realize mirrors with sub-wavelength thicknesses and reflectivities > 99 %, mostly limited by scattering losses, as shown in [58]. LPCVD SiN thin films also enable the combination of PhC mirrors with low thermal noise mechanical oscillators, due to their high intrinsic stress, thin geometry, and weak coupling to undesired thermal modes [67, 112].

Microfabrication processes have so far restricted suspended PhC mirrors to areas around $300 \times 300\,\mu m^2$ [58]. This size sets an upper bound to the waist of incident Gaussian beams, since wider waists do not completely interact with the PhC, resulting in decreased reflectivity. But the waists also have a lower bound: very small waists have a high divergence and couple to undesired PhC modes, which leads to shifting, broadening and shallowing of the high-reflectivity crystal resonance. These adverse finite-size effects have been consistently measured in very thin mirrors with thicknesses below 0.1λ, where λ is the wavelength of the reflected light [67, 98, 118, 119]. The ability to fabricate larger PhC mirrors with increasingly thinner membranes could greatly facilitate the combination of high reflectivity and low mechanical losses [67]. These properties indicate the potential that PhC mirrors may have for reducing thermal mirror coating noise which stands as a limit in precision measurements such as atomic clocks [120], frequency-stabilized lasers [121], and gravitational wave detectors [122]. At the centimeter scale, PhC mirrors could have more immediate applications as deformable mirrors with adjustable wavefront [123], or evanescent field sensors with a large interaction area [124, 125].

In this letter we experimentally demonstrate free-standing SiN photonic crystal mirrors with thicknesses of 56 and 210 nm and areas of up to $10 \times 10\,mm^2$. Not only do we increase the area of suspended PhC mirrors by nearly 4 orders of magnitude compared to previous works, we also show that these large aspect-ratios allow us to achieve high reflectivity from membranes thinner than previously measured. We observe greater than 90 % reflectivity of 1550 nm light from mirrors with a thickness of 0.038λ (56 nm) – a significant increase compared to previous devices with similar thickness and wavelength [118]. Such large structures allow studying the spectrum of PhC membranes as a function of incident beam waist with less constraints from finite size effects.

5.2. METHODS

Our suspended PhC mirrors are fabricated from high-stress (1 GPa) LPCVD SiN films deposited on 200 µm Si wafers. The geometry of the PhC structures is optimized for each desired film thickness to a wavelength of 1550 nm using finite-difference time-domain

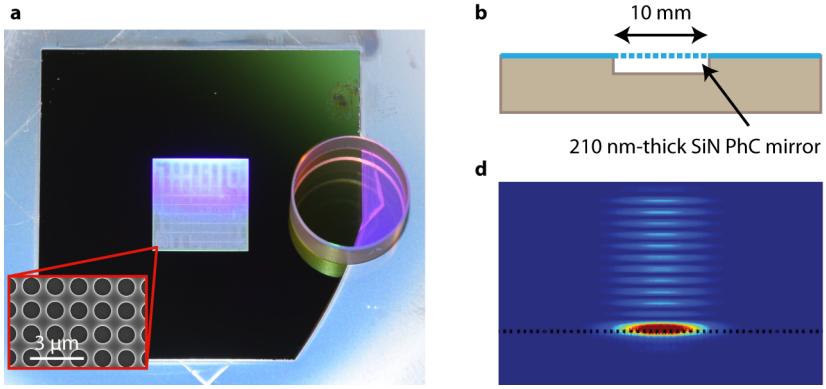

Figure 5.1: **a** Photograph of a 10 mm-wide, 210 nm-thick PhC mirror next to a commercial $1/2''$ mirror for size comparison. The rectangular shaped patterns within the PhC are stitching errors from the mainfields of the beamwrite, which do not affect the measured reflectivity significantly. The inset shows a scanning electron microscope picture of the actual photonic crystal. The full mirror is made up of around 6×10^7 holes. **b** Cross-section schematic of the device. The thin membrane is made of SiN and is supported by a silicon chip. **c** FDTD simulation of a reflected light mode on a PhC membrane.

(FDTD) simulations [48]. The structures are patterned on the SiN films using electron beam lithography and a plasma etching process ($CHF_3 + O_2$). Stitching errors occur about every millimeter due to stage drifts during the beamwrite and are on the order of 1 µm wide. One of the fundamental challenges for large aspect-ratio membranes is suspending them without causing any fractures. Typically liquid etchants such as KOH or TMAH are used to release free-standing SiN structures from their Si substrates. However, such wet processes produce a number of forces, like turbulences and surface-tension at the interfaces, which can easily destroy the fragile suspended PhC mirrors. These methods also leave residues that negatively impact the optical performance of the mirrors, requiring additional liquid cleaning steps that decrease the the fabrication yield, specially for large area devices [107]. In order to overcome these limitations, we have developed a stiction-free RIE-ICP plasma release using SF_6 [126]. A hot piranha solution consisting of sulfuric acid and hydrogen peroxide is first used to remove surface contaminations on the unreleased structures. This is followed by a diluted HF solution to smoothen the SiN surface [127] and remove surface-oxide from the silicon which allows for an even release of the membrane. Finally, we suspend the PhC mirrors using the SF_6 plasma release. Figures 5.1a-c show a photograph of a 10 mm-wide, 210 nm-thin mirror, a scanning electron microscope picture of the PhC pattern, a cross-section schematic of the device and numerical simulations of the reflected optical field.

In order to characterize the optical properties of the PhCs, we fabricate three devices with different thickness and size: two 210 nm-thick mirrors, $4 \times 4\,mm^2$ and $10 \times 10\,mm^2$-large; and a 56 nm-thick, $1.6 \times 1.6\,mm^2$-large one. We measure the mechanical spectrum of the fabricated devices to match those of bare square membranes with the same intrinsic stress. This indicates that despite the unconventionally large areas, the material stress remains high, which should guarantee the membrane's flatness, an important point when developing high reflectivity mirrors. This is also a relevant observation when

estimating the thermal displacement noise of this type of device. More details can be found in section 5.5.1.

The devices are characterized by focusing a wavelength-tunable laser beam perpendicular to the PhC mirrors. We measure the reflected and transmitted power and compare it to a reference beam that does not interact with the devices. For calibration, we use a commercial broadband mirror at the same position as the PhC mirrors. The laser is tuned from 1530 to 1630 nm. The recorded signal is normalized to the reference arm and to the calibration mirror to obtain the reflectivity spectra for multiple beam waists. We vary the beam radius between 8 µm and 1.1 mm using a lens system placed in front of the PhC membranes. This allows us to analyze the behavior of PhC membranes with different thicknesses to laser beams of varying sizes. For more details see 3.3.

5.3. RESULTS

Figure 5.2 shows a selection of measured spectra of the 210 nm-thick, $4 \times 4\,\mathrm{mm}^2$-large and the 56 nm-thick devices. While the PhC is completely released, for testing purposes the chip itself is not fully etched through (cf. figure 5.1b). This results in a parasitic interference pattern with a periodicity of 1.8 nm on top of the expected PhC spectra, corresponding to a 200 µm-thick Si etalon. Since the frequency of this interference is well defined, we post-process it by band-pass filtering the data. Section 5.5.2 contains the full set of acquired spectra, as well as a detailed description of the data processing.

The spectra of the 210 nm-thick PhC mirror, shown in figure 5.2a, exhibit a resonance at 1549 nm that varies little with the incident beam waist. At 1573 nm a parasitic resonance emerges whose width increases as the waist becomes smaller. This can be understood by considering the decomposition of a Gaussian beam with waist w_0 into plane waves [44]. The decomposition in terms of incidence angle is weighted by a Gaussian distribution with a standard deviation equal to the beam divergence $\theta = \lambda/\pi w_0$. A large waist w_0 has a small divergence θ, which is a good approximation to a plane wave with a zero angle of incidence. As w_0 decreases, θ becomes larger, and so plane waves with larger angles of incidence have a stronger weight on the decomposition. These waves can couple to PhC modes other than the resonance of interest, giving rise to parasitic features such as the one observed. We can apply the same reasoning to explain the increase in maximum reflectivity of the main resonance: the device geometry was optimized assuming a plane wave with normal incidence. Hence, beams with a large waist approximate this condition better, which results in a reflectivity closer to the optimized one.

In figure 5.2b we observe that the main resonance of the 56 nm-thick membrane exhibits stronger shifts in wavelength, width and maximum reflectivity with varying beam waist, in comparison to the 210 nm-thick device. As explained in the work of Bernard et al. [118], the spectral response of plane waves incident on a PhC mirror depends on the angle of incidence. This dependence is stronger for thinner devices and results in large resonance wavelength shifts. Therefore, as the beam waist decreases – and its divergence increases – the reflectivity of thin devices is more strongly attenuated. On the other hand, due to the small size of the 56 nm-thick PhC mirror (area of $1.6 \times 1.6\,\mathrm{mm}^2$ vs. $4 \times 4\,\mathrm{mm}^2$ for the 210 nm-thick device) beams with waists larger than 280 µm are partially scattered

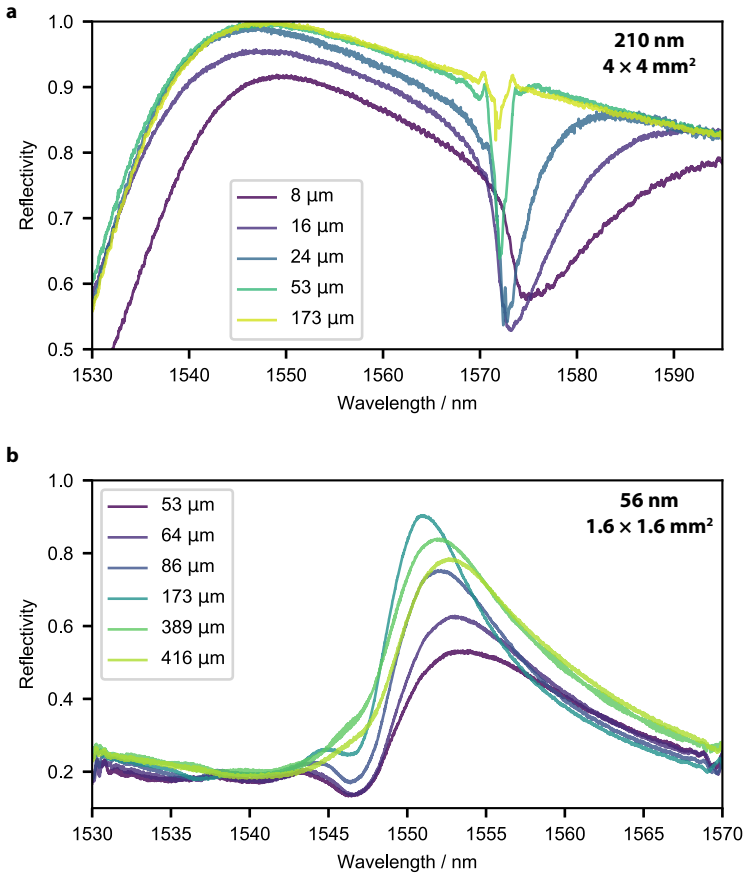

Figure 5.2: Reflectivity spectra of the PhC mirrors. Shown is a selection of measured reflectivity spectra of PhC mirrors with film thickness of **a** 210 nm and **b** 56 nm. Each spectrum shows the reflection of a Gaussian beam with the specified waist. As the waist increases, the incident beam approaches the behavior of a plane wave, for which the devices are optimal, and so the maximum reflectivity increases. Due to the finite size of the 56 nm PhC mirror, its reflectivity drops as the incident beam becomes larger than the PhC area. The data were digitally processed to remove parasitic interferences from the substrate (see section 5.5.2 for details).

outside the PhC and exhibit a decreasing maximum reflectivity (see below).

Figure 5.3 shows the maximum reflectivity of all PhC membranes as a function of the incident beam waist. As described in the previous paragraphs, larger beam waists approximate the design conditions of the PhCs better, reducing the amount of light that couples to unwanted modes. As such, the maximum reflectivity increases for larger beams. We verify this behavior with simulations and plane wave decomposition: starting with the geometry parameters that resulted from the FDTD optimization and that were patterned on the SiN membranes, we simulate the reflectivity of plane waves with varying angles of incidence at the resonance wavelength using rigorous coupled-wave analysis (RCWA) [128]. The reflectivity at each beam waist is then the weighted sum of the simulation results, following a Gaussian distribution with standard deviation θ,

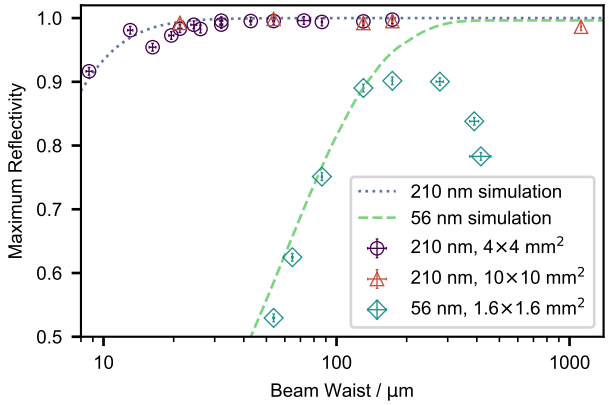

Figure 5.3: Maximum reflectivity as a function of incident beam waist. We show the maximum reflectivity for several PhC thicknesses and membrane sizes, highlighting the potential of these structures as large-area, high-reflectivity mirrors. For comparison, we include simulations, represented by lines, obtained from plane wave decomposition of Gaussian beams using RCWA. The reflectivity of the 56 nm-thick PhC mirror decreases when the optical beam becomes comparable to the PhC diameter, underlining the importance of finite size effects. The measured data have an uncertainty in reflectivity of ±0.6 %. The uncertainty in the beam radii results from propagating the estimated uncertainties in the positions of the lens sets. For more details see section 3.3.

5

which is further described in section 5.5.3.

The reflectivity of the 56 nm-thick PhC mirror decreases when the beam radius measures between 280 and 390 µm. Considering that the field amplitude of a Gaussian beam falls as e^{-r^2/w_0^2}, where r is the distance from the beam's center, we expect 99 % of the field to be within a diameter of $6 \times w_0$. Since the PhC measures $1.6 \times 1.6\,\mathrm{mm}^2$, beams with waists larger than 1.6/6 mm = 270 µm will have larger field components reflecting off the area outside the PhC. This allows us to observe a smooth transition between two regimes: one, for small waists, where the PhC response is limited by a large beam divergence and another one for large waists, where the limitation is the finite size of the device. Between these two bounds we see a plateau where the maximum reflectivity >90 % is approximately constant. To the best of our knowledge, this is the highest reported reflectivity of a 56 nm suspended PhC mirror, operating in a regime with lower beam divergence and finite size limits.

5.4. CONCLUSION

In conclusion, we fabricate and characterize the first suspended PhC mirrors that span areas up to square-centimeters, with reflectivities exceeding 99 %, which are only limited by our measurement precision. Previous attempts focused on devices not wider than 300 µm, resulting in strong limits to the maximum achievable reflectivity, in particular for devices thinner than 0.13λ. By measuring the reflectivity spectrum of the PhC mirrors for varying incident beam waists, our work shows that these devices are indeed strongly affected by finite size effects. In particular, we observe a reflectivity of 90 % for a 0.036λ-thick PhC mirror at a wavelength of 1550 nm, whereas previous reports of devices with similar thickness were limited to 62 % [98, 118]. Despite the presence of fabrication

errors in the lithography process for the largest device (see figure 5.1a), we suspect that its performance becomes insensitive to small defects in the PhC lattice for large beam waists, since the reflectivity shows no appreciable changes with increasing waists (see figure 5.3, 210 nm data). Since larger incident beams sample a larger area of the PhC structure, we observe that the reflectivity seems robust to imperfections in the 2D array of holes that arise from drifts or poor stitching during lithography. It is also important to note that these mirrors could be improved even further with more sophisticated methods of lithography. Electron beam lithography is prone to stage drifts during exposure and secondary back-scattering of electrons from the substrate which produce uneven dosing – both of these effects can lead to an inhomogeneous lattice constant and variations in hole size. We envision scaling these devices further to full wafer sizes by using techniques such as nano-imprint lithography, lithography stepping, or interference lithography [129].

Due to its high intrinsic stress, LPCVD SiN PhC membranes should remain relatively flat even at larger areas. Together with the low optical absorption of SiN, this is a promising platform for light sails in future space probes propelled by light, such as the Breakthrough Initiative Starshot [130]. In addition, high-stress SiN membranes have been shown to have high thermal noise suppression which becomes better with thinner, larger membranes [67]. At large scales, SiN PhCs could thus be an interesting route towards low-noise suspended mirror coatings. In section 5.5.4, we include a first-order estimate of the thermal displacement noise such devices would have, and make a baseline comparison of their performance to the well-documented mirror coatings used on LIGO test-masses.

Furthermore, the fact that these mirrors are suspended allows them to be used in a variety of applications that profit from mechanical tuning of mirrors. Deformable mirrors could be realized with these PhC structures [123], for example through electrostatic-tuning with arrays of electrodes close to the mirror, or even as displacement noise tunable mirrors, using techniques such as optomechanical feedback control [131]. Further experiments are planned to study the transversal mode composition of the reflected beam and to properly characterize the devices' optical absorption and scattering using a high finesse optical cavity. These developments open up a new paradigm in photonics – one that steers away from the focus on simply miniaturizing components, but instead tries to bring the performance of nano-engineered materials to large scales.

ACKNOWLEDGMENTS

We thank F. Alpeggiani, P. Klupar, A. Loeb, and P. Worden for helpful discussions. We also acknowledge valuable support from the Kavli Nanolab Delft, in particular from C. de Boer and M. Zuiddam, the European Research Council (ERC StG Strong-Q) and the Netherlands Organisation for Scientific Research (NWO/OCW), through the Frontiers of Nanoscience program.

5.5. SUPPLEMENTARY INFORMATION

5.5.1. MECHANICAL MODES OF PHC MIRROR

In order to get a better understanding of the mechanical properties of the PhC mirrors, a displacement spectrum was recorded for a $4 \times 4\,\mathrm{mm}^2$ mirror. The device was mounted in a vacuum chamber and a homodyne detector measured the phase quadrature of the back reflected light. Figure 5.4 shows a spectrum recorded in the center of the mirror and another spectrum measured at the edge of it. The off-center spectrum displays mechanical modes which have no net-effect on centered beams, i.e. modes which are mirror symmetric on two orthogonal axes. The fundamental mechanical frequency of a bare square membrane is given by

$$\omega_\mathrm{m} = \frac{2\pi}{\sqrt{2}L}\sqrt{\frac{\sigma}{\rho}}, \tag{5.1}$$

where L is the length the membrane, ρ is the material density ($2.7\,\mathrm{g/cm}^3$ for SiN), and σ is the tensile pre-stress in the film, which we take to be 1 GPa, a value defined by the parameters of the LPCVD deposition process. A square membrane with the same dimensions and material properties as the one discussed here has a fundamental frequency of 108 kHz. Comparing this to the value measured for our device (117 kHz) leads us to conclude that the pre-stress remains high even for these unconventionally large suspended areas.

To simplify the analysis, we model the structure as a simple square membrane without holes. Starting from the fundamental mode frequency of the device, we can calculate the frequencies of all higher-order modes [84], which we plot on the upper horizontal axis in figure 5.4. We observe a very accurate fit of the measured higher-order modes (the deviation is around 1 %). The measured spectrum also allows to predict the noise performance of an optical cavity made with such PhC mirrors [13].

5.5.2. POST-PROCESSING OF SPECTRAL DATA

Figure 5.5 shows the full, unprocessed set of measured reflectivity spectra for the **a** 210 and **b** 56 nm-thick devices. We measured the spectra for several incident beam waists, which are indicated in the figure legends. The spectra follow the expected Fano resonance shape, characteristic for this type of device.

In addition, we also see a parasitic oscillation with a periodicity of 1.8 nm. This is because the devices are suspended but the substrate is not etched through. In fact, to facilitate the testing process, the membranes are undercut by only a few µm on top of the 200 µm silicon substrate (cf. figure 5.1**b**). The observed periodic pattern arises from interference of reflections from the substrate interfaces. Using the thickness of the silicon substrate and a refractive index of 3.5, we calculate a free spectral range of 1.7 nm for a wavelength of 1550 nm, which is in excellent agreement with the observed oscillations. The periodicity observed on the measured spectra is equal for all measurements and as such, we remove it digitally using the procedure described below.

The Fourier transformations of the unprocessed reflectivity spectra show peaks that are well defined and common to all measurements, which we associate with the described etalon effect. The peaks are marked by the dashed lines in figures 5.5**c** and **d**.

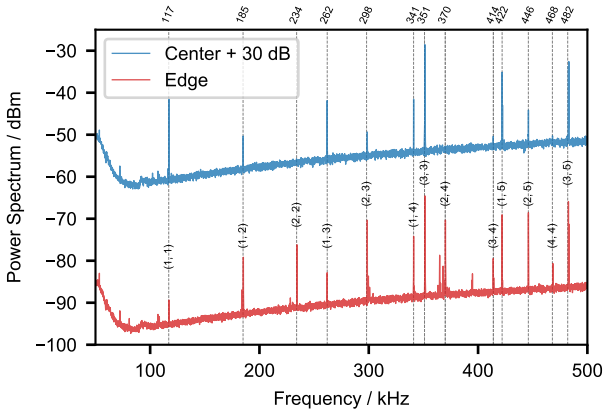

Figure 5.4: Measured mode spectrum. Shown is the spectrum of the back reflected light from a $4 \times 4\,\mathrm{mm}^2$ PhC sample detected with a homodyne detector. The optical power for this measurement was set to 1 mW, the resolution bandwidth to 100 Hz and the spectrum was averaged 50 times. The device was driven with a piezoelectric actuator connected to a white noise generator (peak-to-peak voltage 100 mV) inside a vacuum chamber at 1×10^{-5} mbar. Electronic and displacement noise from the mounting-frame were subtracted from the displayed data. We calibrated the noise from the mounting-frame by measuring a spectrum with the laser beam focused on the frame. The blue trace (top) shows data obtained with the laser focused in the center of the device, while for the red trace (bottom) the laser was focused onto the edge of the PhC mirror. The latter was done to record modes which have no net-effect on the reflected beam, e.g. a (2, 2) or (4, 4) mode. The theoretically expected mode frequencies are highlighted by the vertical dashed lines and match the measured spectrum very closely.

The Fourier transforms are obtained with the `fft.rfft` and `fft.rfftfreq` commands of the Python `numpy` library. To remove these parasitic features from the Fourier transforms, we apply a Tukey filter, with filter parameter 0.9, around the identified peaks. The filter was generated using the function `signal.tukey` from the `scipy` library. Finally, the filtered spectra are obtained by performing the inverse Fourier transform using the `fft.irfft` command. These can be seen in figures 5.5**e** and **f**. We carefully verify that filtering does not change the reading of the maximum reflectivity.

Figure 5.6 shows the raw data of the 210 nm-thick, 10 mm-wide device. This device was attached to a single-side polished carrier wafer using an index matching oil. Since the bottom surface of the substrate is rough, the interference between interfaces is no longer visible. Therefore this data set did not require any post-processing.

5.5.3. SIMULATED REFLECTIVITY SPECTRA FOR GAUSSIAN BEAMS

To simulate the expected reflectivity spectra of the PhC membranes, we use a rigorous coupled wave analysis (RCWA) [128] combined with a plane wave decomposition [132]. On the one hand, choosing a RCWA implies that the simulated spectra are valid only for periodic structures, i.e. spectral changes caused by diffraction effects at the membrane's edge cannot be recreated. As this approach commonly starts with a plane wave as the incident electromagnetic field, it also requires to implement a composition of plane wave spectra when dealing with Gaussian beams. On the other hand, a finite element analysis (FEA) can in principle be set up to compute spectra of a finite, e.g. $10 \times 10\,\mathrm{mm}^2$ large, PhC

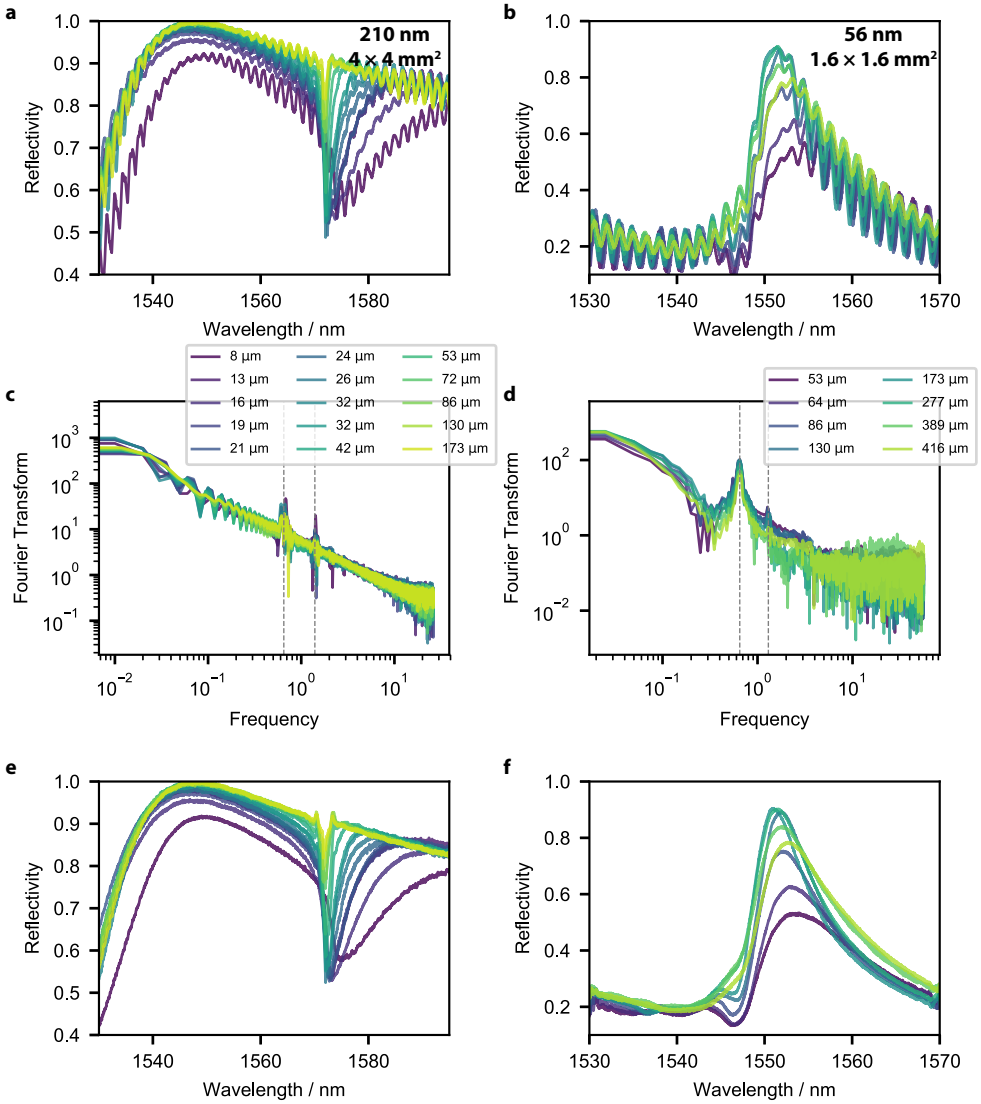

Figure 5.5: The plots show the **a**,**b** unprocessed reflectivity spectra, their **c**,**d** Fourier transformations, and the **e**,**f** filtered spectra of the PhC mirrors. The first column pertains to the 210 nm-thick, 4 mm-wide device, whereas the second column corresponds to the 56 nm-thick, 1.6 mm-wide one.

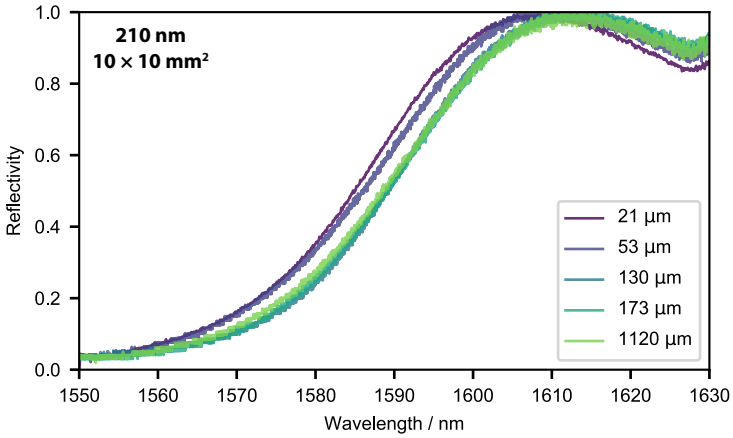

Figure 5.6: Unprocessed reflectivity spectra of the 210 nm-thick, 10 mm-wide device.

membrane excited by a Gaussian beam of waist w_0. However, the simplicity of a FEA approach has disadvantages when it comes to hardware, especially memory, requirements. To faithfully simulate the structure, the model volume has to cover about $20 \times 20 \times 1\,\text{mm}^3$ and still capture the details of the nano-scale membrane, which increases the memory usage drastically. A RCWA only discretizes the actual PhC membrane, such that the reflected field can be retrieved at any point above or below the structure. Finally, having simulated a set of plane waves via RCWA allows to assemble Gaussian beams of any size. For our requirements, the RCWA approach therefore is most appropriate.

We simulate two different unit cells:

- 210 nm thick, lattice constant 1.355 µm, hole radius 0.5014 µm
- 56 nm thick, lattice constant 1.526 µm, hole radius 0.6265 µm.

Each cell, composed of 140 modes, is excited at a certain wavelength with 66^2 plane waves of various polar and azimuthal angles of incidence. To verify that the structure is polarization insensitive, the wavelength- and angle scan is conducted for both s- and p-polarization. The simulation is built around an open source RCWA package [50], which rotates the s and p component of the incident field with respect to the incident angles. To align the polarization uniformly for all angles, the s- and p-electric field component E are transformed as

$$E_\text{s} \mapsto \cos(\theta)/\cos(\phi) \tag{5.2a}$$
$$E_\text{p} \mapsto -\sin(\theta) \tag{5.2b}$$

and

$$E_\text{s} \mapsto \sin(\theta)/\cos(\phi) \tag{5.3a}$$
$$E_\text{p} \mapsto \cos(\theta) \tag{5.3b}$$

for a s- and p-polarized beam, respectively. Here the polar angle is denoted by ϕ, while θ is the azimuthal angle. This set of transformations inverts the global rotation implemented in the software package.

Having computed the reflection coefficients $r_{\mathrm{s,\,p}}(\phi,\theta,\lambda) \in \mathbb{C}$ for a plane wave, the reflectivity of a Gaussian beam with the electric field distribution

$$E(x,y) = \sqrt{\frac{2}{\pi w_0^2}}\, e^{-\frac{x^2+y^2}{w_0^2}} \tag{5.4}$$

at the waist position ($z = 0$) is obtained by weighting the reflection coefficients according to the plane wave decomposition

$$E(k_x,k_y) = \iint_{-\infty}^{\infty} E(x,y)\, e^{\imath(k_x x + k_y y - \frac{2\pi c_0}{\lambda} t + \phi)} \mathrm{d}x\mathrm{d}y. \tag{5.5}$$

Transforming the expression to spherical coordinates, the power reflectivity spectra are computed via

$$R_{\mathrm{s,\,p}}(\lambda, w_0) = \frac{\iint \left| r_{\mathrm{s,p}}(\phi,\theta,\lambda) \right|^2 e^{-\frac{1}{2}(w_0 r \sin(\phi))^2} \sin(\phi)\mathrm{d}\theta\mathrm{d}\phi}{\iint e^{-\frac{1}{2}(w_0 r \sin(\phi))^2} \sin(\phi)\mathrm{d}\theta\mathrm{d}\phi}. \tag{5.6}$$

Figure 5.7 illustrates the results of the simulations for a 210 nm and 56 nm-thick unit cell with the parameters given above. Due to a small mismatch in the cell parameters the absolute resonance frequency of the measured and simulated spectra deviate from each other slightly, however the overall features of the measurement are recreated faithfully. The individual simulations of s- and p-polarization exhibit virtually no difference, which is an important as we probe the membranes with a circularly polarized beam. From the data plotted in figure 5.7, the maximum achievable reflectivity can be readily extracted by determining the peak reflectivity for each wavelength and beam waist scan. In figure 5.8 the results from the main text are plotted again and the simulated maximum reflectivity is shown for both polarizations. A zoom into the last two percent helps reading out the measured values.

5.5.4. ESTIMATION OF THERMAL DISPLACEMENT NOISE

Thermal mirror coating noise is currently one of the main limitations to the sensitivity of high-precision experiments including atomic clocks, frequency stabilized lasers and gravitational wave detectors. Widely used in these communities are distributed Bragg reflector (DBR) coatings made of alternating layers of dielectric materials. One challenge with DBR coatings is that their reflectivity has a natural trade-off with the number of layers used (and therefore the total thickness). Increases in coating thickness are usually associated with increases in coating's thermal Brownian noise. Attaining high reflectivity requires DBR surfaces which are commonly microns thick, while PhC mirrors can realize similarly high reflectivities with a membrane which is only the thickness of a single DBR layer. Additionally, their suspended geometry makes them into an easily deformable mirror surface, which potentially provides mechanical isolation from substrate (i.e. test mass) noise, and the possibility to dynamically tune the mechanical properties using optomechanical techniques.

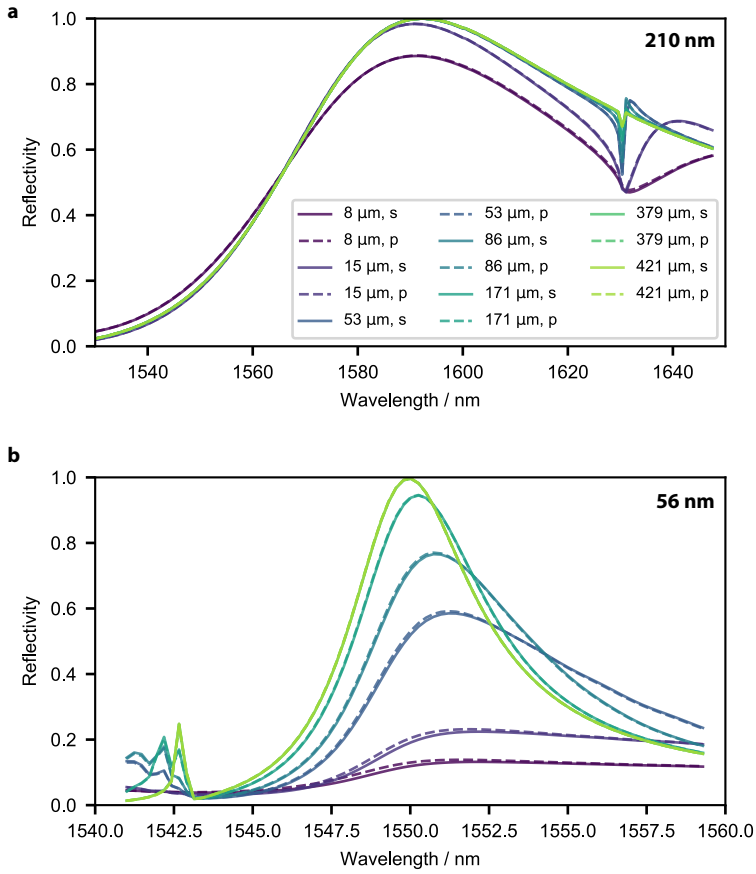

Figure 5.7: Reflectivity simulations for PhC membranes. Reflectivity spectra for s- and p-polarized Gaussian beams with the waist indicated on the legend. Panels **a** and **b** show data for a 210 nm and 56 nm-thick membrane, respectively.

In order to assess the potential that suspended PhC membranes could have in these types of applications, we perform a simplified calculation of the thermal noise performance of suspended PhC mirrors in this section and compare it to the thermal coating noise of the a-LIGO experiment [1].

For large LPCVD SiN mirrors we estimate the biggest noise contribution to be due to the thermal displacement noise, which for a square membrane is given by [24]

$$S_x(\omega) = \frac{4k_B T m_{\text{eff}} \omega_m / Q}{m_{\text{eff}}^2(\omega^2 - \omega_m^2)^2 + (\omega_m \omega / Q)^2}, \tag{5.7}$$

where Q is the mechanical quality factor, k_B the Boltzmann constant, T is the membrane's temperature, m_{eff} the effective mass of the membrane's fundamental mode, and ω_m its frequency given by eq. (5.1). The effective mass can be estimated with $m_{\text{eff}} = m/4$ [22], where m is the physical mass. It is further reduced by a factor of 0.3, which

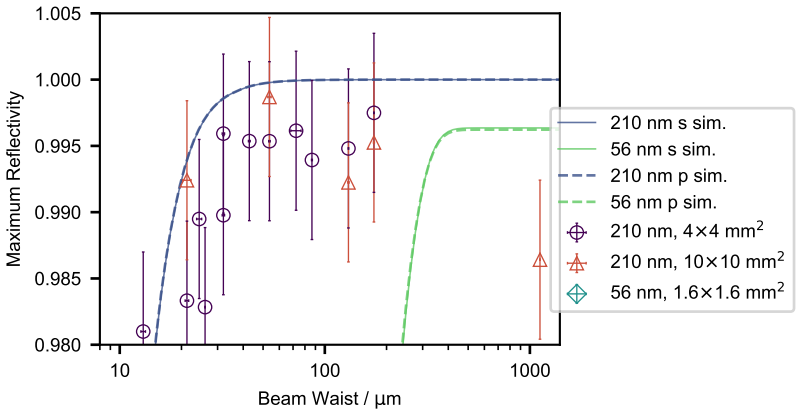

Figure 5.8: Extracted peak reflectivity compared to measured data. Shown are the same data as in the main text with additional simulations for various polarizations.

accounts for the mass lost to the PhC holes.

There are numerous limiting factors to the mechanical quality of a membrane [84, 101]: thermoelastic damping, surface defects, Akhiezer damping, etc. For LPCVD SiN membranes, the most relevant factors are acoustic radiation losses and damping from collisions with gas particles. The acoustic radiation losses into the substrate generally scale as the ratio between L and the thickness h: $Q_{\mathrm{rl}} \propto L/h$ [84, 101]. Considering previously measured radiation limited quality factors of 4×10^7 for $L/h = 5\times10^4$, we can extrapolate the radiation limit for arbitrary sizes of the PhC mirror. In addition, the quality factor limited by gas damping is given by [133]

$$Q_{\mathrm{p}} = \left(\frac{\pi}{2}\right)^{\frac{3}{2}} \rho h \frac{\omega_{\mathrm{m}}}{2\pi} \sqrt{\frac{RT}{m_{\mathrm{g}}}} \frac{1}{p}, \tag{5.8}$$

where R is the ideal gas constant, p is the pressure, and m_{g} is the molecular mass of the background gas molecules. The final Q is given by $Q^{-1} = \sum_i Q_i^{-1}$, where Q_i are the various contributions mentioned above.

In order to estimate the thermal displacement noise of suspended PhC mirrors, we need to assume some parameters. We chose those of the a-LIGO experiment, since its DBR coated mirrors are well known and characterized in terms of noise properties. This allows us to make a first-order comparison of how suspended PhC mirrors would operate when scaled up to the same size of the a-LIGO mirrors.

We take a SiN film thickness of 210 nm, a lateral size $L = 350$ mm, and effective mass $m_{\mathrm{eff}} = 12$ mg. We assume the mirrors are placed in a vacuum chamber at room temperature with a pressure of $p = 7\times10^{-9}$ hPa and that the main background gas component is hydrogen [1]. These parameters result in a fundamental mechanical frequency of $\omega_{\mathrm{m}}/2\pi = 1200$ Hz and a pressure-limited fundamental mode mechanical quality factor $Q_p \sim 10^8$. Considering a detection frequency of 100 Hz, we find a thermal displacement noise of around 10^{-17} m/$\sqrt{\mathrm{Hz}}$. For comparison, the thermal coating noise of the mirrors used in a-LIGO is of the order of 10^{-20} m/$\sqrt{\mathrm{Hz}}$.

These estimates are mainly limited by the environment pressure, which sets an upper bound to the mechanical quality factor. By decreasing the pressure further it could be possible to improve the thermal displacement noise significantly. Furthermore, suspended mirrors have the additional advantage that they can be adjusted, for example either through the addition of tuning electrodes or optomechanical techniques, in order to further reduce the noise performance in the desired regime.

It is important to note that the focus of this calculation is the estimation of thermal Brownian noise associated with the mirror coatings. The presented calculations and mirror designs are heuristic in nature and only allow one to make estimates comparing different mirror coating noise performances. It is however not entirely clear for example, how the Brownian noise related to the substrate (or test mass) would couple to such a suspended mirror. This could be relevant for monolithic cavities in quantum optomechanics experiments at room temperature, where substrate thermal noise is the dominant source of heating in laser cooling experiments [22]. In addition, it has been shown that at increasingly large aspect ratios the substrate thickness becomes a significant variable in a membrane's mechanical quality factor [67]. A massive substrate could work well in experiments which require large test masses. How these effects translate to the cm-scale remains an open question.

6

OPTOMECHANICAL ARRAYS OF TWO HIGH REFLECTIVITY MEMBRANES

Multi-element cavity optomechanics constitutes a direction to observe novel effects with mechanical resonators. Several exciting ideas include superradiance, increased optomechanical coupling, and quantum effects between distinct mechanical modes, amongst others. Realizing these experiments has so far been difficult, because of the need for extremely precise positioning of the elements relative to one another due to the high reflectivity required for each element. Here we overcome this challenge and present the fabrication of monolithic arrays of two highly reflective mechanical resonators in a single chip. We characterize the optical spectra and losses of these 200 μm*-long Fabry-Perot interferometers, measuring finesse values of up to* 220*. In addition, we observe an enhancement of the coupling rate between the cavity field and the mechanical center-of-mass mode compared to the single membrane case. Further enhancements in coupling with these devices are predicted, potentially allowing to reach the single-photon strong coupling regime, giving these integrated structures an exciting prospect for future multi-mode quantum experiments.*

This chapter has been published together with C. Gärtner, W. Haaxman, R. A. Norte and S. Gröblacher in Nano Letters **18** (11), 7171–7175 (2018) [134]

6.1. INTRODUCTION

CAVITY optomechanics explores light-matter interactions by using the established control techniques of optical resonators to manipulate highly sensitive mechanical oscillators [13]. A particularly successful direction is to dispersively couple suspended silicon nitride (SiN) membranes to a rigid optical cavity [14]. These so called membrane-in-the-middle (MIM) systems combine independent optical and mechanical oscillators, allowing the use of high finesse cavities to study a variety of mechanical devices. Although recent years have seen tremendous progress in quantum optomechanics and in particular with experiments observing quantum behavior of the mechanical mode [69, 135, 136], most have focused on single mechanical or noninteracting modes. Studying the behavior of multiple directly coupled modes could however allow probing new and exciting regimes of optomechanics [137], like superradiance, phonon lasing [138, 139], synchronization [140], the study of exceptional points [141], quantum information processing [142], as well as the direct entanglement of mechanical resonators [143]. It has also been suggested that the collective interaction of several mechanical oscillators can allow reaching the single-photon strong coupling regime [21]. This effect is based on reducing the effective optical mode volume through an array of closely spaced mechanical systems and it becomes stronger as the reflectivity of the individual systems R_m is increased.

Tethered SiN membranes patterned with photonic crystals (PhC) constitute ideal candidates for this type of experiments, as they have excellent mechanical properties, low mass, and high reflectivity due to the PhC which can be engineered to operate at a large range of wavelengths [67, 112]. To date, experimental efforts have focused on using independent mechanical membranes to create a mechanical array [39, 144], relying on the intrinsic reflectivity of the bare SiN, with one recent attempt to fabricate a membrane on each side of the same chip [145].

In the present work, we monolithically combine two tethered SiN membranes on a single chip and control their reflectivity using PhC patterns. This allows us to avoid having to manually align the mechanical elements to each other, which to date has been a major challenge with such high-reflectivity resonators. To compare the properties of devices with different reflectivity R_m, we fabricate pairs of single and double-membranes for three different PhC parameter sets, spanning R_m from 33 % to 99.8 % at an operating wavelength of 1550 nm. The optical spectrum of the arrays exhibits Fabry-Perot interference, which allows us to study the optical loss mechanisms present in the system. The optomechanical coupling rate of the center-of-mass (COM) mode of single and double-membranes to an optical cavity are compared. By changing the incident laser wavelength, we can operate the double-membrane stacks in their reflective or transmissive regimes, corresponding to enhanced or null COM optomechanical couplings, respectively.

6.2. DEVICE DESIGN AND FABRICATION

We fabricate our optomechanical devices on 200 nm of low-pressure chemical-vapor deposition (LPCVD) SiN deposited on both sides of a 200 µm-thick silicon (Si) substrate. A

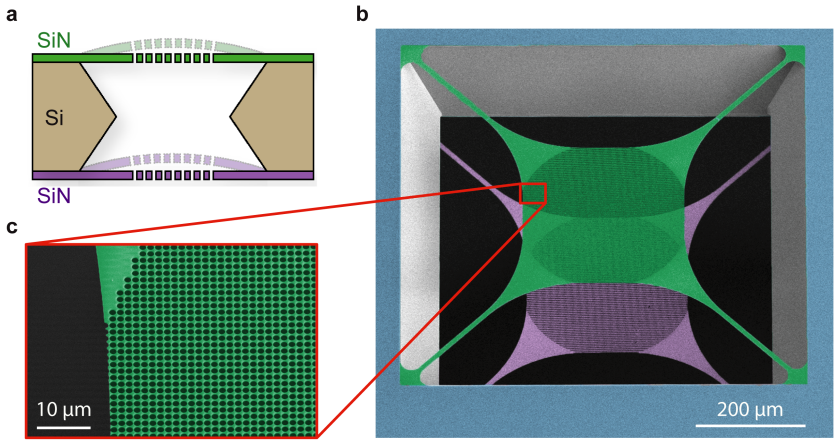

Figure 6.1: **a** Cross-sectional schematic of a released double membrane stack. **b** False-colored SEM image from the top under an angle of 37° showing a stack of two membranes as depicted in **a**. The top (green) and bottom (purple) SiN trampolines form a Fabry-Perot cavity. **c** Zoom-in of the PhC patterned central pad area of the upper membrane.

trampoline membrane is patterned on each side of the chip using electron-beam lithography and then etched into the SiN using a CHF_3/O_2 plasma etch. Finally, the Si in-between the trampolines is removed with KOH etching. Figure 6.1 shows a cross-section schematic of a final double membrane stack, as well as a false-colored SEM of one of our released devices.

At the heart of our devices is a central mirror pad on the tethered membranes. It is patterned with a two-dimensional PhC consisting of a periodic array of holes etched into the SiN device layer. Such a periodic change in the refractive index creates a band gap that can be tailored to a specific wavelength, resulting in reflectivities > 99.9 % [58, 67]. Using S^4, a Rigorous Coupled-Wave Analysis software, we simulate the spectrum of a given PhC pattern [146]. During fabrication, we can accurately tune the PhC resonance to our desired wavelength by adjusting the lattice constant a and hole radius r (see figure 6.6 for more details). We design three PhC patterns in order to obtain different R_m at our operating wavelength of 1550 nm. We refer to these patterns as *Low*, *Mid*, and *High R* and their geometries and measured R_m at 1550 nm are specified in table 6.1. The optical beam we use to probe the PhC has a waist size of about 50 µm. To avoid clipping losses, the diameter of the PhC pattern is 300 µm, while the tether length and width are 318 µm and 10 µm, respectively.

6.3. RESULTS AND DISCUSSION

For each PhC pattern (cf. table 6.1) we fabricate a single- and a double-membrane, which allows us to test all designs on a single chip, greatly facilitating the measurements. In the following subsections, we characterize their optical, mechanical, and optomechanical properties.

	a [nm]	r [nm]	R_m @ 1550 nm
Low R	1240	475	33 %
Mid R	1310	500	56 %
High R	1372	525	99.8 %

Table 6.1: Lattice constant a and hole radius r of the PhC patterns used in this work, as well as their measured reflectivity R_m at our operating wavelength of 1550 nm.

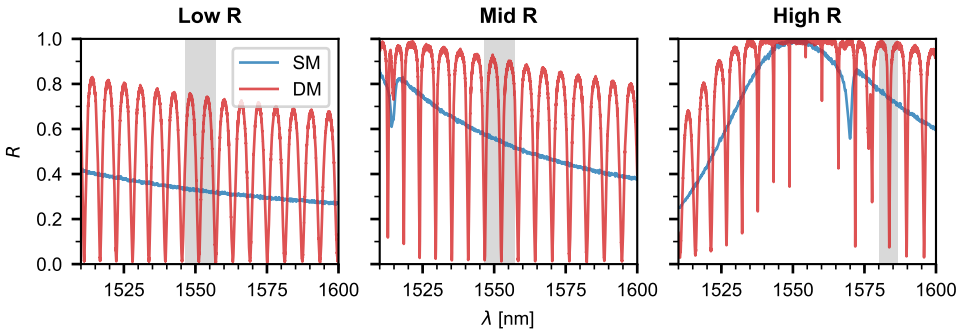

Figure 6.2: Reflection spectra of the devices. The photonic crystal pattern of each device is indicated at the top of each figure, according to the parameters in table 6.1. The blue traces correspond to devices composed of a single-membrane (SM), whereas the red traces are from double-membrane stacks (DM). The gray-shaded regions correspond to the wavelength ranges where the center-of-mass optomechanical coupling was measured (see figures 6.3 and 6.4).

6

6.3.1. OPTICAL CHARACTERIZATION

SINGLE MEMBRANES

We first obtain the optical spectra of the single devices by scanning a tunable laser from 1510 to 1600 nm and measure the reflected and transmitted signals from the PhC trampolines, which are shown in figure 6.2. At 1550 nm, we measure reflectivities of 33 %, 56 %, and 99.8 % for the Low, Mid, and High R samples, respectively. Because this measurement procedure has an uncertainty of 0.5 %, we determine the dispersive effect of a device similar to the High R sample on an optical cavity to obtain a lower bound on its transmission at resonance [57, 58]. We measure a transmission of 2.5×10^{-5}, comparable to the best reported results in the literature [58]. Finally, we simulate a PhC membrane with an imaginary component of the refractive index of 1.9×10^{-5} [57], and estimate that a fraction of 3.4×10^{-4} of the light is lost when interacting with the devices, due to either absorption or scattering from fabrication imperfections (see section 6.5.3 for more details).

DOUBLE-MEMBRANE ARRAYS

The double-membrane arrays have the same PhC design as the individual membranes and we determine their optical response in a similar way, shown in Figure 6.2. These structures can be modeled as plane-parallel etalons (fig. 6.1) and the characteristic features of Fabry-Perot interferometers can be clearly observed in their spectra. The free spectral range FSR_{DM} of 750 GHz, or 6 nm at a wavelength of 1550 nm, is, as expected,

defined by the 200 µm thickness of the Si substrate that separates the two membranes. The linewidth of the resonances becomes smaller as the reflectivity of the individual membranes increases. This is particularly prominent on the High R sample, where the full-width at half-maximum linewidth changes from 176 GHz at 1521 nm to 8.7 GHz at 1554 nm, corresponding to a change in finesse F from 4.3 to 86. Our best performing samples exhibit linewidths as low as 3.3 GHz ($F = 220$), suggesting a total loss per round-trip of approximately $2\pi/F = 2.9 \times 10^{-2}$.

Several sources contribute to this loss. First, using the measurements presented in the previous section, we estimate a lower bound for the round-trip transmission of 5×10^{-5}. However, in general the highest finesse etalon peak is not exactly at the resonance of the PhC, being at most $\mathrm{FSR}_{\mathrm{DM}}/2 = 3$ nm away from it. At this point, the round-trip transmission becomes 2.6×10^{-2}. Second, we expect a round-trip absorption and scattering loss of 6.8×10^{-4}. Finally, some light will be lost due to the finite aperture size of the etalon. Plane-parallel Fabry-Perot cavities are particularly susceptible to this effect [26, 63], and we estimate it to result in a round-trip loss of 2×10^{-3}. Combining these effects we arrive at estimated total round-trip losses between 2.8×10^{-3} and 2.9×10^{-2} (see section 6.5.3 for more details).

Although the maximum finesse measured in our devices fits well to this range, the fact that we generally measure lower values suggests that they are underestimated. Scattering, which has consistently been identified as one of the main loss mechanisms in other PhC membranes [57, 58], could be higher than expected. In addition, these estimates assume that both membranes have the same reflectivity. In both the Low and Mid R samples the reflection drops to zero at the etalon resonances, indicating that the PhC resonances on the front and back membranes are sufficiently well matched in these regimes. However, with increasing reflectivities, mismatches due to fabrication imperfections and small systematic shifts between the individual PhC mirrors become more apparent and lead to smaller dip depths (cf. the High R device in Figure 6.2). In fact, as the reflectivity of the individual membranes increases, the dip depth becomes significantly more sensitive to differences between the two mirrors (see Figure 6.5 in section 6.5.1). This also results in higher round-trip transmission values that can explain the discrepancy between our finesse estimates and measurements.

6.3.2. MECHANICAL CHARACTERIZATION

We determine the mechanical quality factor of the fundamental modes of both single and double membrane devices by performing interferometric ring-down measurements. The mode frequencies are approximately 150 kHz and the difference in frequency between the front and back membranes is typically around 170 Hz. The small difference of around 0.1 % in resonance frequency can be attributed to an irreproducibility in the fabrication process. All devices show unclamped quality factors between 1.2×10^6 and 5.6×10^6. These values are in good agreement with measurements on a similar geometry, which showed quality factors of 4×10^6 [67], indicating that the PhC patterning does not negatively effect their mechanical properties.

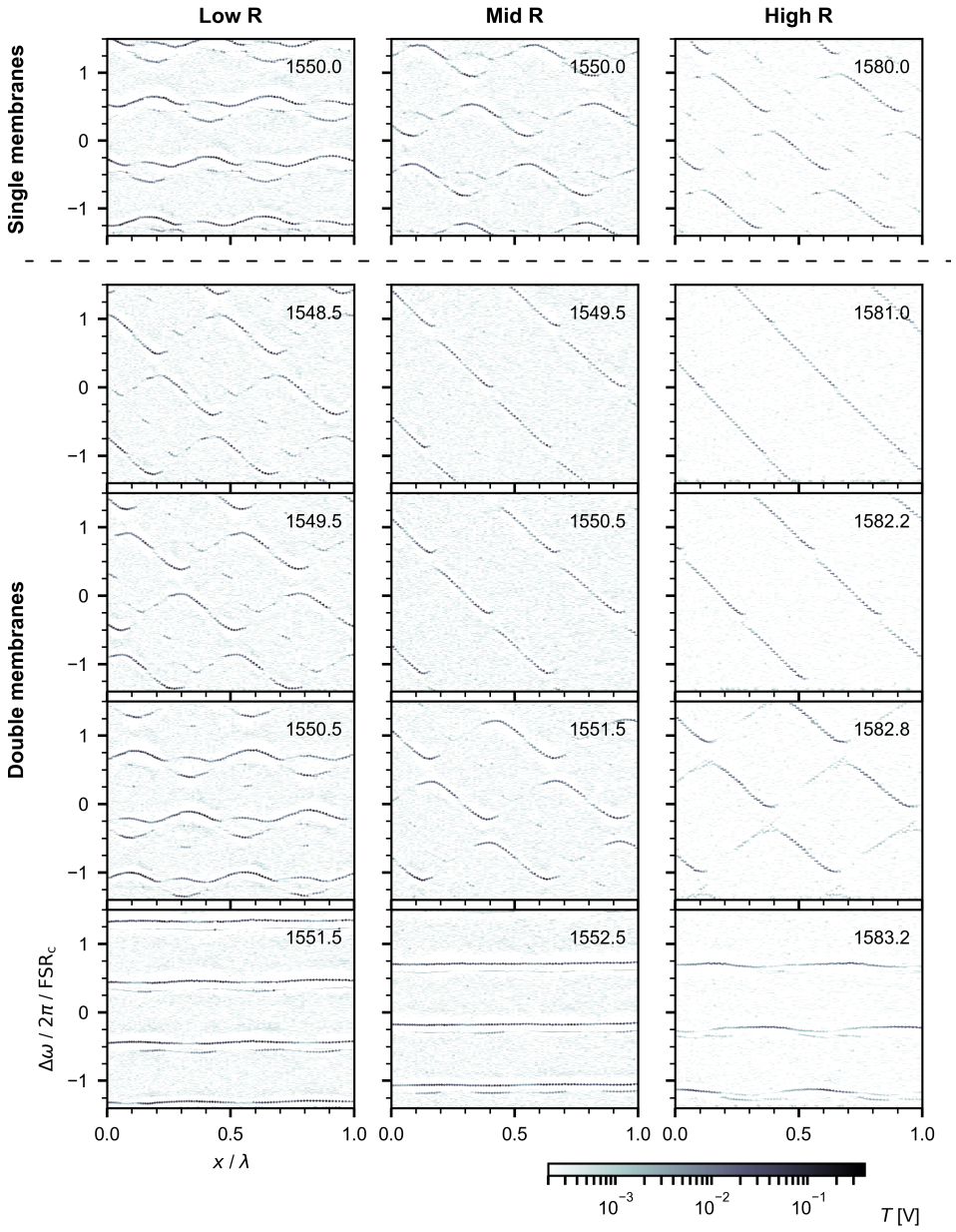

Figure 6.3: Optical cavity transmission T as a function of the frequency shift $\Delta\omega$ of an incident laser and of the displacement x of a mechanical device placed in the middle of the cavity. $\Delta\omega$ is normalized by the cavity free spectral range $\mathrm{FSR_c} = 3.13\,\mathrm{GHz}$ and x by the laser wavelength λ which is indicated on each plot. We measured multiple devices in the middle of the cavity: above the dashed line we study single-membranes and, below it, double-membranes. The type of photonic crystal used in each sample is indicated at the top of the figure. Note that in order to work in a regime with a slow reflectivity change and large dip depth, the High R samples were studied at a wavelength for which $R_\mathrm{m} = 0.76$.

6.3.3. OPTOMECHANICAL CHARACTERIZATION

In order to obtain the optomechanical characteristics of the devices we place them inside an optical cavity. The optical modes of this larger cavity strongly depend on the position of the membranes inside. By measuring the changes in cavity mode frequency ω_c as a function of the device displacement x, we are able to determine the linear optomechanical coupling between the cavity and the device's center-of-mass mechanical modes, which we define as $G \equiv \max\{|\partial\omega_c/\partial x|\}$. The cavity has a free spectral range $\mathrm{FSR_c} = 3.13\,\mathrm{GHz}$ and an empty cavity half-width at half-maximum of $\kappa/2\pi = 550\,\mathrm{kHz}$. We align our tunable laser to the cavity and measure the transmitted light. The laser frequency is then scanned as a function of the device position, which allows us to directly obtain $\omega_c(x)$ and calculate the optomechanical coupling.

Let us first consider the case of a single-membrane, where the cavity modes are affected by the membrane position and reflectivity R_m, according to $\Delta\omega_c/2\pi = \mathrm{FSR}\cdot \arccos(\sqrt{R_m}\cos(4\pi x/\lambda))/\pi$ [14]. The so-called linear coupling regime occurs when a membrane is placed close to $x = \lambda/8 + n\lambda/4, n \in \mathbb{Z}$. Around these points, the cavity frequency changes linearly with the membrane position and the optomechanical coupling is given by

$$\frac{G}{2\pi} = 4\frac{\mathrm{FSR}}{\lambda}\sqrt{R_m}. \tag{6.1}$$

The first row of figure 6.3 shows the cavity transmission as a function of laser frequency shift and displacement of the single-membrane samples. The wavelength at which the measurements were taken is indicated on each plot. The points of high transmission correspond to cavity modes. Because of alignment imperfections between the laser, the cavity and the membranes, in addition to the fundamental cavity mode, we also observe higher order modes, which can be coupled to each other [147]. The fundamental optical mode frequency depends on the membrane position with a periodicity of $x/\lambda = \pi/2$ and the amplitude of the frequency oscillations increases with the membrane reflectivity, as indicated by eq. 6.1. Using these data, we obtain G by numerically calculating $|\partial\omega_c/\partial x|$ and taking its maximum value, which occurs at the positions of linear coupling. The blue data points in figure 6.4 show the single membranes' coupling around a narrow wavelength window obtained through the derivative method or through applying eq. 6.1 to the spectra of fig. 6.2. Within this wavelength range, the reflectivity of each device varies little and therefore G is practically constant. The average measured couplings $G/2\pi$ for the Low, Mid, and High R samples are 3.8(60), 5.7(90), and 7.7(12) GHz/nm, whereas the expected values using eq. 6.1 and $\sqrt{R}$ are 4.5, 5.8 and 6.8 GHz/nm. Despite the large uncertainty, mainly due to the displacement calibration, the results are in good agreement with eq. 6.1.

Finally, we follow the same approach to obtain the coupling rate between the cavity and the COM displacement of the double-membrane chips, schematically represented in fig. 6.1. The crucial difference between single and double-membranes is that the latter's spectra vary more strongly with wavelength. In particular, over one $\mathrm{FSR_{DM}}$, the device reflectivity can quickly change from zero to one (see fig. 6.2). When the reflectivity is low, the COM mode of the device will interact weakly with the external cavity. Correspondingly, at a reflection maximum, the coupling will be higher than that of a device composed of only one membrane. In rows 2 to 5 of fig. 6.3 the measured cavity

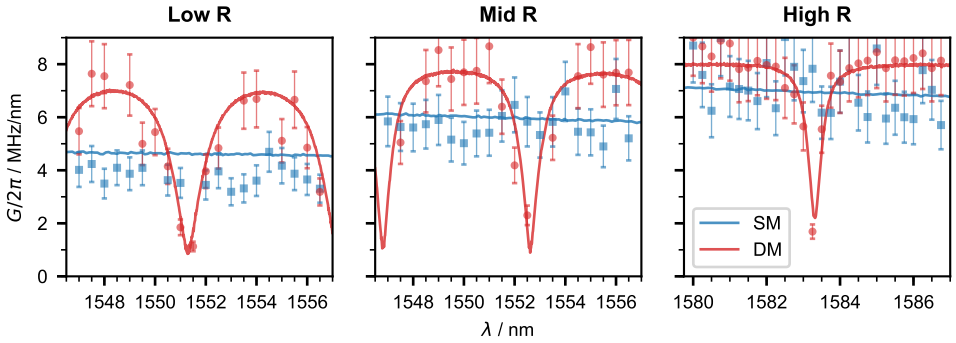

Figure 6.4: Center-of-mass optomechanical coupling $G/2\pi$ as a function of wavelength λ. The points are calculated from the maximum of the derivative of the dispersion data shown in figure 6.3, whereas the lines result from applying equation 6.1 to the reflectivity data on figure 6.2. The blue data are taken from single- and the red from double-membrane devices. The corresponding PhC patterns are indicated on top of each figure, with the wavelength range studied here marked in gray in fig. 6.2. Given our experimental parameters, a single membrane with a reflectivity of 1 is expected to have a coupling of 8 GHz/nm.

dispersion for the three double-membranes studied is shown. We perform these measurements at several wavelengths spanning half a $\mathrm{FSR_{DM}}$, between which the reflectivity varies between its maximum and minimum values. Note that for the High R sample we choose to study a resonance for which $R_\mathrm{m} \sim 0.76$ since for higher R_m the laser fine scanning range becomes similar to the resonance linewidth, and the dip depth decreases, making the coupling oscillations less visible. Row 2 corresponds to the reflectivity maxima. When comparing it with row 1, it becomes clear that the cavity frequency varies more strongly than in the single-membrane case. The data in row 5 are taken close to a transmission maximum where, as discussed, the COM motion has little influence on the cavity frequency. Rows 3 and 4 show wavelengths in between the maximum reflection and transmission of the double-membrane stacks. The extracted COM coupling is plotted in fig. 6.4. As discussed, the coupling oscillates between almost zero and values larger than those of the individual membranes. The oscillation follows the device's spectral response, indicating that the COM coupling of a double-membrane is well described by eq. 6.1, a model derived from the single-membrane case.

6.4. CONCLUSION

In conclusion, we have fabricated and characterized stacks of optomechanical devices that operate in various low to high reflectivity regimes. The devices presented here are patterned onto a single chip without the need for additional bonding steps or micropositioners. Our devices form a flexible platform in which the finesse can be freely tuned. Placing these devices inside an optical cavity allows the direct comparison of membrane-in-the-middle systems in multiple reflectivity regimes, such as proposed in reference [148]. We see an enhancement of the optomechanical coupling rate between the COM motion of the two membranes and the cavity field as a function of reflectivity, when compared to a single membrane system.

More importantly, we can tune the system such that the COM coupling is practi-

cally zero. The theory of the collective motion of optomechanical arrays predicts that at these points the cavity field becomes resonant with the inner cavity and thus couples strongly to the relative motion of the membranes. This is the regime where single-photon strong coupling in an optomechanical system could be achievable [21]. We are currently working on improving the stability of our setup in order to probe these relative motional modes. For devices with large R_m, like the ones presented here, the coupling enhancement of the differential mechanical motion is limited by the ratio $L/2l$ between the length of the optical cavity L and the separation between the membranes l [38]. Given our experimental parameters, this should allow us to observe an enhancement of up to 120. Increasing this value further could be done by replacing the Si substrate by a thin sacrificial layer as the spacer between mirrors, considerably decreasing d to values similar to [144] but keeping the advantages of monolithic fabrication presented here.

Even more interestingly, the single-photon cooperativity scales quadratically with the single-photon coupling strength, which in our case could boost this important figure of merit by 4 orders of magnitude, assuming the mechanical and optical dissipation rates stay the same. For many experiments, coherent control in the strong single-photon coupling regime is not necessary, but reaching cooperativities greater than one is sufficient for performing several quantum protocols [13, 31]. Other interesting experiments could include synchronization of mechanical modes [140], studying exceptional points in optomechanics with independent mechanical systems, as well as superradiance [138, 139] and state transfer between mechanical systems [145]. In addition, our arrays could serve as rigid, stable free-space optical filters with adjustable finesse. The arrays also constitute an optomechanical system by themselves, whose mirrors are both movable and with engineerable optical and mechanical properties. As both mirrors and mechanical resonators are monolithically combined, the system is inherently stable, greatly relaxing the setup complexity of typical free-space optomechanical setups, and making it an ideal platform for simple studies of radiation-pressure effects.

ACKNOWLEDGMENTS

We would like to thank Markus Aspelmeyer and Clemens Schäfermeier for discussions and support. We also acknowledge assistance from the Kavli Nanolab Delft, in particular from Marc Zuiddam, Charles de Boer and Arnold van Run. This project was further supported by the European Research Council (ERC StG Strong-Q, Grant No. 676842), the Foundation for Fundamental Research on Matter (FOM) Projectruimte grants (15PR3210, 16PR1054) and by the Netherlands Organisation for Scientific Research (NWO/OCW), as part of the Frontiers of Nanoscience program and through a Vidi grant (Project No. 680-47-541/994).

6.5. SUPPLEMENTARY INFORMATION

6.5.1. DETAILED FABRICATION, CHALLENGES AND SOLUTIONS

DETAILED FABRICATION

Our devices are fabricated in 200 nm thick stoichiometric SiN deposited via low-pressure chemical-vapor deposition (LPCVD) on a plain 200 µm-thick Si substrate. We then lithographically define a 500 nm thick electron-beam sensitive resist (AR-P 6200.13) in the shape of our photonic crystal trampolines and transfer the pattern into the SiN device layer with a CHF_3/O_2 plasma etch. In the case of our single photonic crystal trampolines the backside of the wafer is then patterned with square openings to fully etch through the entire Si wafer without forming a double membrane array. In the case of fabricating the latter, we first thoroughly strip the remaining electron beam resist with a suitable remover at elevated temperatures (Baker PRS-3000 at 80 °C) to ensure a clean surface after the first pattern transfer step. We then repeat the same procedure of transferring the trampoline pattern into the second device layer while protecting the already patterned front side as to minimize exposure of both device layers to the clean room environment. This cannot fully be avoided as both device layers will get in contact during the spin coating procedure, i.e. with both the spin coater chuck and the hot plate surface during tempering. Despite that fact, we do not see clear negative effects on neither the mechanical nor optical properties of our resonators. After the pattern transfer into both SiN layers, we again clean the chip surfaces thoroughly from any organic compounds. We first use Baker PRS-3000 at 80 °C to remove the remaining electron resist off the surface followed by a hot Piranha solution at 110 °C. To release the trampolines, the chips are briefly rinsed in various water baths and then transferred to a 30 % potassium hydroxide (KOH) solution at 75 °C. The silicon is etched through the entire wafer for about two hours at a rate of 1 µm/min. After the release, a 10 min hydrochloric acid (HCl) etch cleans off KOH residues of the exposed resonators surfaces. We then carefully transfer them into subsequent rinsing baths of water and isopropyl alcohol (IPA) before drying them in a critical point dryer (CPD) to avoid their exposure to viscous forces and surface tension.

FABRICATION YIELD

We have found that by patterning the entire central pad with a PhC, even on its edges, as shown in the zoom-in of figure 6.1c, the fabrication yield increases considerably. Devices with round PhCs as close as 5 µm to the pad edge show either cracks or even fully break. Increasing the PhC diameter such that we cover more of the central pad with etch holes seems to reduce part of the large stress on the membranes which presumably is causing their rupture during release. This allows us to explore a much wider range of possible design parameters with even larger pad sizes, significantly improving on challenges like alignment between both membranes related to finite aperture losses (see section 6.5.3), or using bigger beam waists in an optical cavity.

ALIGNMENT BETWEEN FRONT AND BACK MEMBRANE

We align front and backside using an optical microscope to determine the coordinates of the patterns to be written with respect to one corner of our chips. By using this method,

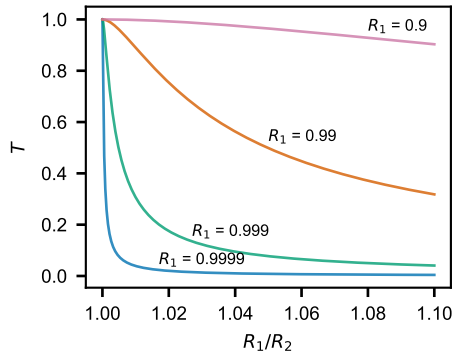

Figure 6.5: Influence of reflectivity mismatches between both mirrors. Plotted is the transmission T versus the ratio of both mirror reflectivities R_1/R_2. For low finesse Fabry-Perot cavities, bigger mismatches do not have as big of an influence on the the transmission as for the high finesse cases.

we introduce uncertainties to the correct coordinates between front and backside, leading to misalignments between 10 µm and 30 µm with good reproducibility, effectively reducing the overlap between both mirrors. This could be significantly improved by using topological alignment markers reaching through the entire chip, e.g. by deep reactive ion etching (DRIE). This would lead to better alignment between both membranes with the drawback of adding additional fabrication steps.

OPERATION IN THE HIGH FINESSE TRANSMISSIVE REGIME

In order to understand the importance of matching the reflectivities between both mirrors, we plot the theoretical transmission T of the Fabry-Perot cavity with respect to the ratio R_1/R_2 of its individual mirror reflectivities (see figure 6.5). The transmission (without losses) follows the following equation for normal incident light

$$T = \frac{(1-R_1)(1-R_2)}{(1-\sqrt{R_1 R_2})^2}.$$

One can see that the transmission only reaches unity for matching mirror reflectivities and drops quicker the higher the finesse of the cavity becomes, i.e. for increasing R_1 and R_2. In the case of $R_1 = 90\,\%$, mismatches of up to 10 % do not cause a big drop in transmission yet (pink curve, see also low and mid R transmission plots in figure 6.2). For very high mirror reflectivities above $R_1 = 99.99\,\%$ even small mismatches between both mirrors already lead to a significant and rapid reduction in transmission (blue curve, figure 6.2).

It is crucial to have good control over the tuning of our PhC resonances in order to account for mismatches between both mirrors induced by fabrication imperfections, especially in high finesse cavities. We therefore fabricated single membranes with various PhC parameters in order to see its influence on the maximum of their resonance λ_{res} (see figure 6.6). We vary their radius r as well as lattice constant a and find a linear behavior around our operating wavelength of 1550 nm. Taking the measured values of the lines

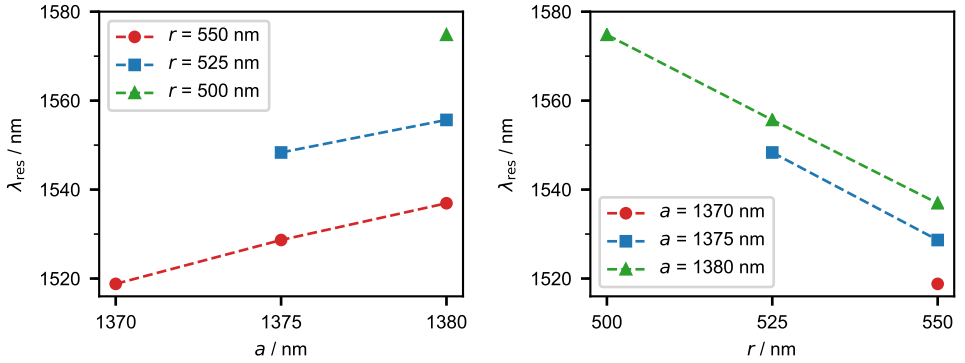

Figure 6.6: Influence of the PhC design parameters on its resonance wavelength λ_{res}. Plotted are measured resonance maxima for varying lattice constants a and radii r. For increasing lattice constants, the maximum of the PhC resonance shifts to higher wavelengths, whereas it decreases for increasing radii.

with three data points, we can determine the slopes to be $\Delta\lambda_{\text{res}} \propto 1.81 \cdot \Delta a$ for a fixed radius of $r = 550\,\text{nm}$, and $\Delta\lambda_{\text{res}} \propto -0.76 \cdot \Delta r$ for a fixed lattice constant of $a = 1380\,\text{nm}$.

In order to test how much the reduced dip depths can be attributed to mismatching mirror reflectivities, we fabricated double membrane arrays with varying PhC design parameters. We keep the devices on one side of the chip fixed while sweeping the resonances on the other side by ± 1.5 nm in their lattice constants a, effectively tuning λ_{res} by more than 5 nm. We found that we could increase the dip depth of the high R array resonances from 1 % to up to 10 %. Further, more finely spaced sweeps of these parameters should allow for even larger dip depths, while operating in a regime of high finesse.

6.5.2. SETUP FOR OPTOMECHANICAL CHARACTERIZATION

To characterize the optomechanical properties of the devices we place them in the center of a rigid optical cavity, composed of two commercial mirrors which are 48.1 mm apart. The mirrors are curved with an equal radius of 25 mm, making a stable cavity with a $\text{FSR}_c = 3.12\,\text{GHz}$, an empty cavity half-width at half-maximum linewidth of 550 kHz and a corresponding finesse of 3000. We estimate the cavity waist to be 49 µm, considerably smaller than the PhC diameter of 300 µm and approximately the same as the one used on the optical characterization setup.

When empty, we align the incident laser to the cavity, achieving a mode matching to the TEM_{00} modes larger than 90 %. By measuring light that is both transmitted and reflected from the cavity and by scanning the laser frequency, previously calibrated using a wavemeter, we obtain the cavity spectrum.

We then position the membrane inside the cavity using a 3-axis piezoelectric stick-slip positioner. This allows us not only to precisely align the PhC membranes to the cavity waist, but also to probe multiple devices on the same chip. The positioner is mounted on top of a stage which enables the alignment of the membranes' tip and tilt in relation to the cavity axis. The x-axis positioner can also be operated in a conventional continuous voltage mode, which lets us displace the membrane by up to 5 um along the cavity axis.

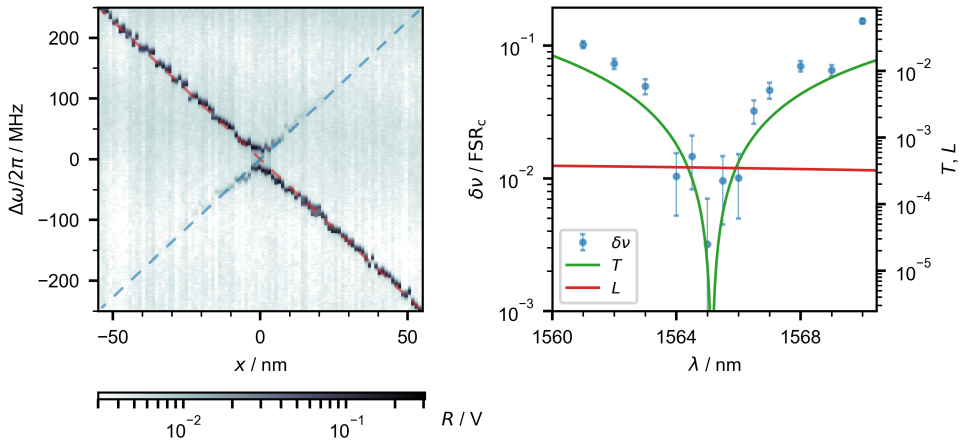

Figure 6.7: Left: Reflection of the optical cavity as a function of laser frequency $\Delta\omega$ and membrane position x at a wavelength of 1566 nm. Here, we study a sample with a PhC resonance at 1565 nm and measure the splitting of the avoided crossing $\delta\nu$. Right: The points indicate the measured $\delta\nu$, normalized by the cavity free spectral range $\mathrm{FSR_C}$, as a function of the laser wavelength, close to the PhC resonance. These data can be converted into a membrane transmission, which is indicated on the right axis. The traces are the result of an S^4 simulation of the transmission (green) and absorption losses (red) of a single PhC membrane with similar geometry as the measured sample and an imaginary part of the refractive index of 1.9×10^{-5}.

Finally, for a given laser wavelength and position we scan the laser frequency and measure the transmitted power. The maxima of the transmission correspond to cavity resonances. We obtain the dispersion maps of fig. 6.3 by repeating this measurement for multiple positions and wavelengths. Due to their low signal to noise ratio, in order to make the plots of fig. 6.3 clearer, we apply a bandpass-pass filter to the data, ensuring it has no influence to the height and width of the resonances.

We would like to point out that on the optical characterization setup, due to the procedure we follow to do coarse wavelength sweeps, the wavelength has an uncertainty of 0.5 nm, while the wavelength on the optomechanical characterization setup is much better defined. To compensate for this mismatch, we use the coupling minima as a reference for the wavelength where the $\sqrt{R}$ minima should occur in fig. 6.4 and shift $\sqrt{R}$ accordingly. To be specific, on that figure, the spectra of the Low, Mid and High R devices were shifted by 0.1, 0.1 and −0.3 nm, respectively.

6.5.3. ESTIMATION OF OPTICAL LOSSES

SINGLE-MEMBRANE MINIMUM TRANSMISSION

To obtain a more accurate estimate of the maximum reflectivity achievable with our PhC membranes, we place a sample with a PhC resonance at 1565 nm in the cavity setup described before. The left plot on figure 6.7 shows the cavity reflection as a function of laser frequency and membrane displacement x. The membrane divides the cavity into two half-cavities whose mode frequencies are a function of membrane displacement x. As x increases, the length of the half-cavity above (below) the membrane increases (decreases), changing the mode frequency as indicated by the dashed red (blue) line. If the

membrane was perfectly reflective, both half-cavity mode frequencies would become degenerate at a particular x. Realistically, the membrane has a non-zero transmission which allows some light to leak between the two half-cavities. This lifts the degeneracy and gives rise to an avoided crossing whose frequency splitting $\delta\nu$ can be used to extract the membrane transmission [57, 58].

We repeat this measurement for multiple wavelengths close to the PhC resonance. The frequency splittings normalized by the free spectral range are plotted as blue circles on the right plot of fig. 6.7. The smallest $\delta\nu/\mathrm{FSR_c}$ measured for this sample was 3.2×10^{-3} at 1565 nm. Using the method of Stambaugh et al. [57], this corresponds to a a minimum PhC transmission of 2.5×10^{-5}.

DOUBLE MEMBRANE TRANSMISSION LOSS

In each round-trip, some light inside the double membrane etalon is transmitted through the PhC mirrors. If both membranes had exactly the same PhC resonance wavelength and if the highest finesse peak was exactly at the same wavelength as that resonance, this would result in a round-trip transmission of 5×10^{-5}. However, the double-membrane peak is not, in general, at the PhC resonance. For a double-membrane with similar PhC resonances, the peak can be, at most, 3 nm (approximately $\mathrm{FSR_{DM}}/2$) away from the PhC resonance. According to fig. 6.7, this sets an upper boundary to the round-trip transmission of 2.6×10^{-2}.

MATERIAL LOSSES

When light interacts with the SiN layer, some of it will be absorbed by the material or scattered away due to fabrication imperfections. To estimate the magnitude of these effects, we use S^4 to simulate the reflection and transmission through a PhC with similar parameters to those of figure 6.7. We have considered the material to have an imaginary part of the refractive index of 1.9×10^{-5} [57], which accounts for not only absorption but also other loss mechanisms such as scattering [58], and we calculate the losses as $L=1-R-T$, where R is the reflection and T the transmission coefficients. The simulation results are shown on the lower part of fig. 6.7. We see that the measured transmission follows the simulation quite well. Within this wavelength range, the losses are approximately constant and have a value of 3.5×10^{-4}.

FINITE APERTURE LOSS

Any Fabry-Perot inteferometer with a finite aperture will lose some of the light through diffraction at the mirror edges [26, 63]. These losses are higher for smaller mirrors and for increasing cavity stability parameter. In particular, a plane-parallel Fabry-Perot cavity has the highest stability parameter ($g=1$), which makes it particularly susceptible to finite aperture losses.

To estimate these, one can calculate the cavity Fresnel number $N=a^2/L\lambda$, where a is the mirror radius and L is the cavity length, and obtain the estimated losses per cavity round-trip from tables in literature [26, 63]. Given a mirror diameter of 260 µm, the Fresnel number of our devices is 54, which corresponds to a loss per round-trip of 2×10^{-3}.

Notice that this effect could be directly mitigated either by making the PhC membranes larger, or by controlling the wavefront of the field with one of the PhC, effectively

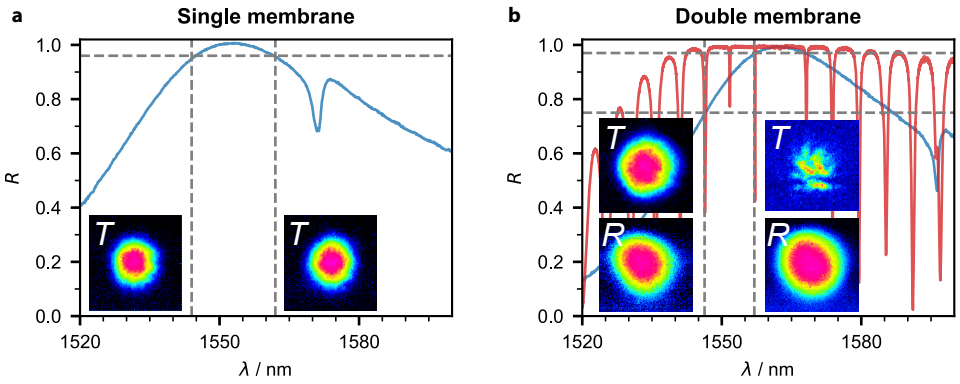

Figure 6.8: Shown are the reflection spectra, together with the transmitted (T) and reflected (R) beam mode profiles of single **a** and double membranes **b**. The dashed lines indicate the reflectivity and wavelength at which the mode profiles were measured.

realizing a focusing mirror [117]. This would reduce the stability parameter of the cavity, making it less susceptible to finite aperture losses.

TOTAL LOSSES

Taking into account the previous results, we can estimate the total losses of the double-membrane array if its highest finesse peak is at the resonance wavelength of the PhC or if it is 3 nm away from it. Using the finite aperture loss, the measured transmissions and the simulated material losses, we reach round-trip total losses of 2.8×10^{-3} and 2.9×10^{-2}, corresponding to cavity finesse values of 2243 and 217. The lower bound of this range is in good agreement with the maximum finesse we measure in our devices of about 220. However, most of our samples show maximum finesses which are approximately a factor of 5 smaller. This could be due to underestimations of scattering and diffraction losses, or due to additional absorption by material residues on the SiN layers or to the mismatch between the PhC resonances of both membranes.

MODE PROFILE ANALYSIS

The reflection and transmission beam profiles can also help in understanding the behavior of our devices. We install flip mirrors in our setup which can send the optical beams to an IR-sensitive camera and record the beam profiles for single and double membranes, shown in figure 6.8a and b, respectively.

For the single membranes we obtain the beam profiles slightly detuned from the maximal reflectivity, around 95 %, as otherwise the transmission is below the sensitivity of the camera. The measured modes have an overlap of approx. 83 % with a Gaussian distribution, highlighting that the PhC structures distort the transmitted optical beams only slightly.

In figure 6.8b we plot the reflection spectrum of a double membrane (red) whose individual membranes have a spectrum similar to the one shown in blue. The resonance with the highest finesse occurs at 1562 nm, however its low dip depth makes the mode difficult to measure with our camera. The adjacent resonance at 1557 nm shows

the second highest finesse ($F = 144$), corresponding to single membrane reflectivities of around 97 %. Here we are able to measure the beam profiles for the transmitted and reflected light. While the reflection is mostly unaffected, the transmitted beam appears distorted. As the single membrane transmission does not show such behavior, we suspect the distortion results partly from scattering losses, as described in section 6.5.3. This loss mechanism becomes more dominant as the number of cavity round-trips, i.e. the finesse, increases. Indeed, for the resonance at 1546 nm with a lower finesse of only 21, corresponding to a single element reflectivity of 75 %, the transmitted and reflected beam profiles have an overlap with a Gaussian distribution of more than 84 %.

In addition, we would also like to note that the tip/tilt alignment becomes more important in double membrane arrays with high finesse, since the incident beam has to be properly mode matched to the cavity. This is further complicated by the plane-parallel geometry of our PhC cavities and could therefore be another main contribution to the observed mode distortion. This problem could be ameliorated by making one of the PhC mirrors a so-called *focusing* PhC [117], which can decrease the cavity stability parameter, making the mode matching and alignment easier.

7

Conclusion and Outlook

The aim of this thesis was to engineer systems based on SiN tethered membranes with large mechanical quality factors and optomechanical coupling rates. Multiple issues related to the study of optomechanical arrays of this type of membranes inside optical cavities were addressed but plenty of new questions were also brought to light. This chapter outlines some of those issues, as well as ideas for future experiments.

High-Q_m SiN mechanical resonators

Chapter 4 showed that tethered SiN membranes can have mechanical properties good enough to be cooled down from room temperature to their ground state using optomechanical cooling. For this, the membrane thickness needs to be as small as possible, whereas the chip thickness must be large. As the thickness of SiN films decrease, the stress approaches this material's ultimate yield strength, making the devices very fragile and harder to fabricate. At 25 nm-thickness, even light collisions of the samples against glass beakers during fabrication can harm the devices' mechanical quality factor. The yield is thus considerably lower. As to the requirement for thicker substrates, this increases the KOH-etching time and demands additional steps to ensure short SiN overhangs, a crucial factor in achieving a high Q_m, making the device more susceptible to failure during fabrication.

More recently, other works have been published in which mechanical resonators with frequencies close to our tethered membranes had equivalent or even higher $f_m \times Q_m$ products [149, 150]. In these, to reduce clamping losses from the resonators to the substrates, the authors design a *phononic shield* which greatly decreases the curvature, and thus bending losses, of some mechanical modes and localizes these far from the clamping points, reducing radiative losses. In this way they are able to achieve $f_m \times Q_m$ up to 1.1×10^{15} Hz. However, this is achievable for higher order mechanical modes and therefore it is questionable how useful this method is for ground state cooling. Therefore, *strain engineering*, the method used primarily in our devices, still seems to be the most promising approach to increase the $f_m \times Q_m$ of fundamental mechanical modes at the MHz-frequency range for ground state cooling from room temperature.

Another advantage of devices with phononic shields is that they are reportedly less sensitive to the way in which the chip is attached to the setup. This is a considerable challenge in membrane-in-the-middle setups, since to ensure good mechanical stability the chip must be mounted tightly to some sort of holder. This in turn modifies the stress distribution of the device and can increase radiation losses [110]. The devices studied in chapter 4 were simply lying on a translation stage and not tightly mounted to it. We opted for this approach because we were already aware that mounting brings a lot of inconsistency when it comes to the mechanical decay rate. Our devices could in principle be made insensitive to these losses by making a phononic shield on the Si substrate around the device, like demonstrated in [151], even though the unit cell, and consequently the chip size, would be considerably larger due to our low mechanical frequency.

As pointed out in chapter 4 and measured in [112], these high-Q_m resonators have force sensitivities of tens of aN/$\sqrt{\text{Hz}}$, making them promising candidates as detectors for applications that require high sensitivity. Following up on this, a few groups are now studying concrete applications of tethered membranes as sensors. As a notable example, a tethered membrane can be functionalized with a magnet in order to build a magnetic resonance force microscope based on optomechanical detection with a very low sensitivity [152]. Another field were tethered membranes could result in direct improvements in performance is in particle detectors. Some rely on the interaction of particles with membranes, measuring their displacement using optomechanics techniques, such as CERN's KWISP [153]. In such a detector, using a trampoline membrane could greatly improve the machine's sensitivity and noise performance. Indeed, functionalizing and exploiting SiN tethered membranes for sensing applications might be one of the most promising avenues of research of this type of devices.

7

LARGE-AREA, SUSPENDED PHC MIRRORS

To obtain strong light-matter interactions, the reflectivity of the mechanical resonators must be large, for example by patterning photonic crystals on the membranes. Decreasing the thickness of SiN membranes makes it more challenging to achieve high reflectivities, since, as laid out in chapter 5, the PhC resonances become narrower and the device response is more sensitive to the wavefront of the incident beam. For the purposes of optomechanical arrays, these results establish clear trade-offs between PhC reflectivity and mechanical properties: thinner devices can have low mechanical damping, but to achieve large reflectivities the membrane must be widened, decreasing the mechanical frequency and, thus, $f_m \times Q_m$. Chapter 4 proposes inverse-PhC patterns of thick SiN cylinders supported by the thin membrane pad as a solution for this issue. On top of an additional lithography step, this type of PhC requires etching down the SiN film with reactive ion etching. It is not known if this process can harm the film surface and, consequently, the mechanical dissipation rate.

The greatest impact of the results of chapter 5 will probably be in fields unrelated to optomechanics, namely in the manufacture of thin optical elements. The development of extremely thin PhC mirrors and lenses is promising, and the possibility of engineering their response to frequency, polarization, and angle of incidence opens the door to a large array of applications. From miniaturizing the pixel size of screens [154] to coatings that protect airplanes from laser attacks [155], photonic crystals and metamateri-

als are increasingly finding their way towards more advanced technology development stages. The large area PhC mirrors presented in this work could find niche applications where properties such as very high reflectivity, low material absorption or high mechanical quality factor are needed. Excitingly, one can envision harnessing the suspended nature of these devices to decrease their displacement noise or control their position, either globally or locally, as a deformable mirror.

One application where large-area, suspended PhC mirrors made of SiN could prosper is in low-mass lightsails, a topic which partially motivated this work in the first place. SiN PhC mirrors meet many of the requirements of lightsails for projects such as the Starshot Breakthrough Initiative [130] of broadband low optical losses, high emissivity, high reflectivity and low mass [156]. But several challenges are still open. Such lightsails require areas of about $10\,m^2$, a large step from what we demonstrated. This would certainly require combining multiple mirror wafers together. Since the SiN mirrors require a supporting Si substrate frame to sustain the tensile stress, the total sail mass would necessarily be much larger than the desired 1 g. It is also not clear how these membranes with large tensile stress would behave with collisions with space dust. Among other difficulties, the extreme requirements of the Starshot project seem unrealistic. Even so, given all its advantages, SiN PhC mirrors are strong contenders for Starshot's sails.

Optomechanical arrays of two high reflectivity membranes

Our work on optomechanical arrays happens during an exciting time in which multiple groups are starting to place considerable efforts towards observing enhanced coupling using this platform. To this day there have only been two other experimental reports which study two membranes in the middle of a cavity [39, 157]. In both, the distance between the membranes can be controlled with piezoelectric actuators, since the devices sit on separate chips. The authors can thus study the optomechanical coupling strength between a cavity and the distance between two unpatterned SiN square membranes.

However, having to control the position of both membranes complexifies the setup considerably. This is a particularly serious consideration once the reflectivity of the membranes increases. Indeed, in one of the cited works, the authors were able to lock the cavity with two membranes in the middle but they had to operate in a regime of low coupling strength in order to avoid instability of the cavity locking feedback loop [39]. In this regard, placing the membranes on the same chip removes some sources of low frequency mechanical noise and allows the feedback loop to be stable over a broader range of parameters.

Fabricating the membranes on the same chip brings other advantages. First, if small membranes such as the ones studied throughout this thesis are used, the method presented in chapter 6 provides a relatively easy way to align the membranes to each other. Furthermore, the parallelism between membranes, which can be a serious source of optical losses [39], is set by that of the substrate, which is typically better than machined parts. In addition, such a double-membrane chip can be used as an optomechanical system in itself, which allows for the realization of optomechanical experiments without the need for complex cavity setups.

Of course with the monolithic-array approach one loses the flexibility of directly controlling the distance between membranes. In this case, the regime of enhanced coupling

can only be reached by tuning the laser wavelength to that of a transmission maximum of the membrane stack. If this is not within reach of a fixed frequency laser, one must instead use tunable lasers. These have typically much larger phase noise which, once again, increase the demands of the feedback loop. However, it should be possible to modify the PhC pattern to alter the phase shift acquired by light transmitted by each membrane and, in this way, apply an offset to the stack's spectrum.

We have estimated that for the parameters of our setup and devices we could potentially observe a coupling enhancement of 120. To go beyond this, one must either increase the cavity length, which comes at the expense of mechanical stability of the setup, or decrease the spacing between membranes. With the current method, this can only be achieved by using thinner chips, which are much more fragile and therefore difficult to handle during manufacturing. Therefore, to move forward, a different approach is needed. One possibility is to bond two square membranes from different chips together, such as described in [144]. This process has demonstrated to allow for membrane distances as short as 8.5 µm. However, it requires careful alignment of the membranes in relation to each other and between their planes, to guarantee parallelism. A promising alternative is to use stacks of crystalline films, such as InGaP, separated by sacrificial layers of AlGaAs. Using a single lithography step, one could obtain a series of mechanical resonators (at the InGaP layers) with very controlled spacings between them, set by the sacrificial layers. This method would also allow for more than two membranes. Although promising, the difficulty seems to reside in successfully fabricating such devices, which are much less robust than SiN. Also, the mechanical properties of membranes made out of such crystalline films have not proven to be able to surpass those of SiN, making it hard to envision such a system having a high optomechanical coupling and low mechanical dissipation simultaneously.

An important open question pertains to the optical losses of double-PhC-membrane stacks. The estimations given on section 6.5.3 do not fully explain why stacks with a higher finesse were not achieved which suggests there are other loss mechanisms at play that we did not consider. For example, non-uniformities or roughness in the mirror surfaces of plane-parallel Fabry-Perots act as scattering elements and lead to serious losses [36]. Cavities with curved mirrors are less susceptible to this issue since they partially recollect scattered light [112, 158]. For this reason, this loss source might not be appreciable when studying a single membrane in the middle of the cavity to obtain its total losses. One indication that surface roughness plays a role in limiting the losses in our devices is in the measured mode profiles shown in section 6.5.3. There we observed that the transmission of higher finesse peaks becomes deformed, which could be explained by a scattering process that makes the beam lose its Gaussian distribution. We know that scattering from surface roughness is one of the dominant loss mechanisms in micro and nanophotonic cavities [159], so it can also be a limiting factor of our PhC optomechanical arrays.

Future experiments should aim at identifying all loss sources and assessing their impact in the context of optomechanical arrays. Similarly, it is important to better define requirements regarding the double-membrane's dip depth and mechanical properties, in particular how relevant the frequency difference between the two membranes is.

Final considerations

Although much effort has been placed in understanding theoretically the effect of the motion of the membrane arrays on the cavity frequency, this was done from a static perspective. We still lack a better understanding of what happens to the mechanical modes once they are coupled through the light field. Are there minimum requirements in the field strength for the membranes to couple strongly enough and to observe the splitting between the center-of-mass and relative motional modes clearly? In other works, what form does the coupling strength between the membranes take? Solving this question will help experimentalists progress more efficiently in the lab.

Going beyond arrays of two mechanical resonators is also an interesting challenge. As mentioned before, one option is to use stacks of thin-films with sacrificial spacer layers, but the material difficulties here are large. An alternative relies on deep-etching technology to pattern arrays of mechanical elements into thick Si chips. One could think of fabricating closely spaced vertical cantilevers which would constitute an array of mechanical elements and whose spacing can be lithographically defined. The cantilevers could be made more reflective by patterning them as a grating. Even more exciting would be to make an optomechanical array system in an integrated photonic circuit. However, it is hard to envision how such a system would look like.

Finally, the high-reflectivity PhC membranes presented in this work could be exploited for studies of quadratic optomechanical coupling. The membrane-in-the-middle platform is one of the only optomechanical systems that allows easy access to this regime which, as mentioned in section 2.3.3, scales favorably with the membrane reflectivity. Given the large reflectivities we measured on single membranes, it is worth exploring what experiments are interesting to perform.

The next few years will bring exciting results to the field of cavity optomechanics. Considering all their potential, PhC membranes will certainly play an important role in *making light jump*.

REFERENCES

[1] The LIGO Scientific Collaboration, *Advanced ligo,* Class. Quantum Grav. **32**, 074001 (2015).

[2] The ET science team, *Einstein gravitational wave Telescope – Conceptual Design Study,* (2011).

[3] The KAGRA Collaboration, *Interferometer design of the kagra gravitational wave detector,* Phys. Rev. D **88**, 043007 (2013).

[4] K. Somiya, *Detector configuration of KAGRA -– the Japanese cryogenic gravitational-wave detector,* Class. Quantum Grav. **29**, 124007 (2012).

[5] The LIGO Scientific Collaboration and Virgo Collaboration, *Observation of gravitational waves from a binary black hole merger,* Phys. Rev. Lett. **116**, 061102 (2016).

[6] Nobel Media AB, *Press release: The Nobel Prize in Physics 2017,* `https://www.nobelprize.org/prizes/physics/2017/press-release/`, accessed in July 2017.

[7] D. G. Blair, L. Ju, and H. Peng, *Vibration isolation for gravitational wave detection,* Classical and Quantum Gravity **10**, 2407 (1993).

[8] LIGO Scientific Collaboration, *Seismic isolation of advanced LIGO: Review of strategy, instrumentation and performance,* Classical and Quantum Gravity **32**, 185003 (2015).

[9] R. Loudon, *The Quantum Theory of Light* (OUP Oxford, 2000).

[10] A. Ashkin and J. M. Dziedzic, *Feedback stabilization of optically levitated particles,* Applied Physics Letters **30**, 202 (1977).

[11] P.-F. Cohadon, A. Heidmann, and M. Pinard, *Cooling of a mirror by radiation pressure,* Phys. Rev. Lett. **83**, 3174 (1999).

[12] LIGO Scientific Collaboration, *Observation of a kilogram-scale oscillator near its quantum ground state,* New Journal of Physics **11**, 073032 (2009).

[13] M. Aspelmeyer, T. J. Kippenberg, and F. Marquardt, *Cavity optomechanics,* Rev. Mod. Phys. **86**, 1391 (2014).

[14] J. Thompson, B. Zwickl, A. Jayich, F. Marquardt, S. Girvin, and J. Harris, *Strong dispersive coupling of a high-finesse cavity to a micromechanical membrane,* Nature **452**, 72 (2008).

[15] M. Eichenfield, J. Chan, R. M. Camacho, K. J. Vahala, and O. Painter, *Optomechanical crystals,* Nature **462**, 78 (2009).

[16] R. Riedinger, S. Hong, R. A. Norte, J. A. Slater, J. Shang, A. G. Krause, V. Anant, M. Aspelmeyer, and S. Gröblacher, *Non-classical correlations between single photons and phonons from a mechanical oscillator,* Nature **530**, 313 (2016).

[17] S. Bose, K. Jacobs, and P. L. Knight, *Scheme to probe the decoherence of a macroscopic object,* Phys. Rev. A **59**, 3204 (1999).

[18] J. Bochmann, A. Vainsencher, D. D. Awschalom, and A. N. Cleland, *Nanomechanical coupling between microwave and optical photons,* Nature Physics **9**, 712 EP (2013).

[19] J. Chan, T. P. M. Alegre, A. H. Safavi-Naeini, J. T. Hill, A. Krause, S. Gröblacher, M. Aspelmeyer, and O. Painter, *Laser cooling of a nanomechanical oscillator into its quantum ground state,* Nature **478**, 89 (2011).

[20] A. H. Safavi-Naeini, T. P. M. Alegre, M. Winger, and O. Painter, *Optomechanics in an ultrahigh-Q two-dimensional photonic crystal cavity,* Appl. Phys. Lett. **97**, 181106 (2010).

[21] A. Xuereb, C. Genes, and A. Dantan, *Strong coupling and long-range collective interactions in optomechanical arrays,* Phys. Rev. Lett. **109**, 223601 (2012).

[22] D. J. Wilson, *Cavity optomechanics with high-stress silicon nitride films*, Ph.D. thesis, California Institute of Technology (2012).

[23] H.-A. Bachor and T. C. Ralph, *A Guide to Experiments in Quantum Optics*, 2nd ed. (Wiley-VCH, 2004).

[24] P. R. Saulson, *Thermal noise in mechanical experiments,* Phys. Rev. D **42**, 2437 (1990).

[25] A. Yariv and P. Yeh, *Photonics: Optical Electronics in Modern Communications*, Oxford series in electrical and computer engineering (Oxford University Press, 2007).

[26] O. Svelto, *Principles of Lasers* (Springer US, 2010).

[27] C. R. Locke, D. Stuart, E. N. Ivanov, and A. N. Luiten, *A simple technique for accurate and complete characterisation of a fabry-perot cavity,* Opt. Express **17**, 21935 (2009).

[28] W. Bowen and G. Milburn, *Quantum Optomechanics* (Taylor & Francis, 2015).

[29] A. Nunnenkamp, K. Børkje, and S. M. Girvin, *Single-photon optomechanics,* Phys. Rev. Lett. **107**, 063602 (2011).

[30] F. Brennecke, S. Ritter, T. Donner, and T. Esslinger, *Cavity optomechanics with a bose-einstein condensate,* Science **322**, 235 (2008).

[31] R. Leijssen, G. R. La Gala, L. Freisem, J. T. Muhonen, and E. Verhagen, *Nonlinear cavity optomechanics with nanomechanical thermal fluctuations,* Nature Communications **8**, ncomms16024 (2017).

[32] M. Bhattacharya, H. Uys, and P. Meystre, *Optomechanical trapping and cooling of partially reflective mirrors,* Phys. Rev. A **77**, 033819 (2008).

[33] M. Aspelmeyer, T. Kippenberg, and F. Marquardt, *Cavity Optomechanics: Nano- and Micromechanical Resonators Interacting with Light*, Quantum Science and Technology (Springer Berlin Heidelberg, 2014).

[34] I. H. Deutsch, R. J. C. Spreeuw, S. L. Rolston, and W. D. Phillips, *Photonic band gaps in optical lattices,* Phys. Rev. A **52**, 1394 (1995).

[35] A. Xuereb, P. Domokos, J. Asbóth, P. Horak, and T. Freegarde, *Scattering theory of cooling and heating in optomechanical systems,* Phys. Rev. A **79**, 053810 (2009).

[36] G. Brooker, *Modern Classical Optics* (OUP Oxford, 2003).

[37] A. Jayich, J. Sankey, B. Zwickl, C. Yang, J. Thompson, S. Girvin, A. Clerk, F. Marquardt, and J. Harris, *Dispersive optomechanics: a membrane inside a cavity,* New J. Phys. **10**, 095008 (2008).

[38] J. Li, A. Xuereb, N. Malossi, and D. Vitali, *Cavity mode frequencies and strong optomechanical coupling in two-membrane cavity optomechanics,* J. Opt. **18**, 084001 (2016).

[39] P. Piergentili, L. Catalini, M. Bawaj, S. Zippilli, N. Malossi, R. Natali, D. Vitali, and G. D. Giuseppe, *Two-membrane cavity optomechanics,* New J. Phys. **20**, 083024 (2018).

[40] N. E. Flowers-Jacobs, S. W. Hoch, J. C. Sankey, A. Kashkanova, A. M. Jayich, C. Deutsch, J. Reichel, and J. G. E. Harris, *Fiber-cavity-based optomechanical device,* Applied Physics Letters **101**, 221109 (2012).

[41] A. Xuereb, C. Genes, and A. Dantan, *Collectively enhanced optomechanical coupling in periodic arrays of scatterers*, Phys. Rev. A **88**, 053803 (2013).

[42] B. Nair, A. Xuereb, and A. Dantan, *Cavity optomechanics with arrays of thick dielectric membranes*, Phys. Rev. A **94**, 053812 (2016).

[43] K. Luke, Y. Okawachi, M. R. E. Lamont, A. L. Gaeta, and M. Lipson, *Broadband mid-infrared frequency comb generation in a si3n4 microresonator*, Opt. Lett. **40**, 4823 (2015).

[44] M. Born and E. Wolf, *Principles of Optics*, 6th ed. (Pergamon Press, 1986).

[45] M. Kanskar, P. Paddon, V. Pacradouni, R. Morin, A. Busch, J. F. Young, S. R. Johnson, J. MacKenzie, and T. Tiedje, *Observation of leaky slab modes in an air-bridged semiconductor waveguide with a two-dimensional photonic lattice*, Appl. Phys. Lett. **70**, 1438 (1997).

[46] S. Fan, P. R. Villeneuve, J. D. Joannopoulos, and E. F. Schubert, *High extraction efficiency of spontaneous emission from slabs of photonic crystals*, Phys. Rev. Lett. **78**, 3294 (1997).

[47] P. L. Gourley, J. R. Wendt, G. A. Vawter, T. M. Brennan, and B. E. Hammons, *Optical properties of two-dimensional photonic lattices fabricated as honeycomb nanostructures in compound semiconductors*, Applied Physics Letters **64**, 687 (1994).

[48] S. Fan and J. D. Joannopoulos, *Analysis of guided resonances in photonic crystal slabs*, Phys. Rev. B **65**, 235112 (2002).

[49] Lumerical Inc., *FDTD Solutions*, `http://www.lumerical.com/tcad-products/fdtd/`, accessed in January 2019.

[50] V. Liu and S. Fan, *S^4 : A free electromagnetic solver for layered periodic structures*, Comput. Phys. Commun. **183**, 2233 (2012).

[51] C. Gärtner, Ph.D. thesis, University of Vienna (2019).

[52] AMMT GmbH, *Wet Etching: Single Chip*, `https://www.ammt.com/products/wet-etching/single-chip/`, accessed in February 2019.

[53] D. T. Smithey, M. Beck, M. G. Raymer, and A. Faridani, *Measurement of the wigner distribution and the density matrix of a light mode using optical homodyne tomography: Application to squeezed states and the vacuum*, Phys. Rev. Lett. **70**, 1244 (1993).

[54] C. Schäfermeier, U. Andersen, and A. Huck, *Quantum enhanced optical sensing*, Ph.D. thesis, Technical University of Denmark (2016).

[55] S. Gröblacher, *Quantum opto-mechanics with micromirrors: combining nano-mechanics with quantum optics*, Ph.D. thesis, University of Vienna (2010).

[56] J. P. Moura, *Fiber Stretcher*, `https://github.com/GroeblacherLab/FiberStretcher`, accessed in February 2019.

[57] C. Stambaugh, H. Xu, U. Kemiktarak, J. Taylor, and J. Lawall, *From membrane-in-the-middle to mirror-in-the-middle with a high-reflectivity sub-wavelength grating*, Annalen der Physik **527**, 81 (2015).

[58] X. Chen, C. Chardin, K. Makles, C. Caër, S. Chua, R. Braive, I. Robert-Philip, T. Briant, P.-F. Cohadon, A. Heidmann, T. Jacqmin, and S. Deléglise, *High-finesse fabry-perot cavities with bidimensional si_3n_4 photonic-crystal slabs*, Light Sci. Appl. **6**, e16190 (2017).

[59] W. Haaxman, *Characterization of suspended photonic crystal membrane arrays*, Master's thesis, Delft University of Technology (2018).

[60] K. Higuma, S. Oikawa, Y. Hashimoto, H. Nagata, and M. Izutsu, *X-cut lithium niobate optical single-sideband modulator*, Electronics Letters **37**, 515 (2001).

[61] B. Culshaw and M. G. F. Wilson, *Integrated optic frequency shifter modulator,* Electronics Letters **17**, 135 (1981).

[62] M. Izutsu, S. Shikama, and T. Sueta, *Integrated optical ssb modulator/frequency shifter,* IEEE Journal of Quantum Electronics **17**, 2225 (1981).

[63] A. Siegman, *Lasers* (University Science Books, 1986).

[64] K. T. Knupfer, *Improving the stability of a membrane-in-the-middle setup for cavity optomechanics,* Master's thesis, Delft University of Technology (2019).

[65] R. W. P. Drever, J. L. Hall, F. V. Kowalski, J. Hough, G. M. Ford, A. J. Munley, and H. Ward, *Laser phase and frequency stabilization using an optical resonator,* Appl. Phys. B **31**, 97 (1983).

[66] E. D. Black, *An introduction to Pound-Drever-Hall laser frequency stabilization,* Amer. Jour. of Phys. **69**, 79 (2001).

[67] R. A. Norte, J. P. Moura, and S. Gröblacher, *Mechanical resonators for quantum optomechanics experiments at room temperature,* Phys. Rev. Lett. **116**, 147202 (2016).

[68] J. D. Teufel, T. Donner, D. Li, J. W. Harlow, M. S. Allman, K. Cicak, A. J. Sirois, J. D. Whittaker, K. W. Lehnert, and R. W. Simmonds, *Sideband cooling of micromechanical motion to the quantum ground state,* Nature **475**, 359 (2011).

[69] A. D. O'Connell, M. Hofheinz, M. Ansmann, R. C. Bialczak, M. Lenander, E. Lucero, M. Neeley, D. Sank, H. Wang, M. Weides, J. Wenner, J. M. Martinis, and A. N. Cleland, *Quantum ground state and single-phonon control of a mechanical resonator,* Nature **464**, 697 (2010).

[70] T. Palomaki, J. Teufel, R. Simmonds, and K. Lehnert, *Entangling mechanical motion with microwave fields,* Science **342**, 710 (2013).

[71] A. H. Safavi-Naeini, S. Gröblacher, J. T. Hill, J. Chan, M. Aspelmeyer, and O. Painter, *Squeezed light from a silicon micromechanical resonator,* Nature **500**, 185 (2013).

[72] T. P. Purdy, P.-L. Yu, R. W. Peterson, N. S. Kampel, and C. A. Regal, *Strong optomechanical squeezing of light,* Phys. Rev. X **3**, 031012 (2013).

[73] E. E. Wollman, C. Lei, A. Weinstein, J. Suh, A. Kronwald, F. Marquardt, A. Clerk, and K. Schwab, *Quantum squeezing of motion in a mechanical resonator,* Science **349**, 952 (2015).

[74] J.-M. Pirkkalainen, E. Damskägg, M. Brandt, F. Massel, and M. A. Sillanpää, *Squeezing of quantum noise of motion in a micromechanical resonator,* Phys. Rev. Lett. **115**, 243601 (2015).

[75] F. Lecocq, J. B. Clark, R. W. Simmonds, J. Aumentado, and J. D. Teufel, *Quantum nondemolition measurement of a nonclassical state of a massive object,* Phys. Rev. X **5**, 041037 (2015).

[76] P. Treutlein, D. Hunger, S. Camerer, T. W. Hänsch, and J. Reichel, *Bose-einstein condensate coupled to a nanomechanical resonator on an atom chip,* Phys. Rev. Lett. **99**, 140403 (2007).

[77] K. Hammerer, M. Wallquist, C. Genes, M. Ludwig, F. Marquardt, P. Treutlein, P. Zoller, J. Ye, and H. J. Kimble, *Strong coupling of a mechanical oscillator and a single atom,* Phys. Rev. Lett. **103**, 063005 (2009).

[78] A. G. Krause, M. Winger, T. D. Blasius, Q. Lin, and O. Painter, *A high-resolution microchip optomechanical accelerometer,* Nature Photon. **6**, 768 (2012).

[79] A. Jöckel, A. Faber, T. Kampschulte, M. Korppi, M. T. Rakher, and P. Treutlein, *Sympathetic cooling of a membrane oscillator in a hybrid mechanical–atomic system,* Nature Nanotech. **10**, 55 (2014).

[80] M. Yuan, V. Singh, Y. M. Blanter, and G. A. Steele, *Large cooperativity and microkelvin cooling with a three-dimensional optomechanical cavity,* Nature Commun. **6**, 8491 (2015).

[81] R. Andrews, R. Peterson, T. Purdy, K. Cicak, R. Simmonds, C. Regal, and K. Lehnert, *Bidirectional and efficient conversion between microwave and optical light,* Nature Phys. **10**, 321 (2014).

[82] F. Marquardt, J. P. Chen, A. A. Clerk, and S. M. Girvin, *Quantum theory of cavity-assisted sideband cooling of mechanical motion,* Phys. Rev. Lett. **99**, 093902 (2007).

[83] D. J. Wilson, C. A. Regal, S. B. Papp, and H. J. Kimble, *Cavity Optomechanics with Stoichiometric SiN Films,* Phys. Rev. Lett. **103**, 207204 (2009).

[84] S. Chakram, Y. S. Patil, L. Chang, and M. Vengalattore, *Dissipation in ultrahigh quality factor sin membrane resonators,* Phys. Rev. Lett. **112**, 127201 (2014).

[85] A. H. Safavi-Naeini, J. Chan, J. T. Hill, S. Gröblacher, H. Miao, Y. Chen, M. Aspelmeyer, and O. Painter, *Laser noise in cavity-optomechanical cooling and thermometry,* New J. Phys. **15**, 035007 (2013).

[86] G. M. Harry, A. M. Gretarsson, P. R. Saulson, S. E. Kittelberger, S. D. Penn, W. J. Startin, S. Rowan, M. M. Fejer, D. R. M. Crooks, G. Cagnoli, J. Hough, and N. Nakagawa, *Thermal noise in interferometric gravitational wave detectors due to dielectric optical coatings,* Class. Quantum Grav. **19**, 897 (2002).

[87] S. Gröblacher, J. B. Hertzberg, M. R. Vanner, S. Gigan, K. C. Schwab, and M. Aspelmeyer, *Demonstration of an ultracold micro-optomechanical oscillator in a cryogenic cavity,* Nature Phys. **5**, 485 (2009).

[88] D. Kleckner, B. Pepper, E. Jeffrey, P. Sonin, S. M. Thon, and D. Bouwmeester, *Optomechanical trampoline resonators,* Opt. Express **19**, 19708 (2011).

[89] D. E. Chang, C. A. Regal, S. B. Papp, D. J. Wilson, J. Ye, O. Painter, H. J. Kimble, and P. Zoller, *Cavity opto-mechanics using an optically levitated nanosphere,* Proc. Natl. Acad. Sci. **107**, 1005 (2010).

[90] J. Gieseler, L. Novotny, and R. Quidant, *Thermal nonlinearities in a nanomechanical oscillator,* Nature Phys. **9**, 806 (2013).

[91] R. Zhang, C. Ti, M. I. Davanço, Y. Ren, V. Aksyuk, Y. Liu, and K. Srinivasan, *Integrated tuning fork nanocavity optomechanical transducers with high $f_M q_M$ product and stress-engineered frequency tuning,* Appl. Phys. Lett. **107**, 131110 (2015).

[92] A. Nunnenkamp, K. Børkje, J. Harris, and S. Girvin, *Cooling and squeezing via quadratic optomechanical coupling,* Phys. Rev. A **82**, 021806 (2010).

[93] Z. Deng, Y. Li, M. Gao, and C. Wu, *Performance of a cooling method by quadratic coupling at high temperatures,* Phys. Rev. A **85**, 025804 (2012).

[94] K. Usami, A. Naesby, T. Bagci, B. M. Nielsen, J. Liu, S. Stobbe, P. Lodahl, and E. S. Polzik, *Optical cavity cooling of mechanical modes of a semiconductor nanomembrane,* Nature Phys. **8**, 168 (2012).

[95] S. Gigan, H. R. Böhm, M. Paternostro, F. Blaser, G. Langer, J. B. Hertzberg, K. C. Schwab, D. Bäuerle, M. Aspelmeyer, and A. Zeilinger, *Self-cooling of a micromirror by radiation pressure,* Nature **444**, 67 (2006).

[96] O. Arcizet, P.-F. Cohadon, T. Briant, M. Pinard, and A. Heidmann, *Radiation-pressure cooling and optomechanical instability of a micromirror,* Nature **444**, 71 (2006).

[97] A. Schliesser, P. Del'Haye, N. Nooshi, K. J. Vahala, and T. J. Kippenberg, *Radiation Pressure Cooling of a Micromechanical Oscillator Using Dynamical Backaction,* Phys. Rev. Lett. **97**, 243905 (2006).

[98] C. H. Bui, J. Zheng, S. W. Hoch, L. Y. T. Lee, J. G. E. Harris, and C. W. Wong, *High-reflectivity, high-q micromechanical membranes via guided resonances for enhanced optomechanical coupling,* Appl. Phys. Lett. **100**, 021110 (2012).

[99] K. Makles, T. Antoni, A. G. Kuhn, S. Deléglise, T. Briant, P.-F. Cohadon, R. Braive, G. Beaudoin, L. Pinard, C. Michel, V. Dolique, R. Flaminio, G. Cagnoli, I. Robert-Philip, and A. Heidmann, *2d photonic-crystal optomechanical nanoresonator,* Optics Lett. **40**, 174 (2015).

[100] S. S. Verbridge, R. Ilic, H. Craighead, and J. M. Parpia, *Size and frequency dependent gas damping of nanomechanical resonators,* Appl. Phys. Lett. **93**, 013101 (2008).

[101] S. Schmid, K. D. Jensen, K. H. Nielsen, and A. Boisen, *Damping mechanisms in high-q micro and nanomechanical string resonators,* Phys. Rev. B **84**, 165307 (2011).

[102] P.-L. Yu, T. P. Purdy, and C. A. Regal, *Control of material damping in high-q membrane microresonators,* Phys. Rev. Lett. **108**, 083603 (2012).

[103] L. G. Villanueva and S. Schmid, *Evidence of surface loss as ubiquitous limiting damping mechanism in sin micro- and nanomechanical resonators,* Phys. Rev. Lett. **113**, 227201 (2014).

[104] A. Darvishian, B. Shiari, G. He, and K. Najafi, *Effect of substrate thickness on quality factor of mechanical resonators,* in *Inertial Sensors and Systems (ISISS), 2015 IEEE International Symposium on* (IEEE, 2015) pp. 1–4.

[105] A. Kaushik, H. Kahn, and A. H. Heuer, *Wafer-level mechanical characterization of silicon nitride mems,* J. Microelectromech. Syst. **14**, 359 (2005).

[106] R. A. Norte, (2014), patent pending.

[107] R. A. Norte, *Nanofabrication for On-Chip Optical Levitation, Atom-Trapping, and Superconducting Quantum Circuits*, Ph.D. thesis, California Institute of Technology (2014).

[108] M. Bhattacharya and P. Meystre, *Trapping and cooling a mirror to its quantum mechanical ground state,* Phys. Rev. Lett. **99**, 073601 (2007).

[109] K.-K. Ni, R. Norte, D. Wilson, J. Hood, D. Chang, O. Painter, and H. Kimble, *Enhancement of mechanical q factors by optical trapping,* Phys. Rev. Lett. **108**, 214302 (2012).

[110] M. Yuan, M. A. Cohen, and G. A. Steele, *Silicon nitride membrane resonators at millikelvin temperatures with quality factors exceeding* 10^8, Appl. Phys. Lett. **107**, 263501 (2015).

[111] *Thermal performance of a radiatively cooled system for quantum optomechanical experiments in space,* Applied Thermal Engineering **107**, 689 (2016).

[112] C. Reinhardt, T. Müller, A. Bourassa, and J. C. Sankey, *Ultralow-noise sin trampoline mems for sensing and optomechanics,* Phys. Rev. X **6**, 021001 (2016).

[113] H. J. Kimble, *The quantum internet,* Nature **453**, 1023 (2008).

[114] J. P. Moura, R. A. Norte, J. Guo, C. Schäfermeier, and S. Gröblacher, *Centimeter-scale suspended photonic crystal mirrors,* Opt. Express **26**, 1895 (2018).

[115] F. Lu, F. G. Sedgwick, V. Karagodsky, C. Chase, and C. J. Chang-Hasnain, *Planar high-numerical-aperture low-loss focusing reflectors and lenses using subwavelength high contrast gratings,* Opt. Express **18**, 12606 (2010).

[116] D. Fattal, J. Li, Z. Peng, M. Fiorentino, and R. G. Beausoleil, *Flat dielectric grating reflectors with focusing abilities,* Nat. Photon. **4**, 466 (2010).

[117] J. Guo, R. A. Norte, and S. Gröblacher, *Integrated optical force sensors using focusing photonic crystal arrays,* Opt. Express **25**, 9196 (2017).

[118] S. Bernard, C. Reinhardt, V. Dumont, Y.-A. Peter, and J. C. Sankey, *Precision resonance tuning and design of sin photonic crystal reflectors,* Opt. Lett. **41**, 5624 (2016).

[119] U. Kemiktarak, M. Metcalfe, M. Durand, and J. Lawall, *Mechanically compliant grating reflectors for optomechanics,* Appl. Phys. Lett. **100**, 061124 (2012).

[120] S. L. Campbell, R. B. Hutson, G. E. Marti, A. Goban, N. Darkwah Oppong, R. L. McNally, L. Sonderhouse, J. M. Robinson, W. Zhang, B. J. Bloom, and J. Ye, *A fermi-degenerate three-dimensional optical lattice clock*, Science **358**, 90 (2017).

[121] T. Kessler, C. Hagemann, C. Grebing, T. Legero, U. Sterr, F. Riehle, M. J. Martin, L. Chen, and J. Ye, *A sub-40-mHz-linewidth laser based on a silicon single-crystal optical cavity*, Nat. Photon. **6**, 687 (2012).

[122] S. Reid and I. W. Martin, *Development of mirror coatings for gravitational wave detectors*, Coatings **6**, 61 (2016).

[123] P.-Y. Madec, *Overview of deformable mirror technologies for adaptive optics and astronomy*, in *Adaptive Optics Systems III*, Vol. 8447 (SPIE, 2012) pp. 844705–1–18.

[124] J. H. Schmid, W. Sinclair, J. García, S. Janz, J. Lapointe, D. Poitras, Y. Li, T. Mischki, G. Lopinski, P. Cheben, A. Delâge, A. Densmore, P. Waldron, and D.-X. Xu, *Silicon-on-insulator guided mode resonant grating for evanescent field molecular sensing*, Opt. Express **17**, 18371 (2009).

[125] X. Fan, ed., *Advanced Photonic Structures for Biological and Chemical Detection*, 1st ed. (Springer-Verlag, 2009).

[126] R. Norte and S. Gröblacher, *Method for fabrication of large-aspect-ratio nano-thickness mirrors*, (2017), NL 2019631.

[127] X. Ji, F. A. S. Barbosa, S. P. Roberts, A. Dutt, J. Cardenas, Y. Okawachi, A. Bryant, A. L. Gaeta, and M. Lipson, *Ultra-low-loss on-chip resonators with sub-milliwatt parametric oscillation threshold*, Optica **4**, 619 (2017).

[128] M. G. Moharam and T. K. Gaylord, *Rigorous coupled-wave analysis of planar-grating diffraction*, J. Opt. Soc. Am. **71**, 811 (1981).

[129] C. Lu and R. H. Lipson, *Interference lithography: a powerful tool for fabricating periodic structures*, Laser Photon. Rev. **4**, 568 (2010).

[130] Breakthrough Initiative, *Starshot*, `https://breakthroughinitiatives.org/Initiative/3`, accessed in July 2017.

[131] H. M. Wiseman, *Quantum theory of continuous feedback*, Phys. Rev. A **49**, 2133 (1994).

[132] D. R. Rhodes, *On a fundamental principle in the theory of planar antennas*, Proc. IEEE **52**, 1013 (1964).

[133] M. Bao, H. Yang, H. Yin, and Y. Sun, *Energy transfer model for squeeze-film air damping in low vacuum*, J. Micromech. Microeng. **12**, 341 (2002).

[134] C. Gärtner, J. P. Moura, W. Haaxman, R. A. Norte, and S. Gröblacher, *Integrated optomechanical arrays of two high reflectivity sin membranes*, Nano Letters **18**, 7171 (2018).

[135] S. Hong, R. Riedinger, I. Marinković, A. Wallucks, S. G. Hofer, R. A. Norte, M. Aspelmeyer, and S. Gröblacher, *Hanbury Brown and Twiss interferometry of single phonons from an optomechanical resonator*, Science **358**, 203 (2017).

[136] R. Riedinger, A. Wallucks, I. Marinković, C. Löschnauer, M. Aspelmeyer, S. Hong, and S. Gröblacher, *Remote quantum entanglement between two micromechanical oscillators*, Nature **556**, 473 (2018).

[137] M. Bhattacharya and P. Meystre, *Multiple membrane cavity optomechanics*, Phys. Rev. A **78**, 041801 (2008).

[138] M. Gross, C. Fabre, P. Pillet, and S. Haroche, *Observation of near-infrared dicke superradiance on cascading transitions in atomic sodium*, Phys. Rev. Lett. **36**, 1035 (1976).

[139] T. Kipf and G. S. Agarwal, *Superradiance and collective gain in multimode optomechanics*, Phys. Rev. A **90**, 053808 (2014).

[140] M. Zhang, G. S. Wiederhecker, S. Manipatruni, A. Barnard, P. McEuen, and M. Lipson, *Synchronization of micromechanical oscillators using light,* Phys. Rev. Lett. **109**, 233906 (2012).

[141] H. Xu, D. Mason, L. Jiang, and J. G. E. Harris, *Topological energy transfer in an optomechanical system with exceptional points,* Nature **537**, 80 (2016).

[142] M. Schmidt, M. Ludwig, and F. Marquardt, *Optomechanical circuits for nanomechanical continuous variable quantum state processing,* New J. Phys. **14**, 125005 (2012).

[143] M. J. Hartmann and M. B. Plenio, *Steady state entanglement in the mechanical vibrations of two dielectric membranes,* Phys. Rev. Lett. **101**, 200503 (2008).

[144] B. Nair, A. Naesby, and A. Dantan, *Optomechanical characterization of silicon nitride membrane arrays,* Opt. Lett. **42**, 1341 (2017).

[145] M. J. Weaver, F. Buters, F. Luna, H. Eerkens, K. Heeck, S. de Man, and D. Bouwmeester, *Coherent optomechanical state transfer between disparate mechanical resonators,* Nat. Commun. **8**, 824 (2017).

[146] V. Liu and S. Fan, *S^4 : A free electromagnetic solver for layered periodic structures,* Comput. Phys. Commun. **183**, 2233 (2012).

[147] J. C. Sankey, C. Yang, B. M. Zwickl, A. M. Jayich, and J. G. E. Harris, *Strong and tunable nonlinear optomechanical coupling in a low-loss system,* Nature Phys. **6**, 707 EP (2010).

[148] A. Xuereb and P. Domokos, *Dynamical scattering models in optomechanics: going beyond the 'coupled cavities' model,* New J. Phys. **14**, 095027 (2012).

[149] Y. Tsaturyan, A. Barg, E. S. Polzik, and A. Schliesser, *Ultracoherent nanomechanical resonators via soft clamping and dissipation dilution,* Nature Nanotechnology **12**, 776 EP (2017).

[150] A. H. Ghadimi, S. A. Fedorov, N. J. Engelsen, M. J. Bereyhi, R. Schilling, D. J. Wilson, and T. J. Kippenberg, *Elastic strain engineering for ultralow mechanical dissipation,* Science **360**, 764 (2018).

[151] P.-L. Yu, K. Cicak, N. S. Kampel, Y. Tsaturyan, T. P. Purdy, R. W. Simmonds, and C. A. Regal, *A phononic bandgap shield for high-q membrane microresonators,* Applied Physics Letters **104**, 023510 (2014).

[152] R. Fischer, D. P. McNally, C. Reetz, G. G. Assumpcao, T. R. Knief, Y. Lin, and C. A. Regal, *Spin detection with a micromechanical trampoline: Towards magnetic resonance microscopy harnessing cavity optomechanics,* arXiv:1811.05718 (2018).

[153] G. Cantatore (CAST Collaboration), *Latest Results with the KWISP force Sensor at CAST,* in *12th Patras Workshop on Axions, WIMPs and WISPs*, DESY-PROC, Jeju Island (South Korea), 20–24 Jun 2016 (Verlag Deutsches Elektronen-Synchrotron, Hamburg, 2017) pp. 18–22.

[154] Y. Horie, S. Han, J.-Y. Lee, J. Kim, Y. Kim, A. Arbabi, C. Shin, L. Shi, E. Arbabi, S. M. Kamali, H.-S. Lee, S. Hwang, and A. Faraon, *Visible wavelength color filters using dielectric subwavelength gratings for backside-illuminated cmos image sensor technologies,* Nano Letters **17**, 3159 (2017).

[155] Metamaterial Technologies Inc., *metaAir Laser Glare Protection,* `http://www.metamaterial.com/lamda-guard/metaair/`, accessed in January 2019.

[156] A. R. Atwater, Harry A.and Davoyan, O. Ilic, D. Jariwala, M. C. Sherrott, C. M. Went, W. S. Whitney, and J. Wong, *Materials challenges for the starshot lightsail,* Nature Materials (2018), 10.1038/s41563-018-0075-8.

[157] X. Wei, J. Sheng, C. Yang, Y. Wu, and H. Wu, *A controllable two-membrane-in-the-middle cavity optomechanical system,* arXiv:1812.08926 (2018).

[158] D. E. Chang, K.-K. Ni, O. Painter, and H. J. Kimble, *Ultrahigh-qmechanical oscillators through optical trapping,* New Journal of Physics **14**, 045002 (2012).

[159] M. Borselli, K. Srinivasan, P. E. Barclay, and O. Painter, *Rayleigh scattering, mode coupling, and optical loss in silicon microdisks,* Applied Physics Letters **85**, 3693 (2004).

LIST OF PUBLICATIONS

5. C. Gärtner[*], **J.P. Moura**[*], W. Haaxman, R.A. Norte, and S. Gröblacher, *Integrated optomechanical arrays of two high reflectivity SiN membranes*, Nano Letters **18** (11), 7171–7175 (2018)
4. **J.P. Moura**[*], R.A. Norte[*], J. Guo, C. Schäfermeier and S. Gröblacher, *Centimeter-scale suspended photonic crystal mirrors*, Optics Express **26** (2), 1895–1909 (2018)
3. R.A. Norte, **J.P. Moura** and S. Gröblacher, *Mechanical resonators for quantum optomechanics experiments at room temperature*, Physical Review Letters **116** (14), 147202 (2016)
2. **J.P. Moura**, H. Baierl, J.L. Auguste, R. Jamier, P. Roy, J.L. Santos, O. Frazão, *Evaporation of volatile compounds in suspended-core fibers*, Optics Letters **39** (13), 3868–3871 (2014)
1. **J.P. Moura**, S.O. Silva, M. Becker, M. Rothhardt, H. Bartelt, J.L. Santos, O. Frazão, *Optical inclinometer based on a phase-shifted bragg grating in a taper configuration*, IEEE Photonics Technology Letters **26** (4), 405–407 (2014)

[*] These authors contributed equally to this work.

CURRICULUM VITÆ

João Pedro PINTO MOURA

26-03-1991 Born in Porto, Portugal.

EDUCATION

2007–2009 High School
Padrão da Légua High School, Matosinhos, Portugal

2009–2012 BSc in Technological Physics
University of Porto, Portugal

2012–2014 MSc in Physical Engineering
University of Porto, Portugal
Thesis: Microstructured optical fibers for fluid sensing applications
Promotor: Prof. dr. ir. O. S. R. Frazão

2015–2019 PhD in Experimental Physics
Delft University of Technology, the Netherlands
Thesis: Making light jump: Photonic crystals on trampoline membranes for optomechanics experiments
Promotor: Prof. dr. ir. H. S. J. van der Zant
Co-Promotor: Dr. S. Gröblacher

ACKNOWLEDGEMENTS

THE work presented in this thesis is the result of the collective effort of several people. Some contributed directly to the projects. Others indirectly, through their friendship and support. I am grateful to everyone with whom I crossed paths during the past 4 years, but I would like to acknowledge some of them in particular.

Although my interactions with *Herre van der Zant* were short and few, I am thankful for his insights and positive reinforcement which helped me to lead my project successfully. This is also a good opportunity to thank the remaining members of my doctoral committee who have read this dissertation, provided me with useful feedback, and were available to travel to Delft and be present at my defense ceremony: *Kobus Kuipers, David Vitali, Gary Steele, Silvan Schmid, Wolfgang Löffler,* and *Yaroslav Blanter*.

In December 2014, *Simon Gröblacher* captivated me with an ambitious project and the promise of many challenges to face. I arrived at the group's inception to an empty (non-existing, even) lab as the first PhD student and today I leave a much larger team with a variety of projects and plenty of successful results. During this time both of us grew substantially. Building a new lab from scratch, I learned a large breadth of technical skills and have become a well-rounded engineer, and, most importantly, through Simon I developed my personality considerably, becoming a more confident, pragmatic person. I am truly grateful for the opportunity of working and learning with him and I am certain that his lab will continue to contribute positively to optomechanics research for years to come.

The projects described here were mostly carried out by surprisingly small group of people. These are the ones I worked most closely with and from whom I have learned the most:

I was frequently amazed by *Richard Norte*'s inventiveness and ingenuity. His constant out-of-the-box thinking was always an inspiration and the source of most of the creative leaps in our research. He was also a great counterbalance to my personality, bringing positivism and determination to our work. It was great to see him grow into building his own company and research group and I am certain that his ambition and strategic mindset will provide fruitful results.

Clemens Schäfermeier arrived in our group at a crucial point when I knew enough to precisely define the challenges I was facing, but not enough to solve them in the best way possible. He brought a wealth of knowledge from his previous experiments which helped our lab give a large step forward and I can say for certain that it was with him that I learned the most. Our work methodologies were a complete match and it was a pleasure to work with him every single day. Until today, he is the best professional that I have crossed paths with, which convinces me that his future will certainly be bright.

Our lab had a permanent visitor from the University of Vienna, *Claus Gärtner*. We shared not only the same project goals but also personal interests. Because of this, we spent countless hours working together and supporting each other in the most difficult professional and personal moments. Ultimately, we found that we were more productive as a whole by specializing ourselves into the tasks we loved to do the most and I believe this was one of the keys for the success of our projects.

I started working with *Jingkun Guo* during his MSc thesis. From early on it was clear that he was very knowledgeable, a quick learner and a very efficient researcher. He was almost single-handedly responsible for the large PhC measurements, which was a crucial contribution for that chapter. Although we did not work directly together anymore, it was great to continue sharing the same lab with him, now as a PhD candidate.

At the end of my PhD, *Matthijs de Jong* joined our group to take over the membranes project. In the short time we spent together I was impressed by his ability to assimilate the knowledge the group generated thus far and to make relevant contributions to our research. Because of this, I leave feeling that the lab I helped create will continue in competent hands.

During the past years I was fortunate to develop my teaching and mentoring skills by supervising several students who chose to work in our lab for their graduation projects: *Luka Bavdaz*, who quickly learned how to independently operate the mechanics setup and contributed to very preliminary measurements at the start of our lab; *Michail Vlassov*, who designed filter cavities which are still a crucial component of some our group's setups; *Wouter Haaxman*, who greatly improved the usability of both characterization setups and helped develop the calibration procedure of the optics one; and *Klara Knupfer*, who fully redesigned the cavity setup and placed great effort in better understanding the dynamics of the cavity locking procedure. It was great to observe their development during their projects and to feel that I somehow took part in it. In addition, each of them has made a mark on me and helped me grow in some way or another, and for this I have to thank them.

All remaining members of our lab were involved in considerably different projects. Notwithstanding, they always made the effort of keeping up with the membranes' developments, asked pertinent questions during the group meetings and were often useful resources when we faced scientific or technical issues. *Alexander Krause* was in our group only for a brief time but he was a great help getting me started in the lab. *Igor Marinković* always proved to be knowledgeable in all aspects of our work, but the traits I appreciated the most in him were his insightfulness and ability to explain concepts in elucidating fashions. Prudent, creative, and pragmatic, *Andreas Wallucks* had all the qualities of an excellent researcher, an unmatched enthusiasm for his work, and constant availability to help, making it a pleasure to work with him. It was fascinating to hear about *Maarten Leeuwenhoek*'s progression in building an STM from scratch, a project I followed with great interest which often served as an inspiration for our cavity designs. Since our personal interests were highly compatible, most of my conversations with *Moritz Forsch* were not about science, but I thoroughly enjoyed his strong dedication to his hobbies and his recommendations as an expert foodie. *Robert Stockill* arrived filled with knowledge and energy to push towards a new research direction in the group and I am con-

vinced that with his drive it will be a certain success. I am thankful to all of my lab colleagues for creating the enjoyable environment which we shared for the past four years.

Most of the work presented here relied on helpful technical discussions with people not only from the TU Delft (*Gary Steele, Martijn Cohen, João Machado, Filippo Alpeggiani, Alard Katan*) but also from the University of Vienna (*Ralf Riedinger, Witlef Wieczorek, Jason Hoelscher-Obermaier*) and Leiden University (*Wolfgang Löffler, Vitaly Fedoseev, Fernando Luna*), to all of whom I am very grateful.

Equally fundamental was the support of the Quantum Nanoscience and the Kavli Nanolab staff, in particular from *Etty van der Leij, Maria Roodenburg-van Dijk, Marije Boonstra, Erika van Verseveld, Heleen Woldhuis, Ronald Bode, Tino Kool, Charles de Boer, Marc Zuiddam, Marco van der Krogt, Arnold van Run,* and *Ewan Hendriks.*

Throughout my time at TU Delft I appreciated meeting a whole lot more people than the ones mentioned here. Although their contribution was not on a professional level, I still very much enjoyed getting to know all of them and I thank them for giving me that opportunity.

Finally, a special acknowledgement to those whose personal support was the most significant and to whom I dedicate this thesis. They were a constant source of encouragement and perspective, and without them none of this work would have been possible or meaningful.

To my family, both given and chosen.